TWO-DIMENSIONAL PLASMA SHEATH OBSERVATIONS IN PLASMA SOURCE ION IMPLANTATION

By

Kevin Alan Meyer

Submitted in partial fulfilment

of the requirements for the degree of

Master of Science

Department of Physics, University of Natal

September 1996

Durban

1996

Preface

The experimental work described in this thesis was carried out in the Department of Physics, University of Natal, Durban, from February 1994 to March 1995, under the supervision of Professor Michael J. Alport.

These studies represent original work by the author and have not been submitted in any form to another University. Where use was made of the work of others it has been duly acknowledged in the text.

Acknowledgements

I would like to take this opportunity to thank everyone who offered advice and assistance during the research period, especially Professor M.J. Alport, my supervisor, Mark Harmer, who's work on the simulation code gave me a different perspective, and Jaynie Padayachee, for reading through it all in the end and generally polishing things off.

Special thanks to Willem de Beer and Derrick Davies and the rest of the Physics Mechanical and Electronic Workshop staff. I would also like to take this opportunity to thank all my fellow postgraduate students for many valuable discussions. There are probably many others to whom I am indebted, to them I offer my gratitude.

I am also grateful for funding received from the Foundation for Research Development, and for the years of truly wonderful support from my parents, without whom none of this would have been possible.

And finally, to Linda, for all the love, support and encouragement, without whom, I would probably have finished earlier, but much, much poorer!

Abstract

Plasma Source Ion Implantation (PSII) is the process of implanting high energy ions [10–50 keV] into metallic targets, by pulsing them negatively whilst immersed in a background plasma. PSII achieves surface hardening, and increased wear and corrosion resistance.

Numerous papers have been published describing numerical simulations and models of the PSII process, most of which have been limited to one dimension.

This thesis presents the results of work carried out in the Plasma Processing Laboratory at the University of Natal, Durban, during 1994–1995. In particular, measurements of two-dimensional plasma sheath effects due to spherical and complex shaped targets are compared with a particle-in-cell simulation code.

The simulation results are used to define a relationship between the plasma potential of the sheath edge and the saturation currents. Thus allowing for the saturation currents to be used to trace sheath evolution. These results are compared with the experimental measurements from the spherical target.

Results from the rectangular and complex saw-tooth targets show a lack of sheath

conformality. The ion saturation currents were susceptible to electron swamping, which occured in localised regions associated with target structure. It is thought that secondary electrons ejected from the target are focused and accelerated by the high target potential into these regions, where they swamp the ion current.

Contents

List of Figures

List of Symbols

I_{sat}^{+}	Ion saturation current
I_{sat}^{-}	Electron saturation current
I_D	Discharge current
V_f	Filament potential
m_i	Ion mass (kg)
m_e	Electron mass (kg)
n_i	Ion density (cm^{-3})
n_e	Electron density (cm^{-3})
n_n	Neutral gas density (cm^{-3})
n_0	Plasma density (cm^{-3})
N_∞	Plasma background density (cm^{-3})
τ_{pi}	Ion plasma period (s)
τ_{pe}	Electron plasma period (s)
ω_{pi}	Ion plasma frequency (radians.s^{-1})
ω_{pe}	Electron plasma frequency (radians.s^{-1})
f_{pi}	Ion plasma frequency (Hz)
f_{pe}	Electron plasma frequency (Hz)
λ_m	Mean-free-path for collisions (m)
λ_D	Debye length (m)
ϕ	Potential (V)
ϕ_f	Floating potential (V)

ϕ_p	Plasma Potential (V)
ϕ_{probe}	Probe potential (V)
ϕ_{target}	Target potential (V)
T_e	Electron temperature (eV)
T_i	Ion temperature (eV)
ϵ_0	Permittivity of free space ($C^2.N^{-1}.m^{-2}$)
S_0	Planar ion matrix sheath thickness (cm)
r_0	Spherical ion matrix sheath thickness (cm)
ν_d	Drift velocity ($cm.s^{-1}$)
erf	Error function
c_s	Ion acoustic speed ($cm.s^{-1}$

Two-Dimensional Plasma Sheath Observations in Plasma Source Ion Implantation

Kevin Alan Meyer

September 4, 1996

Chapter 1

Introduction

1.1 Introduction to Surface Modification

There are many methods being used in industry to harden, strengthen and prolong the life expectancy of metallic materials used in a wide variety of applications. Often it is desirable to not harden the entire object, since not only could the hardened product become very brittle, but increasingly because the hardening process requires expensive, rare, or insoluble compounds. Surface hardening is typically performed to improve the characteristics of that portion of the object which most requires it, without adversely affecting its bulk properties.

1.1.1 Thermal Techniques

Since the early iron-age, black-smiths have used methods such as selective heating and quenching to harden cast objects. Modern day processing plants using gas torches and lasers achieve localised hardening using this technique. By heating steels in carbon-rich environments, a technique called carburization, carbon can be introduced into the surface to achieve surface hardening.

Nitrogen, too, can be introduced into steels to achieve surface hardening and corrosion resistance. Processes such as cyaniding, carbonitriding and nitriding all

introduce either nitrogen or both carbon and nitrogen into the target surface by heating the target to be processed in cyanide, carbon-monoxide and ammonia rich, or nitrogen gas environments respectively. More detail on these methods can be found in Askeland [4].

Strafford [5], a good text on surface modification, provides an excellent introduction with detail on current trends in other surface modification techniques, such as surface coatings.

1.1.2 Coating Techniques

Zinc and nickel are common coatings added to steel and iron by such methods as hot-dip galvanizing and electroplating. Zinc-rich alloys are often electrodeposited, with coatings containing nickel or cobalt. Electrodeless deposition based on nickel and phosphorus or boron can provide wear and corrosion resistance with negligible change in size, and is especially useful for small delicate components. The inclusion of PTFE can improve frictional characteristics.

Alternatively, coatings can be deposited by vapour deposition methods, such as chemical vapour deposition (CVD), or physical vapour deposition (PVD). CVD is a process in which a stream of gas containing volatile components of the elements to be deposited is introduced in a reaction chamber. By controlling the conditions within the chamber, the appropriate chemical reaction deposits a coating on the surface of the substrate. Metal-organic CVD methods use organo-metallic compound vapours which are stable at room temperature, but which decompose at higher temperatures. The electronics industry uses these methods to produce Al and GaAs films. Plasma aided CVD is a form of low pressure CVD in which the energy of the reactants is increased by producing a plasma, which can achieve the required coating properties at a lower substrate temperature.

PVD is carried out under a partial vacuum, and at least one of the deposited species is atomized from a solid within the processing chamber. Electron Beam PVD

uses an electron beam to heat the solid to be vapourised. By mounting the solid on a cooled base, there is no practical upper limit to which the solid surface can be heated, and so this process can be used to evaporate ceramics for deposition. Titanium Nitride (TiN) deposited onto tool steel can improve the hardness from about 850 VPN to greater than 2500 VPN.

The disadvantage with coating technology is that the surface dimensions of the target are increased by the thickness of the coating, along with the associated risks of bonding failure.

1.1.3 Ion Implantation Techniques

Ion implantation is the process whereby ions, either atomic or molecular [6], are implanted into the surface of the target material. These ions are typically implanted after thermal ionization in an oven. A potential difference between a grid and the oven extracts and accelerates these ions into an ion beam. Additional grids and energy selectors create a high energy ion beam with a relatively narrow energy spread. The resultant high energy beam can be used to implant ions into a variety of materials. The alloys thus formed are barely 1000Å thick but are able to significantly alter the surface characteristics without adversely affecting the bulk properties of the material. The characteristics of the alloy formed are determined by the depth and density of the implanted ions. Since the depth is determined by the implantation energy and the density by implantation time, materials with precisely specified compositions can be manufactured. As described in a review article [7], while originally used in the semiconductor industry to dope silicon substrates, the implantation of metals with different components improves a number of metallurgical properties:

1. The implantation of copper in beryllium raises the temperature at which it superconducts.
2. The implantation of hydrogen into the walls improves ion plasma-wall recycling properties in fusion tokamaks.

3. The implantation of palladium into titanium reduces weight loss due to boiling in sulphuric acid by 3 orders of magnitude [8],
4. Improving surface hardness by the implantation of nitrogen into steel, a process pioneered by the Atomic Energy Research Establishment Harwell Laboratories, England [9,10],
5. The implantation of carbon in steel reduces the coefficient of friction by half [11], and
6. The implantation of nitrogen in Ti-6Al-4V reduces losses due to wear [12], which has specific applications in the processing of artificial hip joints [13] where wear-produced debris can cause inflammation. The inherent inaccessibility of the implanted component makes an extended lifespan more desirable.

Since ion implantation is a surface modification process and not a coating technique, it offers a number of unique advantages:

1. There is no bonding failure or surface delamination.
2. There are no dimensional changes, so cutting edges retain their sharpness and precision engineered items can be processed post production.
3. Surface properties can be changed without affecting bulk properties.
4. Since it uses active athermal non-diffusive implantation, it is not limited by thermodynamic constraints. Since it is a non-equilibrium process, new alloys are not limited by classical thermodynamic properties and diffusion kinetics, allowing for the mixing of otherwise insoluble materials, for example implanting tantalum into iron to improve corrosion resistance [14].
5. The distance through which implanted atoms diffuse is very small. Since the characteristic time for a diffusion-controlled process varies as the square of the distance, reactions occur faster and at lower temperatures than conventional metallurgical work.
6. The ions are introduced in an atomically dispersed fashion forming intimate mixtures. There are no oxide or other interfacial barriers, as occur between

thin films, which can block reactions.

In summary, ion implantation is a low temperature surface modification technique that produces minimal dimensional changes due to thermal distortion and degradation of the surface finish.

1.2 Implantation Methods

1.2.1 Ion beam

Ions were originally implanted into materials using ion beams. In ion beam implantation, typical implantation energies of 10keV to 500keV are produced. Since this is a line-of-sight method precautions are needed to prevent excessive surface degradation due to sputtering (see section 3.1.1). Furthermore the desire to implant all surfaces requires expensive and complex target manipulation hardware and masks.

In conventional ion beam implantation, ions are extracted from the ion source, accelerated to the desired energy, and raster-scanned across the target. The line-of-sight nature of this technique requires target manipulation to bring all treated surfaces into the beam. The addition of target manipulation and beam-rastering hardware adds complexity and expense to the process, limiting the size of the target that can be processed. Temperature build-up in the processed region further complicates the process if distortion due to local thermal expansion and overheating is to be avoided. The additional problems of retained dose (section 3.1.1), and surface degradation due to sputtering [15] (figure 2) when the ions strike the target surface at oblique angles requires the construction of target-specific tailored masks (figure 3). However, the sputtering of this mask can contaminate the target.

A variation of the ion beam technique is IBAD, or ion beam assisted deposition, where the target is first coated with a thin film, which is then implanted. The implanting ions assist in improving the coating target bond.

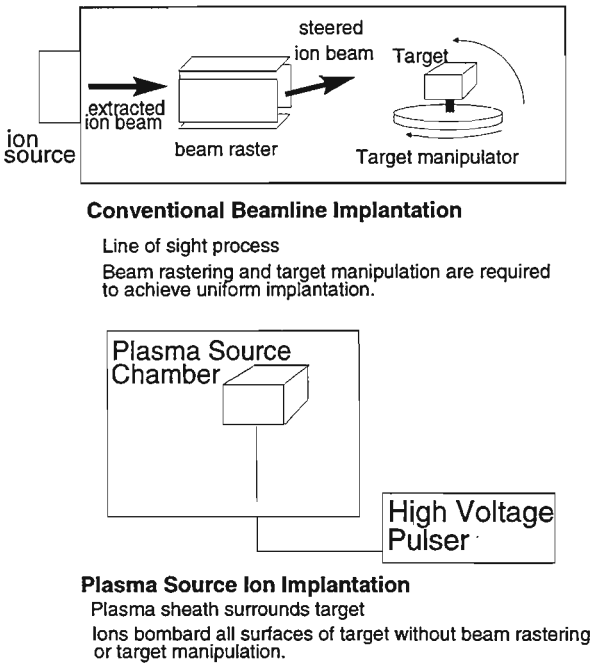

Figure 1: A comparison of the hardware requirements of conventional beamline ion implantation vs PSII [1].

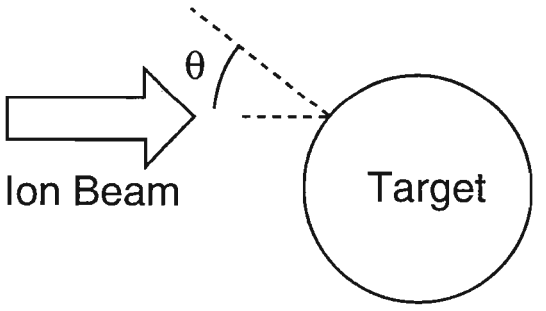

Figure 2: The maximum retained dose (D) for ion implantation depends on the angle of incidence of the ion, $D \sim \cos^{\frac{8}{3}} \theta$ [1].

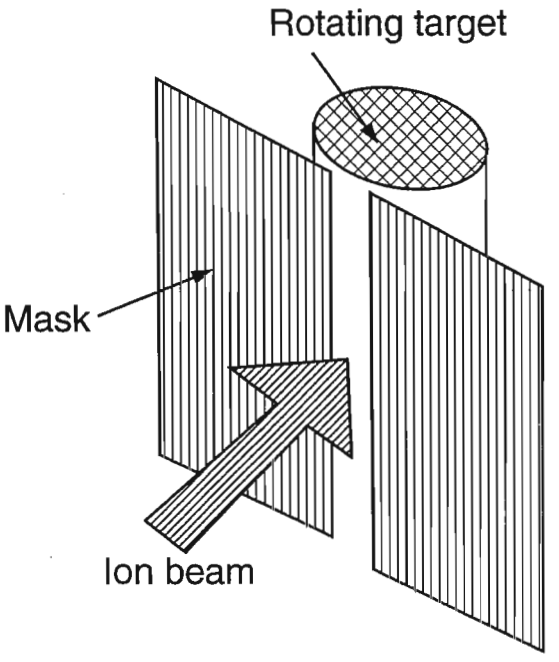

Figure 3: Ion beam implantation technique: Conventional line-of-sight beamline ion implantation requires masking of convex targets to minimize sputtering [1].

1.2.2 Plasma Source Ion Implantation

Plasma Source Ion Implantation (PSII) is a new cost-effective ion-implantation technique developed and patented by J.R. Conrad *et al* [16]. It is cost effective, since by its very nature no beam rastering or target masking hardware is required. Since PSII is plasma based, special emphasis is placed on plasma-based ion sources. For metallurgical reasons, nitrogen is the most common ion source. Numerous authors have reported on the beneficial applications of nitrogen ion beam implantation, to achieve improved wear and lifetime properties of metals;

1. Fayeulle *et al* [17] reported 3-fold decrease in the wear rate of 40keV N^+ implanted in tungsten carbide
2. Yost *et al* [18] implanted 304-stainless steel with 50keV N^+ ions and reduced maximum wear depth for light loads (850-MPa Hertzian stress) by more than an order of magnitude
3. Kustas *et al* [19] implanted 440-C stainless steel with 40keV N^+ ions and increased its rolling contact fatigue lifetime by over 40%
4. Hirano and Miyake [20] implanted 440-C bearings with 90keV N^+ and N^{++} ions to achieve a 100-fold lifetime extension.
5. In the cutting tool and die industry, Hartley [21] reported a fivefold increase in the life-span of M-2 steel taps used in phenolic resin. Tool steel fuel injectors have shown a 100-fold improvement in experiments by Hirvonen [22]. Hartley [21] has reported a two- to four-fold increase in the service lifetime of diamond tools for plastic cutting, while Dutchman and Partyka have shown that plastic extrusion die lifetime can be improved by a factor of 4 [23].
6. Zhang *et al* [24] present results of improved corrosion resistance of nitrogen implanted 6061T aluminium alloy.
7. Min *et al* [25] discuss PIII and oxygen implantation to form thin buried oxide layers in the sub-milliTorr operating pressure regime. A 20–50 nm thick buried oxide layer with a Si overlayer thickness of 20–50 nm was fabricated in about 5

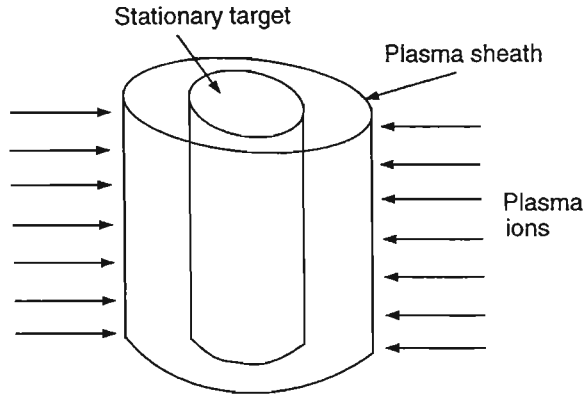

Figure 4: PSII implantation technique: Ions are accelerated from the sheath edge, to strike the entire target surface with nearly normal incidence thus reducing the sputtering and retained dose problem.

minutes.

8. Walter *et al* [26] present the results of improved corrosion resistance of nitrogen implanted 99.999% pure aluminium. They obtain a zero corrosion current for non-sputter cleaned aluminium in salt water.
9. Brown *et al* [27] present a method of fabricating non-equilibrium alloy layers of arbitrarily high dopant concentration and thickness. By repetitively pulse biasing the substrate to high negative voltage while immersed in the metal plasma from a vacuum arc plasma gun, a layer can be synthesized that is atomically mixed into the substrate with an interface width determined by the early-time bias voltage and a thickness determined by the overall duration of the process.

1.3 PSII Concept

Plasma Source Ion Implantation, or PSII, also referred to as Plasma Immersion Ion Implantation (PIII or PI^3), is the process whereby the target to be processed is immersed in a plasma consisting of the ions to be implanted. By pulse-biasing the target to high negative voltages (10–150 kV [28,29]), the plasma ions in the vicinity

of the target are accelerated into the target. Since the ions are accelerated across the sheath (see section 2.3) which forms around the target, the entire target surface is processed simultaneously. Also, since the ions are accelerated along the electric field lines, they tend to strike the target surface with approximately normal incidence, thus minimizing the problem of retained dose and eliminating the requirement of a mask. Preliminary investigations into dose uniformity on multiple targets in a test of batch mode processing yielded promising results [30]. Very much a young science, PSII has been the focus of two international workshops since 1993 [1].

To summarize the advantages of PSII over traditional ion-beam techniques:

1. Elimination of beam rastering and target manipulation hardware,
2. Elimination of target masking and reduction of surface sputtering and retained dose problems,
3. The ion source hardware and controls are at near-ground potential,
4. Greater production throughput, especially for large and/or diverse targets,
5. The smaller, less expensive, easier to operate PSII hardware allow for "in-house" operation, versus the "outside service facility" operation mode prevalent in the ion-beam industry.

1.3.1 Sheath dynamics and PSII pulse theory

The pulsed nature of the PSII target bias gives this technique an important attribute-namely the ability to control the average energy deposited and hence the temperature of the target. The short pulse width (10–500μs) is typically much shorter than the pulse period (0.002 – 1 s). A second requirement of the pulse width is that it should be short enough to prevent the plasma sheath from expanding to the chamber walls or neighbouring target sheaths as this would tend to reduce surface and depth

[1]The first workshop was held in August 1993 at the University of Wisconsin-Madison, USA, the second in February 1995, at the Australian Nuclear Science and Technology Organisation, Sydney, Australia. The third workshop will be held in September 1996 at the Research Centre, Rossendorf, Germany.

implantation uniformity.

1.4 Scope of Thesis

This thesis describes aspects of sheath evolution around one and two dimensional targets in PSII. In particular, ion and electron fluxes are measured by monitoring ion and electron saturation currents collected by a movable Langmuir probe. The position of the plasma sheath can be inferred from these measurements. Results will be presented describing sheath evolution around rectangular, spherical and complex saw-tooth shaped targets. Attention is given to secondary electron emission since this can have a dominating influence on the ion saturation current.

The measurements of complex two-dimensional targets are of importance, for example, in the automotive industry for the processing of gear teeth.

In this thesis the sheath edge is defined as occurring when the local plasma potential achieves some fraction of the target potential (see section 5.2.2). Since the electron saturation current is also reduced at this position, the sheath edge can be associated with this electron saturation current depletion. Though it is more acceptable to define the sheath edge as occurring where $\phi_p \sim kT_e$, the potential is a difficult parameter to measure experimentally, using for example, an emissive probe [31] or a capacitive probe [32].

The measurement of sheaths around rectangular targets is important for the processing of pierce punches and other cutting dies. Here the implantation profiles along target edges is of special interest, since this is where most of the wear takes place. Any effect of target geometry on dose uniformity near the corners must also be identified.

The spherical target is used to produce measurements that can be compared with a numeric plasma simulation. The simulation is used to extract information that can not be easily or accurately measured, and to validate the use of electron saturation

currents to characterize sheath evolution. The spherical, rather than the planar, target measurements are compared with the 1-D Spherical Birdsall particle-in-cell plasma simulation code, since truly planar sheaths are difficult to maintain experimentally.

A significant result obtained with the complex saw-toothed target was the degree of ion focusing and electron channelling that was observed. The outbound electrons are confined to channels created by the target geometry. Such a target would thus result in the generation of localised high intensity X-rays produced when the channelled electrons strike the chamber walls. This phenomenon must be taken into account in the design of chamber shielding and so has potential implications for personnel working near an industrial PSII facility.

Apart from using ion saturation current measurements to describe sheath formation and evolution, the relatively small current measured makes the ion currents extremely sensitive to electron swamping. This is especially noticeable when secondary electrons are emitted from the complex target with a potential energy equal to the target potential. These electrons are focused into channels where they gain enough kinetic energy to overcome the negative probe bias (but positive with respect to the target) of the probe reproducing net negative collected currents. Thus the current collected by a negatively biased probe can be used to highlight areas of increased electron energy.

To summarize, this thesis presents the results of two-dimensional sheath formation and evolution in the PSII process. In particular, sheath evolution around a rectangular corner, a spherical target, and a complex shaped target is measured. Certain other phenomena, such as ion focusing, electron channelling and secondary electron emission are described. The use of ion saturation current measurements as a diagnostic tool is explored, and the validity of using saturation currents to identify the PSII sheath is tested.

Chapter 2

Theory

2.1 Plasma Formation - DC discharge

The plasma described in these experiments was produced by electron bombardment of the neutral gas at low pressures. Primary electrons emitted from the heated filaments and accelerated by an externally provided DC potential collide with neutral argon gas atoms with enough energy to remove at least the first valence electron. These valence electrons are scattered with less energy than the incident primary electron, and are called secondary electrons, and hereafter referred to as secondary plasma electrons. Most electrons in the plasma are secondary electrons. The ionization cross-section is a function of primary electron energy, and peaks at about 100eV for argon, as can be seen in figure 5.

2.1.1 Ionization cross-section and mean-free-path

The mean-free-path λ_m, or mean distance between collisions, is defined by Chen [33] in terms of momentum transfer between collisions of electrons and neutral atoms. The probability of momentum loss can be expressed in terms of the equivalent cross-section σ that the atoms would have if they were perfect absorbers of electron momentum. An ionisation event occurs when the momentum transferred from the incident primary

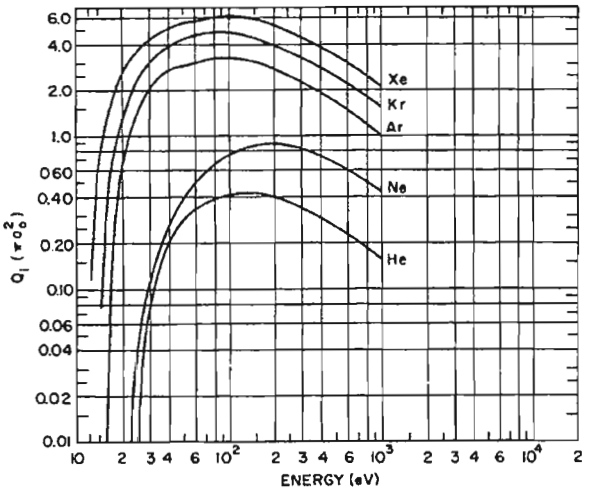

Fig. 5.22 Ionization cross sections for Xe, Kr, A, Ne, and He by electron impact.
D. Rapp, P. Englander-Golden (1965)
JCHEPH J12 V43 P1464

Figure 5: Graph showing ionization cross section as a function of electron energy for various ions. Reproduced from Brown [2].

electron gives the neutral gas atom enough energy to be excited into at least its first charge state, releasing a secondary plasma electron.

Considering electrons incident upon a slab of area A and thickness dx containing n_n neutral atoms per unit volume, where each atom is an opaque sphere of cross-sectional area σ, the number of atoms in the slab is

$$n_n A\ dx.$$

The fraction of the slab blocked by atoms is

$$n_n A\sigma\ dx/A = n_n\sigma\ dx.$$

If a flux Γ of electrons is incident on the slab, the flux emerging on the other side is

$$\Gamma' = \Gamma(1 - n_n\sigma\ dx).$$

Thus the change of Γ with distance is

$$d\Gamma/dx = -n_n\sigma\Gamma$$

or

$$\Gamma = \Gamma_0 e^{-n_n\sigma x} \equiv \Gamma_0 e^{-\frac{x}{\lambda_m}}.$$

In a distance λ_m the flux would be decreased to $\frac{1}{e}$ of its initial value. The quantity λ_m is the mean-free-path for collisions:

$$\lambda_m = \frac{1}{n_n\sigma} \tag{1}$$

2.1.2 Primary electron current

In general the primary electron current, and hence primary electron flux, may be either space charge or cathode temperature limited.

Space charge limited emission

Initially, only a small current can flow between the cathode and anode in the low pressure neutral-atom gas. This is due to the space charge formed by the electrons which accumulate near the cathode and repel newly emitted electrons. The space charge limited current density is given by the Child-Langmuir law [34]:

$$J = \frac{4}{9}\epsilon_0 \left(\frac{2e}{m_e}\right)^{\frac{1}{2}} \frac{U^{\frac{3}{2}}}{d^2} = 2.333 \times 10^{-6} \frac{V_d^{\frac{3}{2}}}{d^2} A.\text{cm}^{-2} \tag{2}$$

where V_d is the discharge bias in Volts, d the distance between the anode and cathode in cm, and J is expressed in units of A.cm^{-2}, which for these experiments, where $V_d = 60$V, $d \simeq 5$ - 30cm, is about 40μA.cm^{-2}.

Temperature limited emission

In plasma discharge devices, the total emission current is usually limited by the filament temperature. The temperature limited emission current is given by the

Richardson law:

$$J = BT^2 e^{-\frac{W}{kT}} A.\text{cm}^{-2} \tag{3}$$

where $B = 4\pi mek^2/h^3 = 120\text{Amp}\cdot\text{cm}^{-2}\cdot\ \text{K}^{-2}$, W is the work function and T the temperature of the filament metal, which for these experiments, where $T \approx 2000\text{K}$, is about 2mA.cm^{-2}. The CRC handbook [35] quotes a value of 1mA.cm^{-2}.

Temperature versus Space charge limitations

Usually, a discharge plasma is generated in the temperature limited regimes so that the discharge current is a sensitive function of the filament temperature and surface area.

Since plasma density is proportional to the discharge current due to increases in the number of ionising collisions, it was decided to install an automatic feed-back circuit to monitor the discharge current and control the filament temperature. The circuit, which is described below in section 3.2.2, controls filament temperature by regulating the filament current, and thus maintains a constant discharge current in spite of variations in filament temperature and surface area, as the bombarding ions slowly sputter and thin the filament.

2.2 Probe Theory

In 1924, I. Langmuir pioneered the use of electric probes in plasma diagnostics and while simple to implement, the theory governing probe responses is very complicated. The probe itself is a conducting surface, usually planar-circular, cylindrical or spherical in shape, which is immersed in the plasma. By analysing the current drawn by the probe as a function of applied potential, one can determine various plasma parameters, for example, the electron temperature T_e, (a measure of the average energy of the plasma electrons), density n_e, the floating potential ϕ_f, and the plasma potential ϕ_p, (the space potential of the plasma, with respect to ground). Potentials used in

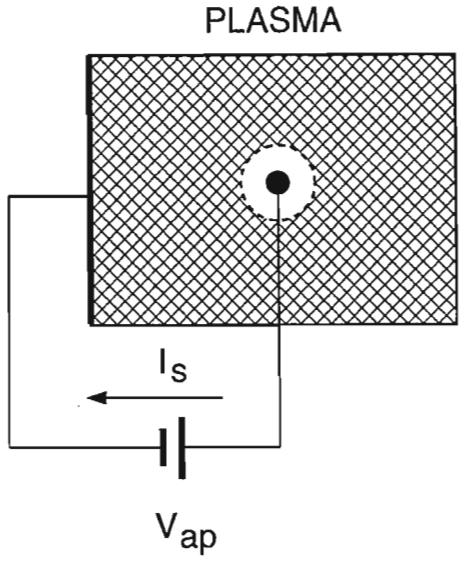

Figure 6: Simple probe circuit, shown to collect electron current (I_s)

plasma physics are calculated relative to the plasma potential. Details of this analysis will be given below.

There are two basic probe configurations, the double probe and the single, or Langmuir, probe. In the double probe configuration, the current is measured as a function of the applied potential difference between the two probes, whereas in the single probe configuration, the current is measured as a function of the potential difference between the probe and the chamber walls which are usually at ground potential.

The electron temperature T_e and density n_e influence the magnitude of the initial ion matrix sheath thickness and its behaviour. An examination of a probe theory used to determine the plasma parameters will be given below.

2.2.1 Analysis of the Langmuir Probe Current-Voltage Characteristic

The application of Langmuir probe theory to determine plasma parameters is complex and much discussed, with different formulae being applied for different plasma regimes. This discussion will be limited to plasmas typical of these experiments. Podgornyi [36] presents a simple theory of Langmuir probes in the single probe configuration, as shown in figure 6, where the applied potential $\phi = V_{ap}$.

This discussion is based upon the following assumptions:

1. Electron and ion densities are equal,
2. Electron and ion mean free paths are much larger than the probe radius,
3. Electron temperature is much larger than the ion temperature,
4. The probe radius is much larger than the Debye length,
5. The electrons and ions have a Maxwellian velocity distribution.
6. The charged particles move through the probe sheath without collisions.

If the region around a probe in which the electric field is concentrated is defined as the probe sheath, then the current collected by the probe is a sensitive function of the applied probe potential, and determined by the sum of the contributions of the negative and positive charge carriers entering the sheath.

When the currents to the probe are small, the scale length of the probe sheath width is given by the Debye length

$$\lambda_D = \sqrt{\frac{\epsilon_0 k T_e}{n_0 e^2}},$$

where T_e is the electron temperature and n_0 the plasma density.

For large current values, the thickness of the sheath increases and is then determined by the Child-Langmuir relation (equation 2) which describes the space-charge limited current between the probe surface and the plasma-sheath boundary:

$$I = \frac{4}{9}\epsilon_0 \left(\frac{2e}{m_e}\right)^{\frac{1}{2}} \frac{\phi^{\frac{3}{2}}}{x^2} A_p \tag{4}$$

I is the current to the probe, x the thickness of the sheath, A_p the surface area of the probe, and ϕ is the potential difference between the plasma and the probe.

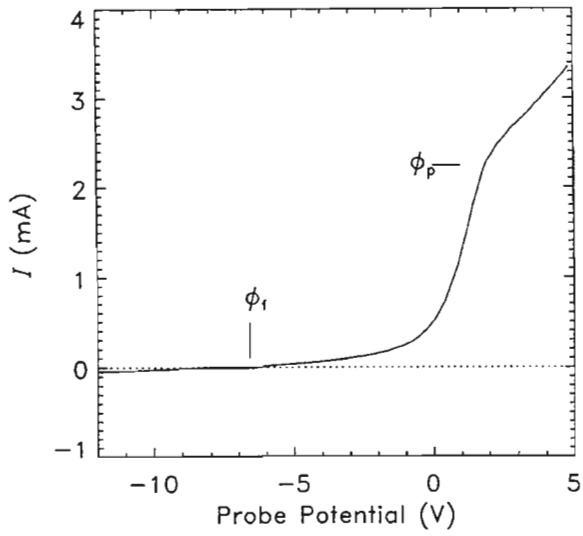

Figure 7: A typical Langmuir characteristic trace. Floating ϕ_f and plasma ϕ_p potentials indicated.

Only about $\sim \frac{kT_e}{2e}$ of the probe potential extends into the plasma. The rest is concentrated in the probe sheath, which accelerates the ions which enter it. This is important in plasmas in which the ion temperature T_i is much lower than the electron temperature T_e, since in this case the ions arrive at the probe sheath with a velocity as if their temperature were equal to $\frac{1}{2}T_e$. This follows from the Bohm Sheath Criterion which requires ions to enter the sheath with a velocity greater than the ion acoustic velocity, c_s. If the energy gained by ions approaching the sheath is $\frac{1}{2}m_i v_i^2 = e\phi$, the requirement that $v_i = c_s = \sqrt{\frac{kT_e}{m_i}}$ has $e\phi = \frac{1}{2}m_i v_i^2$, or $e\phi = \frac{1}{2}m_i \frac{kT_e}{m_i}$, hence $\phi = \frac{kT_e}{2e}$.

A typical Langmuir probe current-voltage characteristic trace is given in figure 7. At large negative applied potentials, ($|V| \gg kT_e$, where $V = \phi_p - \phi_{\text{probe}}$) the current is essentially independent of voltage. This is because the applied potential repels the electrons and the current is due entirely to flux of ions incident on the collecting surface. If $T_i \ll T_e$, then the saturation current is given by [36]

$$I = enA_p\sqrt{\frac{2kT_e}{m_i}} \tag{5}$$

where m_i is the ion mass.

As the probe potential is increased, electrons will start to be collected, first the energetic fast electrons, then the slower ones.

It is in this potential regime, where the electrons are first collected, that evidence of the ionizing primary electrons can be seen. From Hershkowitz [37], at low pressures ($< 10^{-5}$Torr), the primary electron contribution is visible as a straight line on the ion current portion of the I-V Langmuir trace. At higher pressures, the characteristic loses its straight-line shape, but primary electron contributions can still be inferred from the floating potential. When primary electrons are present, the floating potential (See below) is found to be more negative than its true value, found by balancing plasma ion currents with only plasma secondary electrons [37]: $\phi_{f0} = \phi_p - 5.4T_e$.

The magnitude of this floating potential is primarily determined by the electron temperature, and is given by [36]

$$\phi_f = \frac{kT_e}{2e} \cdot \ln\left[\frac{m_i}{m_e} \cdot \frac{T_e}{T_i}\right]. \tag{6}$$

As the probe potential is increased above the floating potential, the current becomes negative and exponentially dependant on applied potential. In this region the probe collects current due to electrons whose energies exceed the potential difference between the probe and the plasma. Since the electrons are assumed to have a Maxwellian energy distribution, the probe current density at a retarding potential V will be $e^{-\frac{eV}{kT_e}}$ times smaller than the electron saturation current density; the current density with no retarding field. Thus at applied probe potentials greater than ϕ_f the electron current is determined by

$$I = enA_p\bar{v}_e e^{-\frac{eV}{kT_e}} \tag{7}$$

where $\bar{v}_e = \sqrt{\frac{kT_e}{\pi m_e}}$, is the average (mean) electron velocity.

A further increase in the applied probe potential produces a sharp break in the trend of the characteristic and the current measured by the planar probe once again becomes relatively independent of the applied potential. The potential at which this

occurs is the plasma potential, ϕ_p. The increase in electron saturation current with further increases in potential is then due to the increasing thickness of the probe sheath as given by equation 4.

The electron temperature is determined easily by plotting the probe characteristics on a semi-logarithmic scale, whence equation 7 is expressed as

$$\ln I_e = -\frac{eV}{kT_e} + \ln(\bar{v}_e e n A_p).$$

Thus the gradient in this region is equal to $-\frac{e}{kT_e}$. The ion and electron density can then be determined from equation 5. A technique to analyse the Langmuir probe characteristic is presented by Carroll *et al* [38], and has been used to obtain the plasma parameters in this thesis. Their technique first determines the plasma potential ϕ_p by identifying the inflection point in the characteristic. Parabolic interpolation is used to determine the plasma potential with a resolution greater than the voltage step size. By defining a function which models the ion and electron currents drawn by the probe they use the Golden rule [39] to minimize the least square error to determine T_e and hence plasma density n_e from the ion saturation current, equation 5.

Plasma Parameters

In summary, it has been shown that by analysing the Langmuir Characteristic one can determine the plasma potential, ϕ_p, the ion density, n_e (and n_i, due to quasi-neutrality), and the electron temperature, T_e [36]. The plasma parameters pertaining to these experiments are presented in section 3.3.2.

2.2.2 Probe theory during the PSII process

During the PSII process the plasma is greatly disturbed and the beams of ions and electrons result in non-Maxwellian velocity distributions. Much has been written about probe theory in non-Maxwellian plasmas, and a full review is beyond the scope of this thesis. Instead, the results of the numeric simulation are used to verify the

use of probes in measuring PSII sheath behaviour.

2.3 PSII sheath theory

In the PSII process the target to be processed is immersed in a plasma and pulse-biased to a high negative potential (10-120kV). The PSII process is then characterised by three time scales which define the formation of the plasma sheath, and its subsequent evolution.

2.3.1 Time scales

There are three important timescales in this process which are used to describe the sheath formation and subsequent evolution.

1. The first timescale is determined by the electrons: When the pulse is first applied, the electrons react on a timescale of the order of the electron plasma period ($\tau_{\mathrm{pe}} = \sqrt{\frac{\epsilon_0 m_e}{n_e e^2}}$), and are "blown away", leaving behind a region with characteristic width S_0 containing only the more massive ions. This region is called the ion matrix sheath. In the experiments described below, the electron plasma period is typically of the order of $10ns$.
2. On a much longer timescale, of the order of the ion plasma period $\tau_{\mathrm{pi}} = \sqrt{\frac{\epsilon_0 m_i}{n_i e^2}}$ the ions start to move toward the target. In these experiments, the ion plasma period is about $1\mu s$. This period marks the end of the ion-matrix sheath phase.
3. On an even longer timescale the sheath edge S propagates outwards as the electrons continue moving away from the target so as to keep enough ions between them and the target to shield the target potential. Normally, the sheath would expand outward until it reaches that distance described by the steady state Child Law, equation 4. However in the actual PSII process the voltage pulse width is kept sufficiently short that the voltage is returned to zero before the steady state sheath forms. This is to prevent neighbouring sheaths from

reaching each other and affecting implantation uniformity.

The theory governing the ion matrix sheath formation and evolution is given in the following sections.

2.3.2 The Ion-matrix Sheath

Conrad [16] describes a model of ion-matrix sheath formation:
The potential profile is obtained from Poisson's equation

$$\frac{d^2}{dr^2}\phi + \frac{\alpha}{r}\frac{d}{dr}\phi = -\frac{1}{\epsilon_0}e(n_i - n_e) \tag{8}$$

where ϕ is the applied pulse potential, n_i and n_e the ion and electron densities, and α=0, 1 and 2 for planar, cylindrical and spherical geometries. Restricting the analysis to the ion-matrix sheath phase of sheath evolution, when the potential is applied to the electrode it is assumed that the plasma is of uniform density and $n_0 = n_i = n_e$. For the case of planar geometry the spatial variable r is measured from the surface of the electrode, while for cylindrical and spherical geometries, r is the radial distance from the centre of the electrode.

It is convenient to introduce dimensionless variables in terms of the electron temperature T_e and the Debye length λ_D. The substitutions

$$\begin{aligned} \tilde{\phi} &= \tfrac{e\phi}{kT_e}, & \tilde{r} &= \tfrac{r}{\lambda_D} \\ \tilde{n}_e &= \tfrac{n_e}{n_0} \quad and \quad \tilde{n}_i &= \tfrac{n_i}{n_0} \end{aligned} \tag{9}$$

yield the dimensionless Poisson's equation

$$\frac{d^2}{d\tilde{r}^2}\tilde{\phi} + \frac{\alpha}{\tilde{r}}\frac{d}{d\tilde{r}}\tilde{\phi} = -(\tilde{n}_i - \tilde{n}_e) \tag{10}$$

During the ion-matrix phase of the sheath evolution, the electron density in the region of interest is assumed to be zero, and the ion density is equal to the background density, so equation 10 reduces to

$$\frac{d^2}{d\tilde{r}^2}\tilde{\phi} + \frac{\alpha}{\tilde{r}}\frac{d}{d\tilde{r}}\tilde{\phi} = -1 \tag{11}$$

subject to the following boundary conditions:

1. The potential at the electrode position, r_0, must be equal to the applied potential ϕ_0, and
2. and the electric field must vanish at the sheath position, r_s.

Thus

$$\tilde{\phi} = \tilde{\phi}_0 \equiv \frac{e\phi_0}{kT_e} \quad \text{at} \quad \tilde{r} = \tilde{r}_0 \equiv \frac{r_0}{\lambda_D} \tag{12}$$

$$\frac{d}{d\tilde{r}}\tilde{\phi} = 0 \quad \text{at} \quad \tilde{r} = \tilde{r}_s \equiv \frac{r_s}{\lambda_D} \tag{13}$$

Solutions are found using standard ordinary differential equation techniques, and are:

Planar geometry:

$$\tilde{\phi}(\tilde{r}) = -\tilde{\phi}_0 + \tilde{r}_s(\tilde{r} - \tilde{r}_0) + (\tilde{r}_0^2 - \tilde{r}^2)/2 \tag{14}$$

Cylindrical geometry:

$$\tilde{\phi}(\tilde{r}) = -\tilde{\phi}_0 + (\tilde{r}_s^2/2)\ln(\tilde{r}/\tilde{r}_0) + (\tilde{r}_0^2 - \tilde{r}^2)/4 \tag{15}$$

Spherical geometry:

$$\tilde{\phi}(\tilde{r}) = -\tilde{\phi}_0 + (\tilde{r}_s^3/3)(1/\tilde{r}_0 - 1/\tilde{r}) + (\tilde{r}_0^2 - \tilde{r}^2)/6 \tag{16}$$

Expressions for the sheath position are found by setting the potential to zero in equations 14-16. By defining f to be the ratio of sheath radius to electrode radius, $f \equiv \tilde{r}_s/\tilde{r}_0 = r_s/r_0$, the results are

Planar geometry:

$$(f-1)^2 = 2\tilde{\phi}_0/\tilde{r}_0^2, \tag{17}$$

Cylindrical geometry:

$$f^2 \ln f^2 - f^2 + 1 = 4\tilde{\phi}_0/\tilde{r}_0^2, \tag{18}$$

Spherical geometry:

$$2f^3 - 3f^2 + 1 = 6\tilde{\phi}_0\tilde{r}_0^2. \tag{19}$$

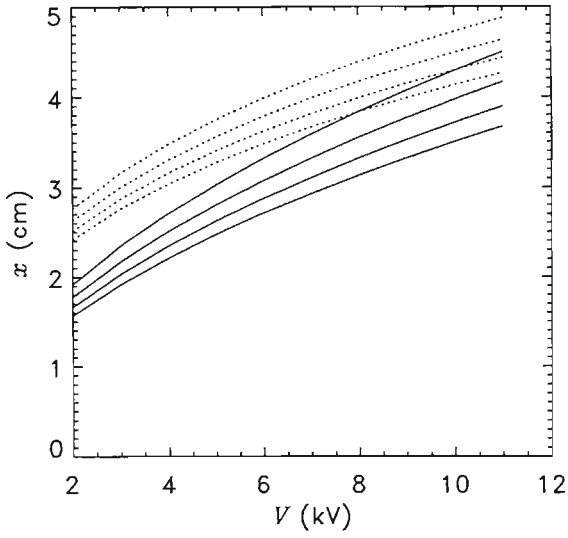

Figure 8: Planar and spherical ion-matrix sheath width as a function of target potential for various densities. Planar widths are shown dashed. Densities (from the top) are 6, 7, 8 and 9 $\times 10^8 \mathrm{cm}^{-3}$

Since all the experiments performed in this thesis can be approximated by planar or spherical geometries, all discussions will be limited to these two situations.

By setting $r_0 = 0$ in equation 14 and rewriting equations14 and 19 from dimensional units into physical quantities yields the following expressions

Planar:

$$r_s = (2\epsilon_0\phi_0/n_0e)^{\frac{1}{2}} \text{ or } r_s(\mathrm{cm}) = 1050[\phi_0(\mathrm{volts})/n_0(\mathrm{cm}^{-3})]^{\frac{1}{2}} \tag{20}$$

Spherical:

$$r_s \simeq (3\epsilon_0\phi_0 r_0/n_0e)^{\frac{1}{3}} \text{ or } r_s(\mathrm{cm}) \simeq 118\left(\frac{\phi_0(\mathrm{volts})r_0(\mathrm{cm})}{n_0(\mathrm{cm}^{-3})}\right)^{\frac{1}{3}} \tag{21}$$

Plotting equations 20 and 21 in figure 8, the dependence of steady state ion-matrix sheath width on target bias and density can be seen.

An analysis of ion-matrix sheath formation about more complex target shapes, in particular, concave and convex wedges, have been performed by Donnelly [40]

and Watterson [41]. By using numerical methods to solve Poisson's equation for the boundary conditions relevant to concave and convex wedges, they were able to conclude that with concave wedges, the sheath width increases by about 10% nearer the tip, where the ion currents would probably be smallest, but for convex wedges the sheath is about 25% thinner near the tip, suggesting increased ion current there.

2.3.3 Sheath Evolution

Numerous theories have been proposed to describe the evolution of the ion matrix sheath, once it has formed. Lieberman [42] proposes a one dimensional planar model describing sheath evolution due to the application of a voltage step [V=0, for t $<$ 0, t$>$t$_p$, and V $= -$V$_0$, 0 $\leq$t$\leq$t$_p$]. This model is based on the following assumptions:

1. The ion flow is collisionless,
2. Compared to the ions, electron motion is inertialess,
3. The applied voltage V$_0$ is much greater than T_e, so $\lambda_D \ll S_0$ and the sheath edge at S is abrupt,
4. During and after implantation, a quasi-static Child-law sheath forms,
5. The electric field is assumed to remain constant for ion motion through the sheath.

The Lieberman model solves the Child-Langmuir law [34] for space-charge limited emission quasi-statically,

$$j = \frac{4\epsilon_0}{9}\sqrt{\frac{2e}{M}}\frac{V^{\frac{3}{2}}}{S^2} \tag{22}$$

where j is the current density crossing the sheath edge, M is the mass of the ion, V is the magnitude of the applied potential, and S is the distance of the sheath edge from the target. Based on the assumption that

$$j = ne(\frac{d}{dt}S + \nu_d) \tag{23}$$

where ν_d is the ion drift velocity, Lieberman solves equations 22 and 23 with $\nu_d = c_s$, the ion acoustic speed. Scheuer [43]*et al* further simplified the Lieberman model by

assuming that $\nu_d = 0$, i.e. the ions are stationary until the sheath reaches them, and equations 22 and 23 are solved to give

$$\frac{d}{dt}S = \frac{4\epsilon_0}{9n}\sqrt{\frac{2}{eM}}\frac{V^{\frac{3}{2}}}{S^2} \tag{24}$$

for a planar geometry which is integrated analytically to yield

$$S = S_0\left[\frac{2}{3}\omega_{\rm pi}t + 1\right]^{\frac{1}{3}} \tag{25}$$

In their analysis they continue to treat the cylindrical and spherical cases, but only the spherical case will be presented here:

In spherical geometries, the Child-Langmuir relation is written as

$$j = \frac{4\epsilon_0}{9}\sqrt{\frac{2e}{M}}\frac{V^{\frac{3}{2}}}{r^2\alpha^2} \tag{26}$$

where α is given by Xia and Chan [44] as $\alpha^2 = \gamma^2 - 0.6\gamma^3 + 0.24\gamma^4 - 0.074\gamma^5$, where $\gamma = \ln(r/r_0)$, producing the following differential equation for sheath evolution in spherical geometries:

$$\frac{d}{dt}r = \frac{4\epsilon_0}{9n}\sqrt{\frac{2}{eM}}\frac{V^{\frac{3}{2}}}{r^2\alpha^2} \tag{27}$$

They present a solution for the normalised ion matrix sheath width ($\tilde{S}_0 = S_0/r_t$) as

$$\tilde{S}_0 \simeq (3A)^{\frac{1}{3}} + (1/2), \tag{28}$$

where $A = \frac{eV\lambda_D^2}{kT_e r_t^2}$, r_t the radius of the target.

Figure 9 shows a comparison between the theoretical planar and spherical sheath evolutions for various densities, produced by numerically integrating equations 24 and 27. This was performed using the Runge-Kutta method and an initial value for the ion matrix sheath thickness (equations 20 and 21) and a sufficiently short time step interval to ensure a smooth result.

Stewart and Lieberman [45] propose a one-dimensional planar model for voltage pulses with finite rise and fall times. By specifying a linear dependence of voltage

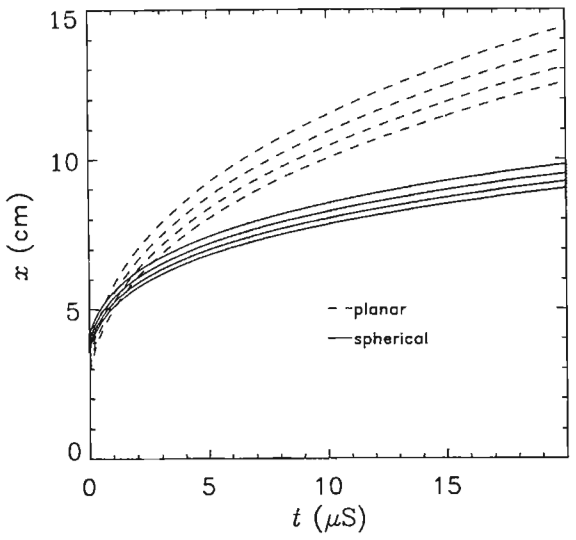

Figure 9: A comparison of planar and spherical sheath evolution. The dashed lines show planar sheath position vs time. Plots are for densities (from the top) of 6, 7, 8 and 9 $\times 10^8 \mathrm{cm}^{-3}$.

on rise, plateau and fall times, they produce analytical solutions for sheath position, instantaneous implantation current, energy distribution and total dose. A comparison with a numerical simulation is used to demonstrate how the accuracy of the model is characterised by the single parameter of the ratio of the ion flight time to the pulse rise time.

Emmert and Henry [46] have published results of their numerical simulation of one-dimensional sheath evolution in planar, cylindrical, and spherical geometries. By solving Poisson's equation coupled with the collisionless fluid equations, their simulation yields the current and energy spectrum of ions hitting the surface. They present comparisons of sheath position as calculated by their model with experimental data from argon plasma PSII experiments. They define the sheath edge to occur at the region where the electron density has dropped to 10% of its background value.

Vahedi *et al* [47]present a one-dimensional planar collisional model, in which the neutral gas pressure is assumed to be high enough for ion motion within the sheath to

be highly collisional. By starting with a sheath edge at r_s when $t = 0$, they solve the equations of motion for charged particles in an electric field. The ion-neutral mean free path is much smaller than the sheath thickness and collisions leave the ion at rest. They present a general model, and then obtain analytic expressions for the normal ion velocity distribution, sheath motion, ion flux at the target and other parameters for planar and spherical geometries. These results are compared with the Birdsall PDP1 and PDS1 Plasma Devices Planar (or Spherical) particle-in-cell simulations.

Xia and Chan [44] present experimental results and comparisons with their fluid dynamic model and the quasi-static model [16,45,47]. Investigating plasma parameters such as ion implantation current and implanted ion energy for spherical targets, they show differences between theirs and other models for short implantation times. For implantation times less than 10 ion plasma periods, their fluid-dynamic model presents results which differ from the conventional quasi-static model. These differences become greater as the target radius decreases, and comparisons with their experimental data favour their fluid-dynamic model. They also calculate the secondary electron emission coefficient for stainless steel and copper using two methods, showing how under PSII conditions, the coefficients are generally larger than under the atomically clean ultrahigh vacuum conditions used to produce the textbook tables.

Wood [48] outlines the effects of displacement current and multiple-pulse effects. Using analytic models and particle-in-cell simulations, Wood introduces the problems of (1) displacement current increasing the implant current while decreasing the implanted ion energy with respect to previous models, and (2) an ion depletion around the target due to a high pulse repetition rate leading to a reduced ion current and dose.

Wang*et al* [49] present another model of collisional sheath evolution and present results of sheath expansion velocity and sheath edge position as a function of time in planar geometries for various pressures. Using the ion current law derived by Rieman,

Ehlemann and Wiesemann [50], they produced a numeric model which covers the whole range, from collision-free to collision-dominated sheaths.

Thomas and Alport [51] present a two-ion fluid model. Based on a time-dependent fluid model, they present results applicable to nitrogen plasmas where the two charge species N^+ and N_2^+ are treated as two species of cold collisionless ion fluids. The density and velocity of the two ion species and sheath evolution for a range of ion mixtures are presented.

2.3.4 Two-dimensional sheaths

As of April 1994, reports of two-dimensional sheath formation and evolution had been fairly rare, with only the following publications having any relevance:

Donnelly and Watterson [40] used numerical methods to solve for the electric potential distribution in the stationary ion matrix sheath around wedge-shaped cathodes in plasmas.

Watterson [41] continued the investigation, finding that ion impact rates are 2.2 times greater near a square edge, and 3.6 times greater near a knife edge than at the planar surface. He also finds that the impact rate decreases to zero at the knife edge.

Lim *et al* [52] launch ion acoustic waves from 90 degree convex and concave corners. Their equi-phase contour results match closely with the results published by Donnelly and Watterson. This is one of the few experimental results applicable to PSII sheaths to have been published.

Sheridan and Alport [53,54] solve Poisson's equation numerically around a square bar, to produce results showing increased ion density and flux near the corner, in agreement the results published by Watterson.

Investigations into dose uniformity were performed by Conrad [30], where retained dose measurements were made at nine points on a spherical target. The target was one of four processed in a typical 2×2 unit-cell for an N×N bulk-processing batch. Rutherford backscattering spectrometry showed a retained dose of about 2.8×10^{17}

atoms cm^{-2}, with a root-mean-square variation of less than 15%.

Shamim *et al* [55] measured sheath evolution along three lines around a planar target. By measuring the electron current with a Langmuir probe along a line perpendicular to the target disk at its centre, at 45 degrees at the centre, and in the plane of the target, they noted an ellipsoid sheath shape, which tended to spherical at greater distances. They associated the sudden drop in the measured electron current with the passage of the sheath.

Faehl, de Volder and Wood [56] used a particle in cell simulation of a plasma consisting of electrons and N^+ ions. Current densities measured along the surfaces of various implantation morphologies were used to find dose and angle of incidence as a function of position. The targets investigated include long cylinders and bores in flat plates. Their bore implantation calculations suggest that while the bottom of the bore could still be implanted, the walls experience a low flux with high angles of incidence. Their inclusion of secondary electrons emitted from a target in a small-chamber configuration yielded no qualitative modification to sheath behaviour.

MunPyo Hong and G.A. Emmert [57] used fluid equations for the cold, collisionless ions and Poisson's equation to simulate the nonuniformly expanding plasma sheath around a square corner. Their results of ion density profiles along the y and $x = y$ axes and ion dose *vs.* position show increased ion dose near the corner, in agreement with previous results.

2.3.5 Recent developments in PSII sheath dynamics

More recently, Sheridan [58] investigated PSII into a deep plasma-filled cylindrical hole. He finds that the sheath does not conform (a conformal sheath would reflect the target geometry) to the hole unless the hole diameter is larger than the ion matrix overlap length (defined by $s_1 = \left(\frac{-4\epsilon_0\phi_{target}}{en_0}\right)^{\frac{1}{2}} = \sqrt{2}s_0$), and that ions impact the side walls of the hole at glancing angles.

Qin *et al* [59] derive a one dimensional multispecies collisionless dynamic sheath

model, based on singly charged ions and a square voltage pulse. They present results of sheath evolution and ion current density for a mixed argon helium plasma.

Sheridan and Goeckner [60] present a one dimensional collisional fluid model of a single ion species. They present results of sheath width, ion impact energy, ion flux and ion density for varying degrees of collisionality. The results are compared with experimental data.

Sheridan [61] presents a two dimensional two-fluid model of PSII into a trench. The potential structure in the sheath both focuses and bunches ions, creating an ion density pulse that travels down the sidewall of the trench.

Mukherjee *et al* [62] present experimental results of the current collected by an electrode immersed in a plasma during the PSII process. The results are compared with a model based on the concept of an expanding capacitor. Their results emphasize the role of displacement current in expanding sheaths.

Mukherjee and John [63] discuss experimental results of current collected by a disc electrode in a collisional plasma in ion sheath experiments. Their negative voltage pulse is characterized by a linear rise, followed by a constant voltage phase and then exponential decay. The measured currents to the electrode are compared to predictions from a dynamic collisional ion sheath model which is developed from the basic two-fluid equations. They find an agreement between the model and the experimental pulse rise and plateau times, but disagreement with the decay times.

Hong and Emmert [64] present a two-dimensional numeric fluid model of sheath dynamics around a square and a cross-shaped target. They calculate the angular distribution of the incident ions and demonstrate non-uniform ion doses. Specifically, they calculate that the incident ion dose peaks near, but not at, the convex corner and has a minimum at the concave corner.

Sun *et al* [65] present the results of a model developed to describe the propagation of the sheath inside a cylindrical target. Their results can be used to predict the final sheath extent for inner surface implantation of a cylindrical target.

Goeckner *et al* [66] present a discussion of collisional pulsed planar sheath dynamics.

Chapter 3

Experimental Arrangement

3.1 Ion - surface interaction

Since ions are implanted ballistically in PSII, the implantation depth is determined by the energy of the incident ions. In order to produce a specified implantation profile the concentration and depth of the implanted ions needs to be well controlled. The ion energy depends on the local space potential, the position of the ion, and its charge state. An argon plasma consists of singly charged ions, but nitrogen plasma ions have two charge states, N^+, and N_2^+. Ions that have initial positions beyond the ion-matrix sheath region after the pulse is applied reach the target with energies dependant on their ion charge state.

However, those ions that are within the ion matrix sheath when the pulse is applied will have an energy that is also dependant on their distance from the target. Since the local space potential increases from the target potential at the target, to zero at the ion-matrix sheath edge, the maximum energy an incident ion can have is dependant on the potential difference between the ions initial position and the target. Thus ions closer to the target will have lower implantation energies than ions at the sheath edge.

This could be important since for certain target geometries it is only ions that start

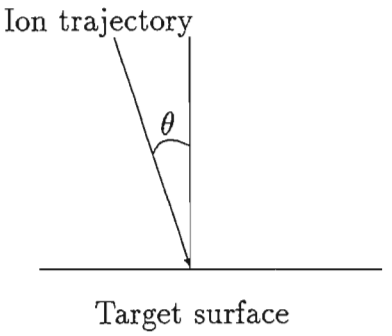

Figure 10: Ions incident on the target at non-normal ($\theta \neq 0°$) trajectories.

near the target which reach it with trajectories perpendicular to the surface. This can be seen from analysis into sheath formation around square corners [53, 54] and convex cathodes [40,41]. While one of the reported advantages of PSII over ion beam implantation has been its ability to implant with normal incidence simultaneously over the entire surface, this is only true for simple spherical targets. In targets with more complex structure, the electric field far away from the target (at the sheath edge, for example) does not reflect certain details of the target surface. In general, at large distances from the target the sheath front tends to have a spherical shape, irrespective of target shape. Thus while it is true that ions are accelerated along the electric field lines, which always intersect the target perpendicularly, the ion's momentum can cause it to deviate from the field line. This is especially true near sharp target structures, where sharp changes in electric field direction occur. Investigations into the problems of implanting square corners and holes have been mentioned above [57], where the difficulty of maintaining uniform ion dose near a corner and the implantation of bore walls is discussed [56].

3.1.1 Retained dose and sputtering

When ions arrive at the target surface with non-normal angles of incidence, $\theta \neq 0°$, figure 10, the problem of retained ion dose and surface sputtering occurs. As reported by Smidt and Sartwell [67] the retained dose is the number of ions retained

by the target. This value could be determined experimentally by such methods as Auger profiling or by Ruther Backscattering. However, they summarize a theoretical understanding of the factors influencing the concentration profile so that the profiles can be predicted. In brief, it is shown that for low ion fluences, the retained dose D$\sim \cos\theta$, while for higher fluences, D$\sim \cos^{\frac{8}{3}}\theta$. For grazing angles of incidence, not only is the retained dose low, but the target surface is eroded away by sputtering.

The tendency for ion momentum to cause the ion trajectory to deviate from the electric field line and thus strike the target surface at an angle $\theta \neq 0°$ is one reason why the PSII pulse width should be kept short. It is from the sheath edge that ions are uncovered and accelerated toward the target. The thicker the sheath, the less the sheath follows the geometry of the target. It is possible that by increasing the plasma density, the sheath width can be minimized, resulting in better sheath/target conformality and allowing sharper corners and holes to be processed. Unfortunately, this also results in greater target currents and heating, unless the pulse repetition rate is correspondingly reduced.

3.1.2 Secondary electron emission

Even if the ions are normally incident on the target, electrons can still be emitted from the material by secondary electron emission. The electron yield, γ, is the number of electrons ejected from the surface per incident ion, and is a function of ion energy, target material and surface cleanliness. A graph showing γ as a function of ion energy for various ions incident on tungsten is reproduced from Brown [2] in figure 11.

It has been suggested that electron yield under PSII operating conditions give values vastly different from the ultra-clean high-vacuum test conditions. Measurements of γ in PSII experiments give values of 2.5 – 4 [44] and 4.8 – 6.2 [68] for steel, for ~30kV ions.

These emitted electrons are then accelerated away from the target by its high negative potential and add to the electron flux of the sheath-displaced electrons. This

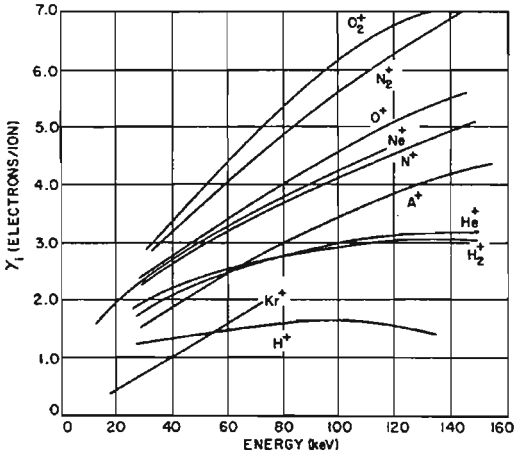

Fig. 7.40 Secondary electron emission coefficient from clean tungsten bombarded by H^+, Kr^+, H_2^+, He^+, A^+, N^+, Ne^+, O^+, N_2^+, and O_2^+.
L. N. Large (1963)
PHYPRO J3 V81 P1101

Figure 11: Graph showing γ as a function of ion energy for various ions incident on tungsten. Reproduced from Brown [2].

additional electron flux must also be taken into account when examining electron-wall interactions and associated X-ray production, for example.

Since the contribution to the measured current due to the outgoing electron current is indistinguishable from the contribution due to the incoming ions, a measurement of the total target current to investigate ion dose can only be used if the secondary electron component is taken into account.

3.2 Apparatus

For clarity, the components of the apparatus used in these experiments will be grouped according to function and described separately in the sub-sections below.

Section 3.2.1 describes the physical plasma chamber and components, section 3.2.2 describes the control circuit used to maintain constant plasma density, while the probe hardware is described in section 3.2.3. Section 3.2.4 describes the high-voltage power

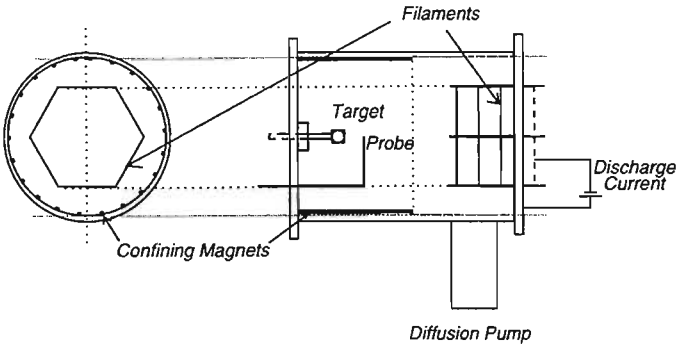

Figure 12: Front and side views of the plasma chamber, showing the target holder in relation to the filaments and the Langmuir probe.

supply used to pulse the target and section 3.2.5 describes the hardware and software used to monitor plasma characteristics and capture probe data. Section 3.3 discusses the associated experimental results.

Argon was used throughout these experiments, even though most PSII applications use nitrogen. Argon has only one charge state and forms a more stable and predictable plasma. Since this thesis is investigating sheath phenomena, not the target's metallurgical properties, argon is a more appropriate choice. The typical plasma parameters of these experiments are given and discussed in section 3.3.2.

3.2.1 Plasma Chamber

Chamber description

The experiments were performed in a cylindrical aluminium-alloy chamber 0.68m long and 0.45m in diameter, shown in figure 12. The end flanges house electrical lead-throughs for the filament and discharge power supplies, Langmuir probes and observation windows. The device was evacuated to a base pressure of about 10^{-7}Torr and has an argon operating pressure of about 10^{-4}Torr. The inside walls of the chamber were lined with a water-cooled copper jacket which protect a large number of ceramic magnets arranged in the usual multidipole magnetic cusp configuration to

improve the confinement of primary plasma electrons [69]. While the magnetic field due to the confining magnets was not explicitly measured, it is has been shown that it does not penetrate more than a few centimetres into the chamber [70]. Thus there should be no magnetic field at the target, or in the regions where sheath phenomena were investigated.

The discharge is produced by a constant potential of 60V that is applied between the chamber walls and three rings of ohmically heated tungsten filaments. An electronic feed-back circuit (see section 3.2.2) maintained the discharge current at a constant preset value of (typically) 500mA.

Chamber cooling

Any metal object exposed to the plasma in the chamber is heated by radiant energy from the filaments, and by ion and electron bombardment, so cooling needs to be provided. In the chamber walls and flanges this cooling is achieved by circulating cold water through copper pipes thermally bonded to their surfaces.

A separate external cooling system was used to pump refrigerated non-conducting transformer oil through the base of the target holder.

3.2.2 Plasma control circuit

Early in the experimental procedure it became apparent that the discharge current tended to decrease by nearly 50% during the extended 50–70 minute experimental runs. This decrease can be understood in terms of reduced filament surface area as the tungsten evaporates or is sputtered away by ion bombardment. Since the plasma density is a strong function of this discharge current, it was decided to use a feedback control circuit to maintain a constant discharge current, and hence plasma density.

Figure 13 shows the discharge control circuit which maintains a constant discharge current I_D, by regulating the filament potential V_f. The filament supply was configured so that its output voltage is programmed by an external remote resistor

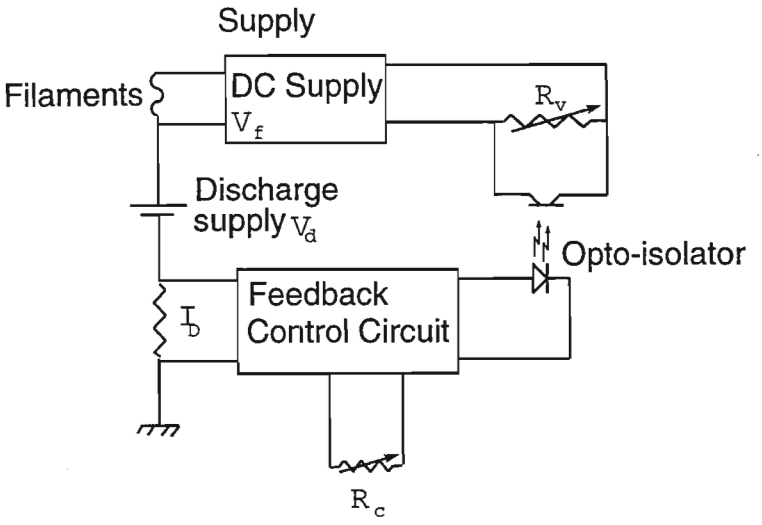

Figure 13: Discharge control circuit.

R_v.

The automatic control of R_v is achieved by connecting the phototransistor output of an opto-isolator in parallel with R_v. Thus when the opto-isolator LED switches on, the phototransistor begins to conduct, with a conductivity proportional to the brightness of the LED, thereby decreasing the effective R_v and hence V_f.

The discharge current can be monitored by measuring the voltage drop across a low-valued (a few ohms) shunt resistor in the 60V discharge power supply. This voltage drop is compared with the voltage drop across a second external variable resistor R_c. If the discharge current is greater than the preset value determined by R_c, the opto-isolator phototransistor is turned on by an amount proportional to the difference between the actual discharge current and the control value. This in turn decreases the effective R_v and hence the filament voltage so tending to reduce the discharge current back towards ite preset value. The reverse effect happens when the measured discharge current is less than it preset value.

This circuit also has two additional advantages (1) it can shut down the plasma

during a high current break down, and (2) the constant voltage control of the filament power supply prevents its voltage from increasing too high and burning out the filaments. This would happen when the discharge current drops to zero, due to a failure in either the neutral gas supply or the discharge current supply.

3.2.3 The Probe

The Langmuir probe projects into the chamber via a suitable electrical feed-through with viton 'O'-ring vacuum seals to allow probe manipulation. The probe was moved by two computer controlled stepper-motors which could simultaneously hold and independently move the probe axially along the chamber or radially across it. The probe itself was a 3.5mm tantalum disk on the end of a shorter (18.7 cm) shaft mounted perpendicular to the major shaft. The probe assembly is shown in figure 32, chapter 4.

The stepper-motors both require 200 steps per revolution, with gear ratios chosen to give 1000 steps per cm axially, and 84 steps per degree radially. The radial distance of the probe tip from the target surface is given by the length of the chord. The stepper gearing was tested and found to have some backlash which meant that the motors had to be stepped a small amount in the new direction before the probe tip moved. The effects of this backlash are quite visible in figures 24 through 26, where the features of the dashed lines (which are repeat scans in the reverse direction) are apparently spatially separated from those of the solid lines.

Thus since the mechanical backlash was significant, in the two-dimensional scans discussed later, the probe was systematically moved beyond a turn around point to take up the slack in the mechanical gearing at the beginning of every scan line.

To verify that the probe could be returned to the same position, a requirement of the large-area grid scanning pattern needed later, the probe was driven backwards and forwards over its full range about 200 times. It was verified that the probe returned to the same position after every scan.

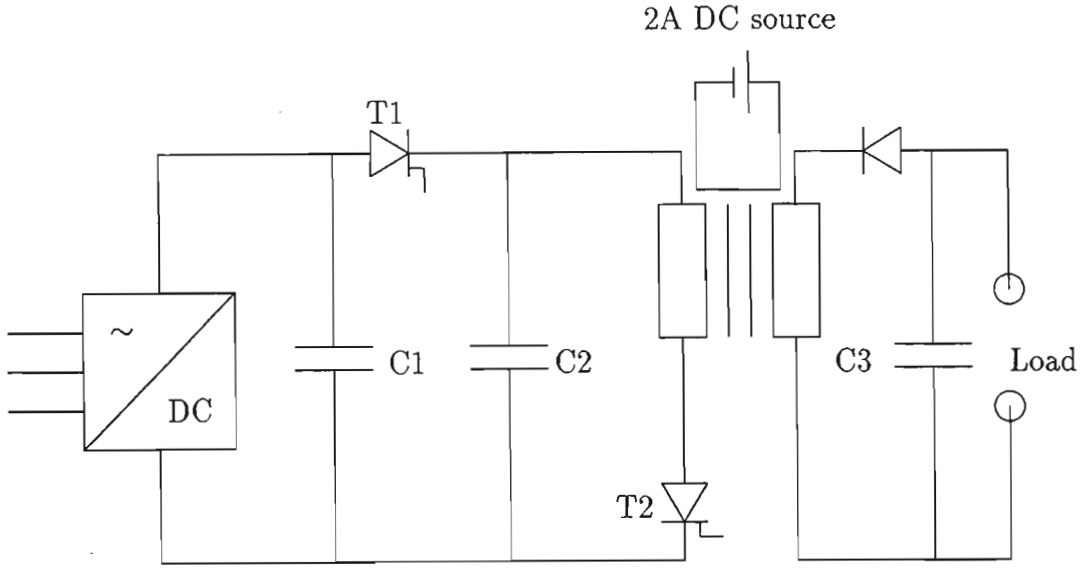

Figure 14: Basic circuit diagram of the H.V. power supply

3.2.4 The PSII Power supply

The power supply used to pulse the targets in the following sections was designed by Prof. H. von Bergman, Dr P. Swart and H. Tromp from Stelsels Lab, Rand Afrikaans University, and constructed by Mark Notcutt and Adriaan Vorster. A basic circuit diagram of which is given in figure 14.

Circuit operation

From Notcutt's report [71], the operation of the circuit is as follows:
The three-phase 380V AC maximum input signal is rectified by a bridge diode to charge the source capacitor C1 to 500V DC. The primary capacitor C2 is resonantly charged when the charging thyristor T1 is switched closed for a period of 200μs. The resultant voltage doubling develops a maximum of 1kV across C2. After the charging thyristor opens, the discharge thyristor T2 is closed allowing all the energy in the primary capacitor to discharge into the primary transformer winding where the pulse

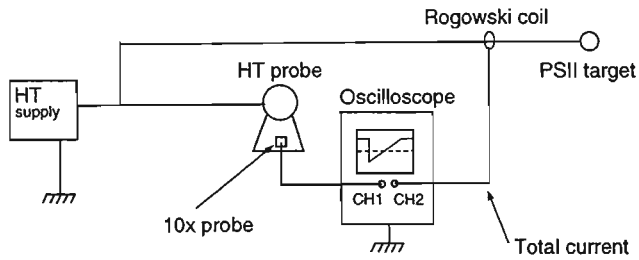

Figure 15: Circuit showing connections between the PSII-pulse power supply and associated measurement instruments.

in the secondary winding charges the secondary capacitor. The secondary capacitor is rectified by a fast diode bank, and discharged into the load. A one turn coil carrying a DC current of 2A in the opposite sense to the primary current is used to reset the core.

Circuit calibration

The output of the HT power supply, as measured by digitising the output of a Power 2000 2000:1 HT probe coupled to a scope 10× probe, is shown in figure 16. The circuit showing the connections between the probe and the digital oscilloscope (HP 54502A) is shown in figure 15.

To calibrate the probe a P6015 High-Voltage 1000× attenuator probe was borrowed from the Electrical Engineering high-voltage laboratory. This probe was used without dielectric fluid as the voltage was not expected to exceed 20 kV. The voltage output from this probe is shown in figure 17. The calibration factor required was obtained by comparing the output voltage measured by both probes. The calibration factor, calculated by dividing the two waveforms is shown in figure 18. The relatively constant calibration factor indicates that the two probes have similar frequency responses with some differences appearing at $0 \leq t < 20\mu s$ when the voltage waveform has a higher temporal variation. The final results measured were not 20

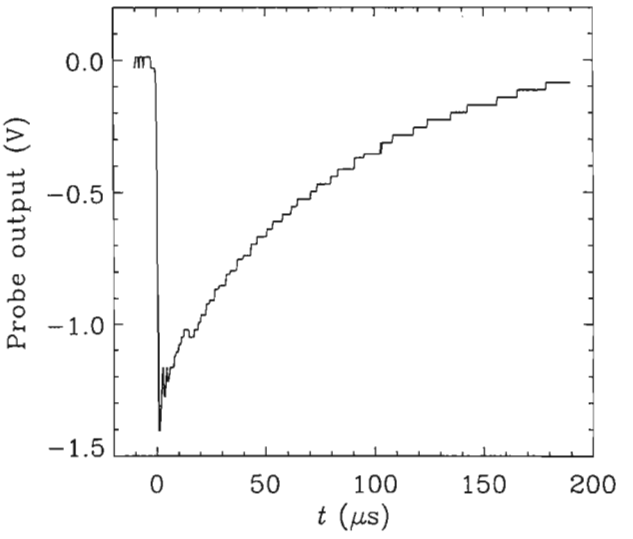

Figure 16: Voltage output from the Power 2000 probe.

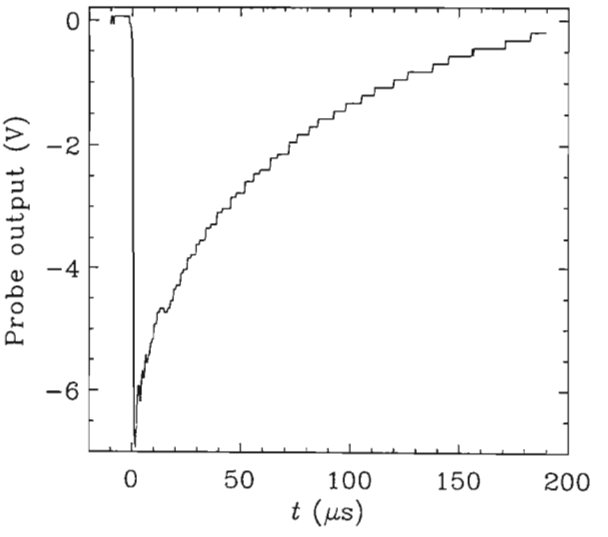

Figure 17: Voltage output from the P6015 probe

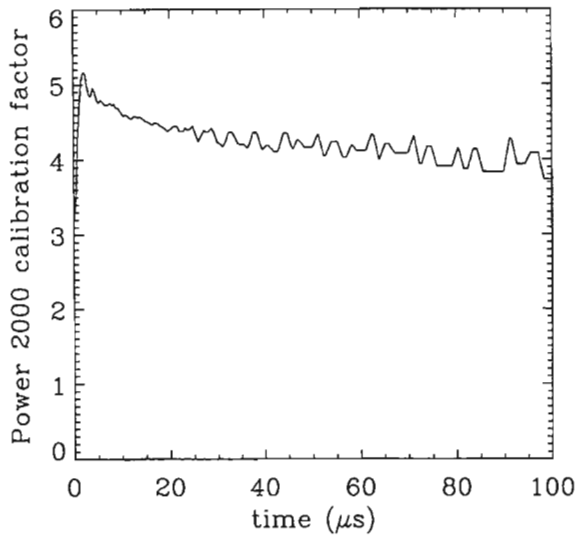

Figure 18: Probe calibration graph comparing Power 2000 and P6015 probe outputs. Result graphed is $P6015_{output}/Power2000_{output}$.

000:1, because the dome was not immersed in oil.

The time constant of the pulse ($\tau = RC$) was determined to be 1.7×10^{-4}s, or 80 ion plasma periods.

Total target current measurements

The total current to the target was measured using a Rogowski coil having a sensitivity of 0.025V/A. A calibrated current and voltage *vs* time graph is shown in figure 19. This figure shows the large initial current ($\sim$ 1.5A) that occurs in the first 20μs, a characteristic of the PSII process.

3.2.5 Data Acquisition

Most of the data presented in this thesis was acquired using one or more of the following devices: a HP54502A oscilloscope, Keithley 199 scanner and a Keithley 617 electrometer.

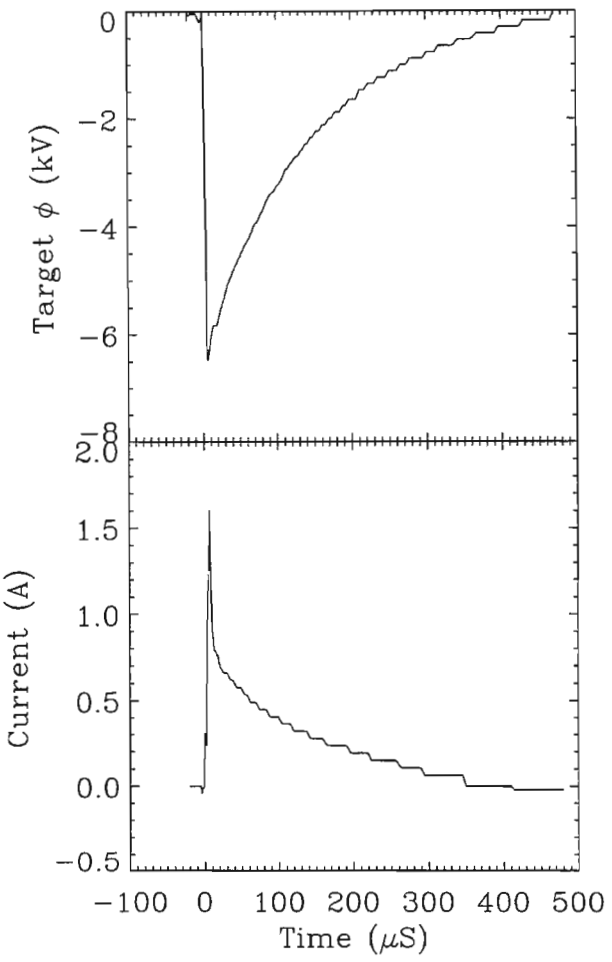

Figure 19: Total current and pulse voltage applied to the target.

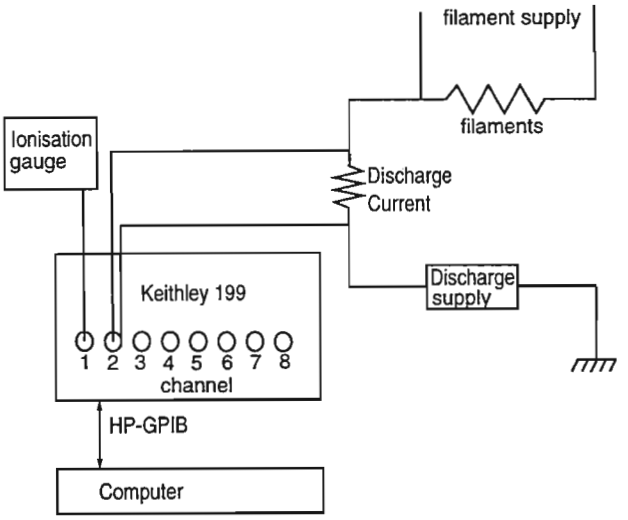

Figure 20: Figure showing the Keithley scanner being used to record various parameters

The Hewlett Packard Digitising Oscilloscope

Time varying data, such as the saturation traces measured during the high-voltage pulse, were captured on a digital oscilloscope (see figure 15 for connections).

The HP oscilloscope is capable of sampling at up to 400MSa/s with a real-time single shot bandwidth of up to 100MHz. Each trace captured was 500 data points long, with a resolution of 7 bits, i.e. a resolution of 0.8%.

The oscilloscope is connected to the computer by the HP-IB data exchange system, which facilitates digital data transfer between multiple connected devices.

The Keithley 199 Scanner and 617 Electrometer

The Keithley scanner and electrometer (also connected via the HP-IB bus) can be used to measure resistance, potential and current. In addition, the electrometer also includes a programmable voltage source.

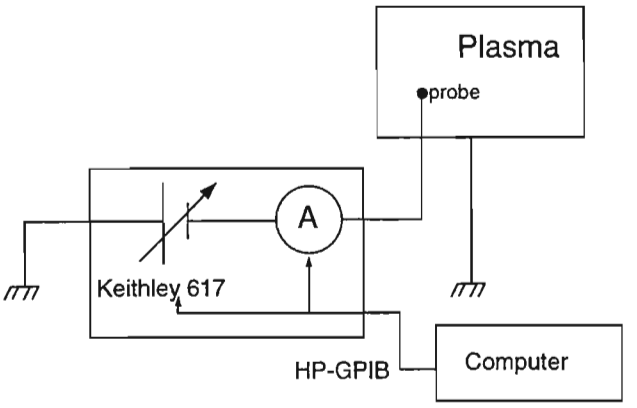

Figure 21: Figure showing the Keithley electrometer being used to record Langmuir traces

The scanner is a 6-digit voltmeter, with eight inputs. By selecting an input channel, the operator can remotely record several different measurements. For example figure 20 shows the scanner connected to the output of the pressure gauge, to record pressure, and the potential drop across the discharge shunt resistor which is proportional to the discharge current.

The programmable voltage source of the electrometer together with its current measuring capability was a convenient way to record the Langmuir characteristic from which the plasma parameters were calculated. The circuit used is shown in figure 21. This device can measure an input with a precision of greater than 1 in 10^3, or 0.1%.

Data acquisition and processing

All data was acquired from the HP54502A oscilloscope, the Keithley scanner and electrometer using the ASYST scientific language. The routines used to analyse the Langmuir characteristics to determine the plasma parameters and to control the stepper motors were also written in ASYST. Additional processing to examine the

recorded data and to generate the figures used in this thesis was performed in IDL[1] (Interactive Data Language).

Data capture

The ion and electron saturation current traces were produced by capturing them on the oscilloscope and then downloading the data to the computer. Langmuir characteristic sweeps were obtained by measuring the current recorded by the Keithley programmable electrometer as its voltage source was swept (typically) from -30 to $+20V$ in steps of 170 to 500mV, depending on circumstances. Thus the electrometer was used to both apply a varying voltage to the Langmuir probe and also to measure the current drawn by it (figure 21). The plasma parameters and sheath position were calculated by processing the Langmuir probe sweep data and saturation current data respectively.

In the process of building an external saturation current bias supply, it was discovered that the recording circuitry was extremely sensitive to the RF noise generated by the HV power-supply. Thus all cabling is shielded by using co-axial cables and the external bias supply, consisting of a DC-battery pack and shunt resistor with connections for measuring voltage drop, was shielded by an aluminium enclosure.

3.3 Plasma Diagnostics

This section presents the experimental measurements of the plasma parameters discussed in section 2.2.1. These results are representative of the steady state operating conditions under which the main sheath observation experiments were performed and includes a section on the interpretation of the saturation current traces.

[1]IDL, by Research Systems, Inc., 777 29th Street, Suite 302, Boulder, CO 80303. Ph: (303) 786-9900, Fax: (303) 786-9909, email: info@rsinc.com

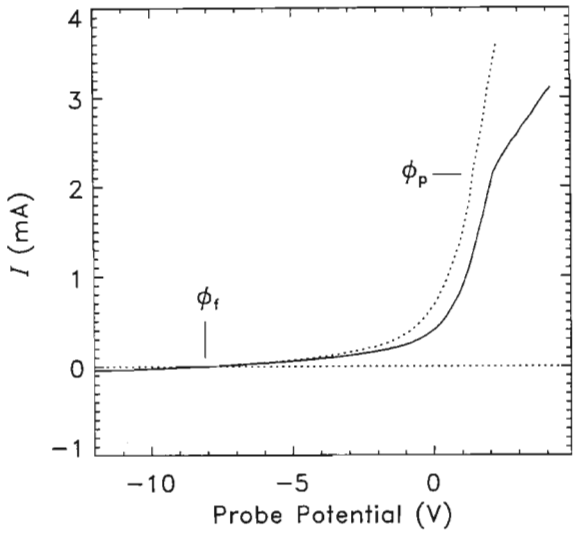

Figure 22: Langmuir characteristic trace with a clean probe, the trace measured with a dirty probe is drawn with a dotted line

3.3.1 Langmuir probe maintenance

Since a biased Langmuir probe draws an electric current from the plasma, its successful operation depends on the electrical properties of the probe surface. To ensure reliable measurements it is necessary to keep the surface electrically clean. In practice the probe was cleaned at the start of each experimental session by biasing the probe to about 120V DC. In this way it was heated by electron bombardment, until it glowed a visible orange. Failure to follow this procedure adversely affects the probes performance, as can be seen in the following figure.

Figure 22 is a typical Langmuir characteristic trace, with the plasma potential ϕ_p and the floating potential ϕ_f clearly marked. The dotted line shows the characteristic Langmuir trace before the probe was cleaned. It is visible how the dirty probe surface degrades the measurement: The 'kink' in the trace, which is the characteristic used to find the plasma potential, is not as clearly discernible in the dotted line.

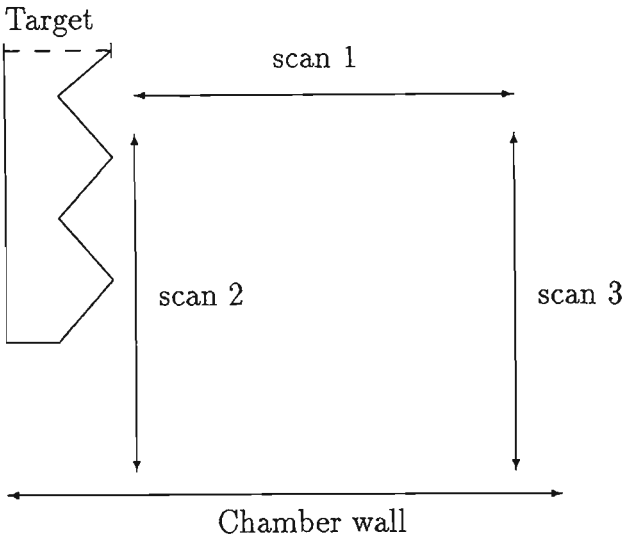

Figure 23: Scanning geometry used for the measurement of steady state parameters.

3.3.2 Steady state plasma conditions

The steady state plasma conditions were determined by analysing Langmuir probe characteristics obtained as the probe was moved incrementally along three representative lines in the plasma chamber. The scanning layout is presented in figure 23.

The Langmuir traces were taken at 2.5 mm intervals in the axial direction, and 2.5 degree (8 mm) intervals in the radial direction. The measurements were recorded by initially moving the probe in one scan direction, and then repeated while returning the probe back to its initial position. This was performed to check reproducibility and to ensure that the plasma- and probe surface conditions were not varying during the scan, which could take 90 minutes. In figures 24, 25 and 26, the forward scan is drawn with solid lines, while the reverse scan is drawn with a dashed line. Hysteresis due to backlash in the probe gearing is clearly visible in figures 25 and 26. This hysteresis problem can be avoided by scanning in only one direction.

No evidence of primary electrons were visible in the Langmuir characteristics. This is because the primary electrons are expected to occur in those regions where the filaments are closest to the chamber walls, i.e. in the last 20 cm of the chamber,

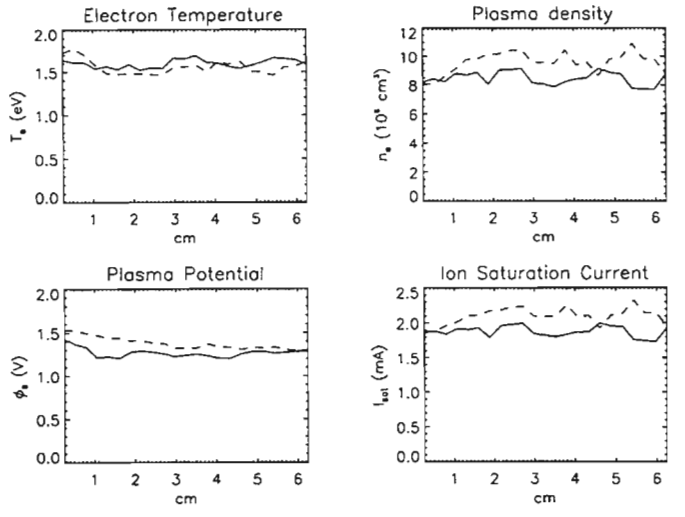

Figure 24: Steady state plasma parameters along line 1 corresponding to the concave region of the target shown in figure 23.

furtherest away from the probe. Since the probe drive mechanism never brought the probe closer than 40 cm to the filaments, it is not surprising that high primary electron densities were not observed.

Figures 24, 25 and 26 show electron temperature T_e, electron density n_e, plasma potential ϕ_p and ion saturation current along the three scan lines.

Figure 24 shows the conditions along scan line (1) corresponding to the axial direction. Figure 25 is along line (2), which represents a radial scan from the target to the chamber wall. Figure 26 shows the results along line (3) corresponding to a radial scan near the centre of the chamber. In all figures, the dashed lines show the parameters measured for the return scans.

The plasma parameters measured will now be discussed:

Child-Langmuir sheaths

The presence of the Child-Langmuir sheath which forms around conductors is clearly visible in the data that is described in the following subsections. Most clearly visible

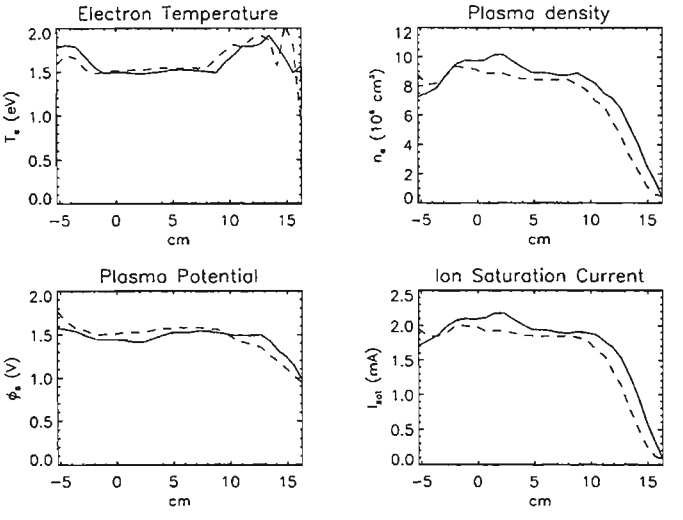

Figure 25: Steady state plasma parameters along line 2 corresponding to the region close to the target shown in figure 23. The chamber wall is at 15 cm.

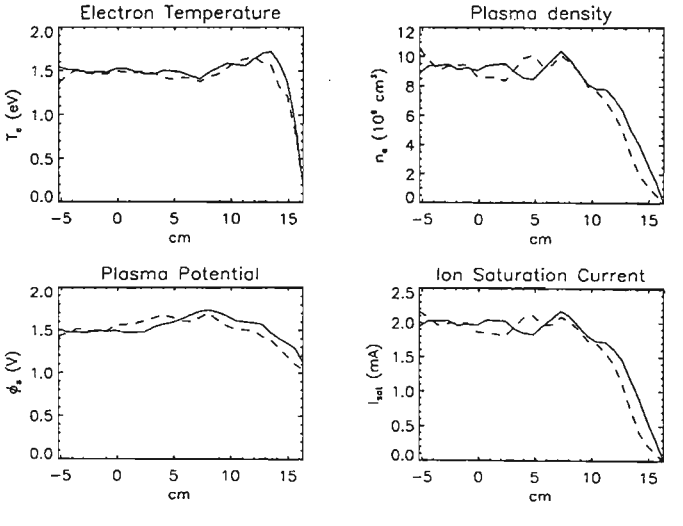

Figure 26: Steady state plasma parameters along line 3 corresponding to the region far from the target shown in figure 23. The chamber wall is at 15 cm.

is the decrease in density and plasma potential as the probe approaches the grounded wall and target.

Electron Temperature

The electron temperature is basically constant at about 1.5 eV, but localised increases near the conductors are visible. This is seen in figure 25, which shows the localised increases near the target (at $x = -5$cm) and near the wall (at $x = 15$cm).

Plasma density

The plasma density is reasonably constant at around 9×10^8 cm^{-3}. Deviations occur near conductors when the density decreases, dropping to zero at the chamber walls.

Plasma potential

The plasma potential is also reasonably constant, only deviating significantly from 1.5V near the chamber walls.

Ion saturation current

The plasma density is calculated directly from the ion saturation current (see equation 5 5), since quasineutrality is assumed to be valid.

3.3.3 Interpreting the saturation current graphs

Most of the experimental information presented in this thesis is determined by measuring ion and electron saturation currents and so it is important to have a good understanding of the nature and origin of these currents, and some idea of what information can be extracted from them.

Based on the results obtained in section 2.2.1, the following sections discuss the use of a planar probe in the experiments, and the effects of the spherical sheath which

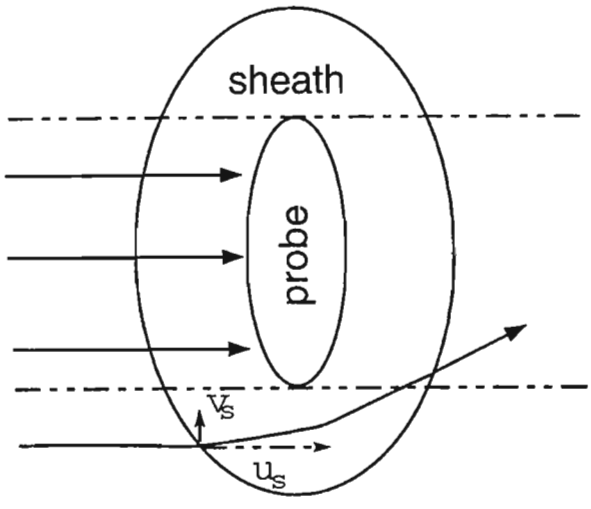

Figure 27: For particles with velocities $u_s \gg v_s$, only those particles with straight-line trajectories which intersect the probe itself are collected.

forms around it, ending with a discussion of what can be said about the saturation currents.

Measurement of saturation currents

The probe used in the following experiments was a Tantalum disk, 3.5mm in diameter, with the conducting surfaces parallel to the target. When used with the complex saw-tooth target, this configuration presents the maximum surface area to the target. Thus the high-energy charge carriers which are repelled from and attracted to the target strike the probe with effectively perpendicular velocities, thereby satisfying one of the assumptions made in the probe theory.

This has special relevance during the PSII process, when the charge carriers are accelerated toward or away from the target and the resultant velocity vector has large perpendicular and small tangential components. Under these circumstances the high velocity particles have velocity vectors about normal to the probe surface.

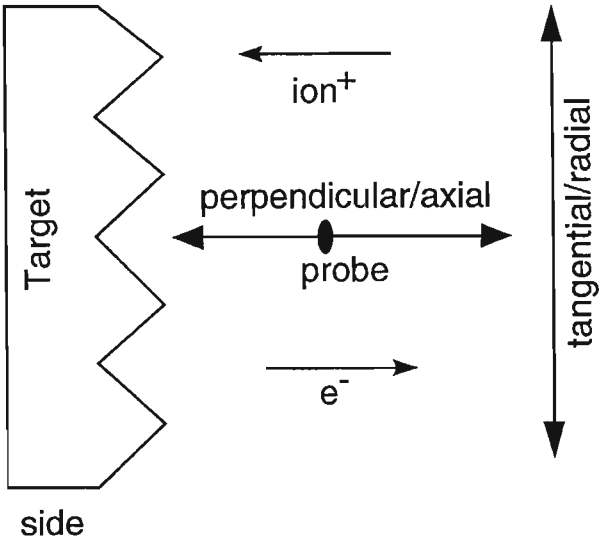

Figure 28: Diagram showing definitions of tangential and perpendicular velocity components.

Equation 4 gives an estimated sheath diameter of about 4mm, which compared to the probe diameter of 3.5mm ($\sim$ 6 Debye lengths) and thickness of 0.3mm, would result in a sheath which is more spherical than planar. However the assumption that the charge carriers are accelerated to high energies by the PSII process means that the particles are not deviated much from their straight line trajectories by the probe sheath. For this reason, only particles with straight-line trajectories which intersect the probe itself are collected (figure 27). This occurs in the experiments with the complex target, figure 28, the spherical target, and in front of the square face of the rectangular target, where the plane of the probe is parallel to the sheath.

Interpreting the results

Clearly, during the PSII process the plasma is severely disturbed. Specifically, the propagating sheath produces accelerated beams of electrons and ions resulting is a strongly non-Maxwellian plasma at the probe location. Thus variations in the

particle velocity distribution will have a strong influence on the saturation currents measured. However, by looking at results from particle simulations, it will be shown that a transition in the measured flux collected by a probe can be used to diagnose the sheath evolution.

Chapter 4

Experimental Procedure

In the course of this investigation, three targets were investigated. Each target was selected because of its specific geometrical configurations.

Since this report uses ion and electron saturation currents as diagnostic tools, it is important to verify the validity of the assumptions made about them in chapter 3. This is especially true for the ion saturation current which is used here for the first time. These verifications are performed by comparing the experimental data with a numerical particle-in-cell simulation. Thus the first target to be discussed is spherical, a geometry favouring comparison with the simulation results. The simulation is based on the 1-D Birdsall code, PDS-1, modified and run by Mark Harmer[1] to explicitly calculate ion and electron saturation currents.

The second target discussed is a rectangular block, a configuration important to, for example, the automotive industry and the processing of drill bits and pierce punches.

The final target discussed is a relatively complex shaped saw-tooth target having regions which are both concave and convex and thus representative of a gear with regularly placed teeth, a typical industrial application.

[1]Former Research Assistant at UND, presently at University of Auckland, Auckland, New Zealand

4.1 Experiment and Simulation

Reading through the literature on reports related to PSII, there are no experimental results presented of measurements of ion density during the PSII process. While there are published results which include ion current data, they are all of a theoretical nature, either from computer simulation, numeric or analytical calculation. In the PSII process the ion distribution determines the:

1. ion current to the target, representative of the ion dose to the target,
2. the ion flux through any spatial region in the plasma, and
3. the ion density at any given point in the plasma.

This thesis describes experimental measurements of ion saturation currents, used as a diagnostic tool to identify the effects of target geometry on plasma behaviour, and hence ion doses.

A particle-in-cell numeric simulation based on the PDS-1 Birdsall one-dimensional spherical code was used to simulate the experiments and produce detailed plasma information including ion and electron saturation currents, ion and electron densities, and velocity histograms and potential profiles. These results were used to assist in the analysis of the experimental data and to justify the use of ion and electron saturation currents as measurement tools.

4.2 The Spherical Target

This target is a stainless steel sphere 7.7cm in diameter. The target and scanning geometry is shown below in figure 29. By scanning axially along a line away from the target, sheath formation and evolution can be measured.

A spherical target was used instead of a planar target to compare with the simulation code because the former produced a sheath configuration that more closely approximates the spherical shape of the simulation code. The planar target only produced a planar sheath for a short distance from the target.

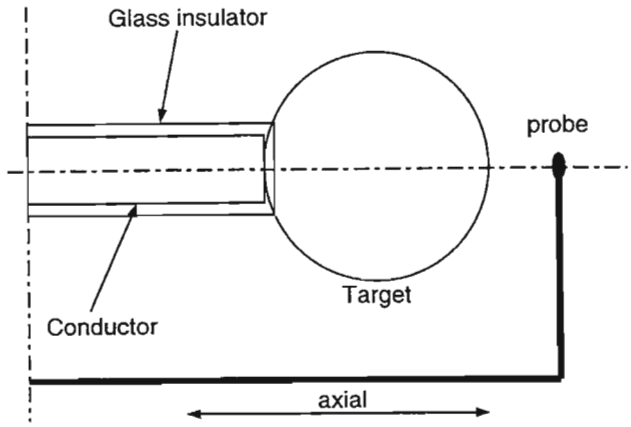

Figure 29: The spherical target, including probe access arrangement

4.3 The Rectangular Target

This target is a regular rectangular stainless steel block, 8 cm long, 2cm wide and 2 cm high. The target construction is shown in figure 30 and the corresponding scan area is shown in figure 31.

4.4 The Complex Target

Machined from brass, this target is 11.2cm wide and 6.8cm high. The horizontal cross-section is saw-toothed, where each regular tooth is 2.8cm wide and 1.5cm high. There are four teeth across the target, forming three concave and four convex regions. The target is shown in figure 32 together with the scanning layout in figure 33.

4.5 Data Measurement

All the saturation current data presented in this report was captured by measuring the current collected by a Langmuir probe immersed in the plasma. Typically, the

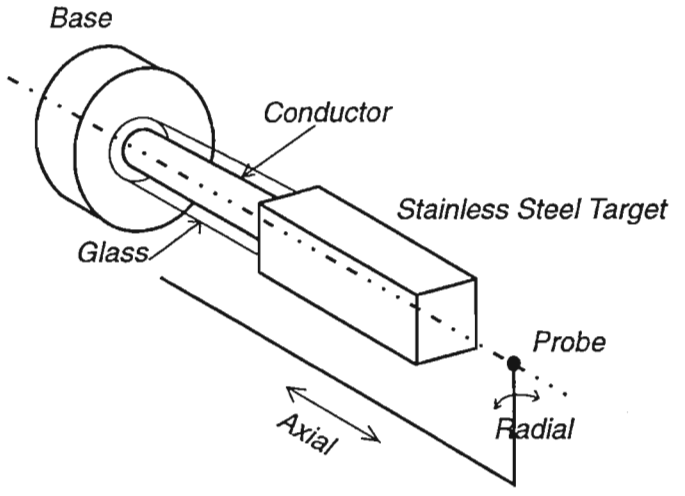

Figure 30: The rectangular target, including probe access arrangement

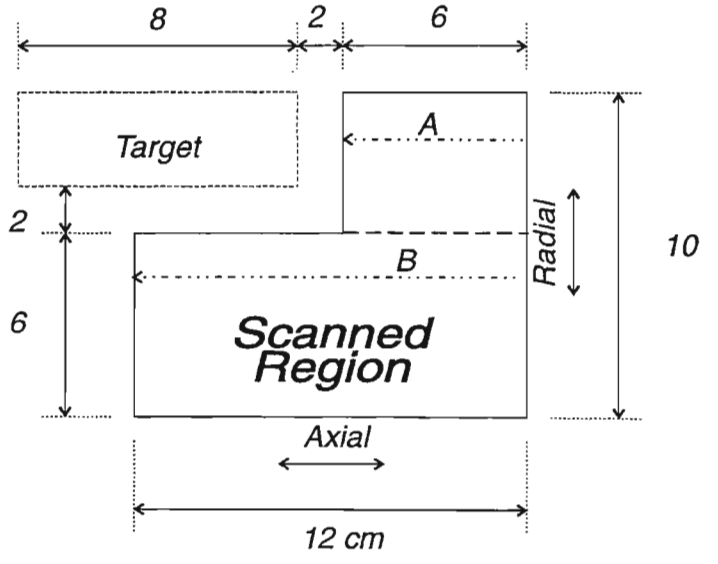

Figure 31: Scanning layout for the rectangular target

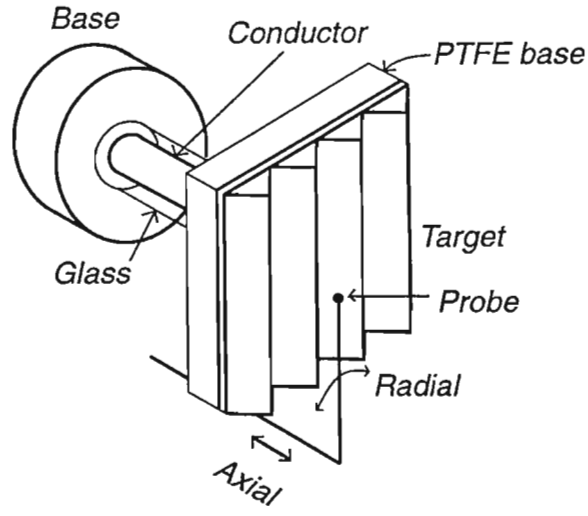

Figure 32: The complex target, including probe access arrangement

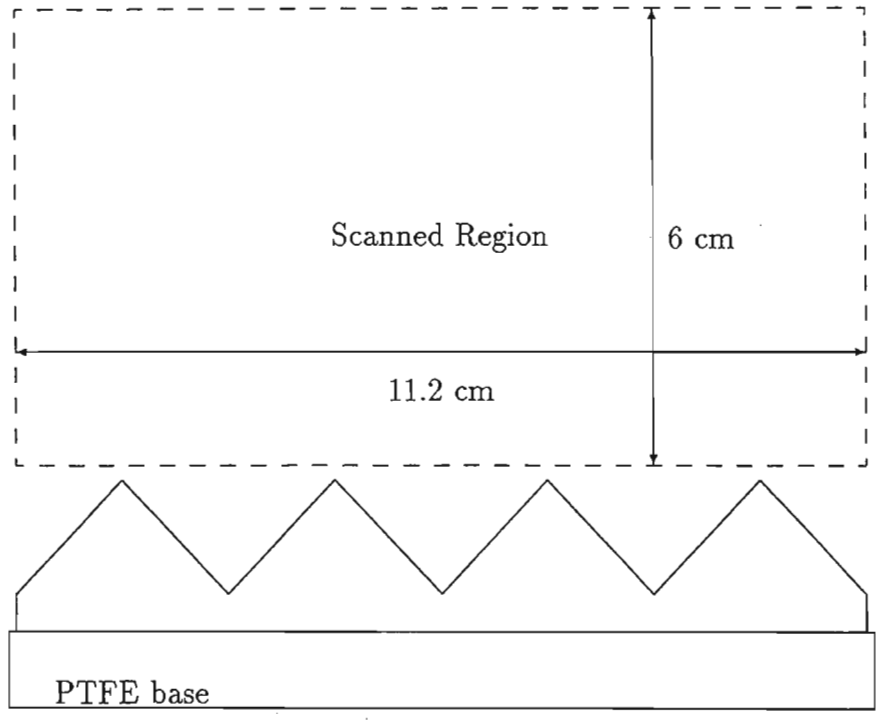

Figure 33: Top view of the complex target also showing the rectangular scanned region, target drawn to scale.

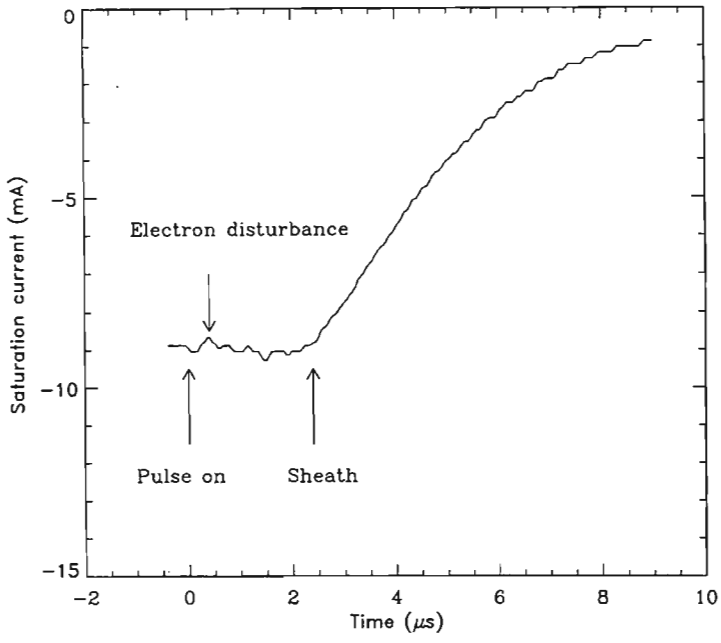

Figure 34: The electron saturation current measured in front of the spherical target.

data was recorded by the HP digital oscilloscope which was triggered by the (negative) rising edge of the voltage pulse. Operating the HP digital oscilloscope in the pre-trigger mode, it was possible to capture the signal before the triggering event. Typically 500 samples were captured per channel over a sampling period of either 10, 50 or 500μs, depending on whether short-time sheath formation, or long-time plasma depletion and replenishment were being investigated. Channel 1 was usually used to record the voltage pulse and channel 2 the corresponding ion or electron saturation current at the probe location.

An example of the electron saturation current measured in front of the spherical target is shown in figure 34.

4.5.1 Data presentation

For two dimensional work, these saturation currents were recorded over rectangular regions with 1mm separations between the grid points in both the x and y directions.

In this way, for each rectangular region, a 3-dimensional array (x, y, t) was stored.

In the sections below, sample figures showing the different methods of data presentation are given. These figures are given only to show the presentation methods, and where appropriate, will be discussed in full elsewhere in the thesis.

A snap-shot of the two-dimensional spatial structure of the saturation current is produced by plotting a two-dimensional slice of the data array, where $(x, y, t = t')$. This may then be visualised as a

1. two-dimensional false-colour image,
2. three-dimensional shaded surface,
3. three-dimensional wire-frame, or
4. contour-plot.

The false colour and shaded presentations were not used in this thesis because they require special printers. They were however, displayed on the PC VGA screen and were used extensively during the initial qualitative analysis to quickly view the data and assist in the choice of values used to produce the contour plots described below.

Like the three-dimensional surface plot, the three-dimensional wireframe plot given in figure 35 presents the data in what is possibly the most intuitive form. One disadvantage of this representation is that even if the viewing angle and elevation are chosen with care, some background features may be obscured by structures in the foreground. Secondly it is difficult to make quantitative measurements from these 3-dimensional representations.

The two-dimensional false colour presentation presents another intuitive image, useful for initial qualitative analysis, where the careful choice of the colour mapping can highlight subtle features due to small variations in the data. For example, the

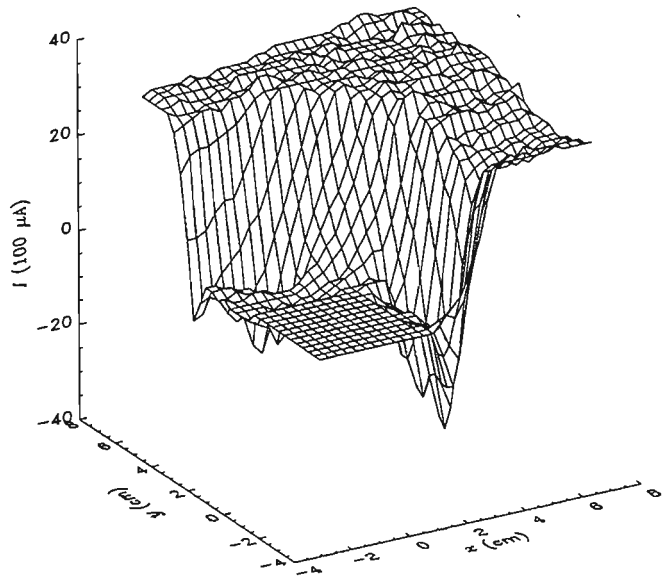

Figure 35: Figure showing the two-dimensional saturation current as produced by IDL's **SURFACE** 3-D wireframe surface output procedure. It shows the ion saturation current around the rectangular target at $t = 6\mu$s, the x and y axes are in cm, and z-axis is in μA.

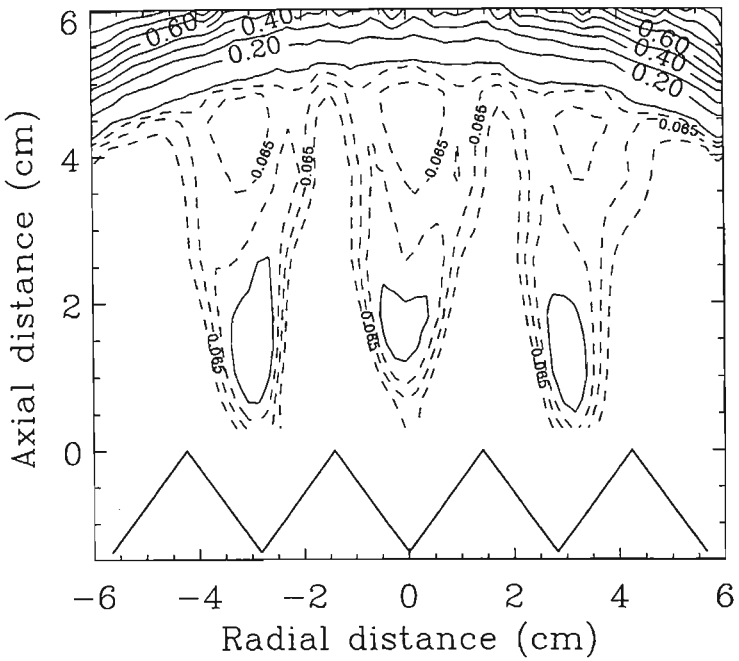

Figure 36: Figure showing the two-dimensional saturation current, using IDL's **CONTOUR** 2-D contour output procedure

small differences in the electron saturation current in front of the saw-tooth target can be seen clearly during the analysis using IDL. Different colours and colour gradients assisted in the differentiating between 'hills' and 'valleys', a difficult task when viewing contour plots. It is only the practical consideration of the capabilities of the printer used which prevents most of the two-dimensional data from being represented in this form.

Contour plots are the most common figure display technique used in this report. Careful choice of contour values and labels allow for reasonably accurate value extraction and with careful analysis of contour trends and values, a good understanding of the data presented can be achieved.

The temporal evolution of sheath behaviour can be seen either by viewing a sequence of 2-dimensional plots drawn in pseudo-colour or as contour plots. IDL provides a programming technique whereby movie clips (comprising 20 or more frames)

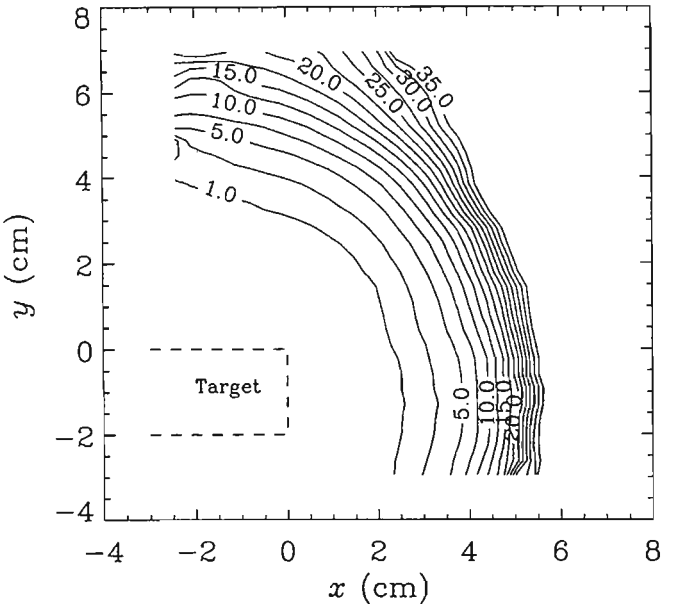

Figure 37: Contour plot showing sheath evolution for the rectangular target, contour values are in μs.

of these plots can easily be generated. Viewing the subsequent 'movie' gives the ability to control the display of the frames with VCR-like controls (frame step forward, backward, etc) to determine the speed and direction of replay. It was found that by repetitively replaying these sequences (perhaps 10 or 20 times) subtle features of the sheath's behaviour could be identified.

By producing contour plots, where the value at each spatial position is representative of the time at which the desired event occurs, temporal evolution can be resolved. For example, by using this method to record when the saturation current drops to 60% of its steady-state value, a contour plot representative of sheath expansion can be produced, as in figure 37. In this figure, the contour values are in μs and show how long it took for the saturation current at that spatial position to drop to 60% of its initial value.

Chapter 5

PIC Simulation

5.1 Introduction

The Plasma Device simulation code, PDP1 (planar) and PDS1 (spherical), are based on the PIC, or particle-in-cell, simulation technique.

In the late 1950's and early 1960's, the idea of using computers to simulate particle movement in plasmas occurred to several people, notably John Dawson at Princeton, and Oscar Bruneman at Cambridge. In the 1950's electron beams in vacuum tubes where simulated. Here, for example, electrons were treated as disks as wide as the beam, with 16 or 32 electrons per wavelength. Their interactions with microwave resonant cavities over 5 or 10 wavelengths, for 10 to 20 cycles, were used to examine the device from linear modulation through to nonlinear saturation. By extending the work to plasmas, the definitive simulation length becomes the Debye length (λ_D), the distance travelled by a particle at the thermal velocity in $1/2\pi$ of a plasma cycle.

Since plasmas, by definition, have interaction lengths much greater than the Debye length, plasma models and simulations do not have to use every one of the 10^6 - 10^{22} particles per cm^{-3} to reproduce the essence of the plasma. Instead, plasmas can be simulated using far fewer finite-sized super-particles to accurately reflect the *collective* behaviour of the plasma. Evaluated at discrete positions on a quantised spatial grid,

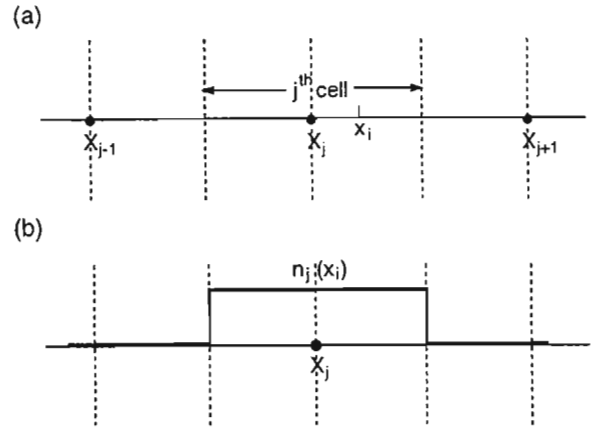

Figure 38: Nearest Grid Point: (a) Particles in the j^{th} cell are assigned to X_j to obtain (b) a grid density of $n(X_j)$ [3]

at discrete time intervals, these super-particles can be defined in terms of the particles contained in Debye cubes.

Particle motion is typically determined by finding all the forces from the effective charge and current densities at the grid points. These forces are then used in turn to calculate the resultant motion of the plasma particles.

Sub-grid sized positions can either be rounded to the nearest grid position, or, as in Particle-in-Cell, affect all neighbouring grid positions with a weight dependant on their relative distances from those grid positions. Figure 38 shows a one-dimensional grid spacing and the effective shape of particles restricted to grid positions. Figure 39 shows the same features but for the PIC method.

5.2 Results

Data obtained from a simulation using the 1-D Birdsall particle-in-cell plasma simulation code (PDS1) has been used to produce saturation current traces and profiles of particle density, velocity and plasma potential. The original simulation code (PDP1,

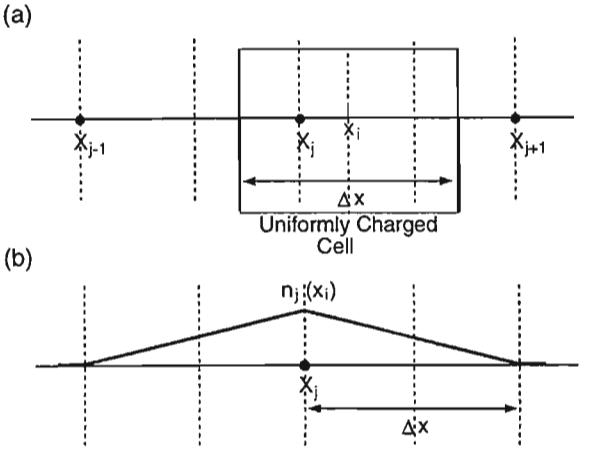

Figure 39: Particle-in-Cell: Particles in the j^{th} cell (a) are weighted over X_j and X_{j+1} to obtain (b) a grid density of $n(X_j)$ [3]

PDS1) did not calculate ion or electron saturation currents. Since saturation currents are used in this thesis as a diagnostic tool, Mark Harmer[1] modified the PDS1 code to produce ion and electron saturation current data. The potential, density, velocity and saturation current data produced in the simulation runs were then interpreted in this thesis.

By using the simulation it is possible to demonstrate the relationship between the saturation currents and the plasma potential in the plasma sheath, as shown in section 5.2.2.

The simulation simulates a PSII pulse where the target achieves a peak potential of -5kV with a rise time of 1μs and a plasma density of 10^8cm^{-3}. The gas used in the simulation was argon, and probe biases of -36V and $+36$V were used to measure the ion and electron saturation currents respectively. These results were chosen to match the experiment.

[1]Former Research Assistant at UND, presently at University of Auckland, Auckland, New Zealand

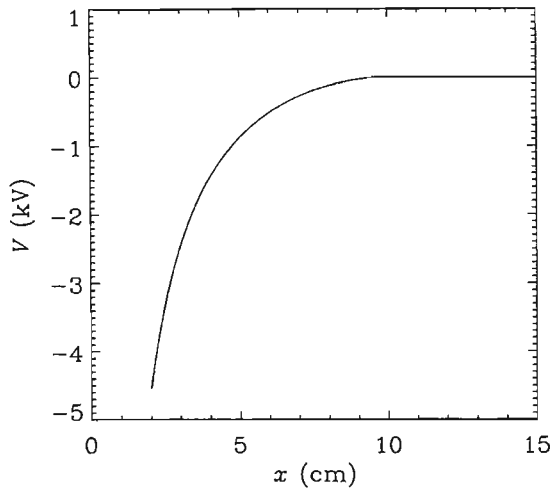

Figure 40: Plasma space potential ϕ_p(V) as a function of position obtained from the PIC code.

5.2.1 Plasma Behaviour

Since it is very difficult to examine the individual ion and electron behaviour in an experimental plasma, a plasma particle simulation has been used to give the particle motion directly. In particular, the velocity and density distributions of each particle species, which may be altered under the influence of the high voltage target bias, is presented. The following sections present the plasma state 10μs, or approximately 5 ion plasma periods, after the pulse was initiated.

Plasma Space Potential

The plasma potential is presented in figure 40, and shows the potential near the target (x = 2cm) to be −4.5kV.

Particle densities

Ion and electron densities in figures 41 and 42 respectively show the relatively

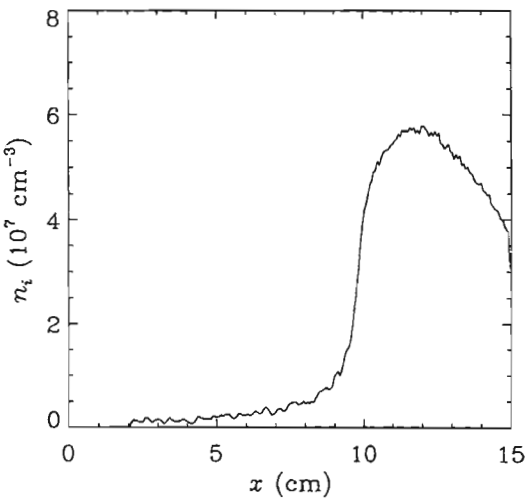

Figure 41: Ion density as a function of position

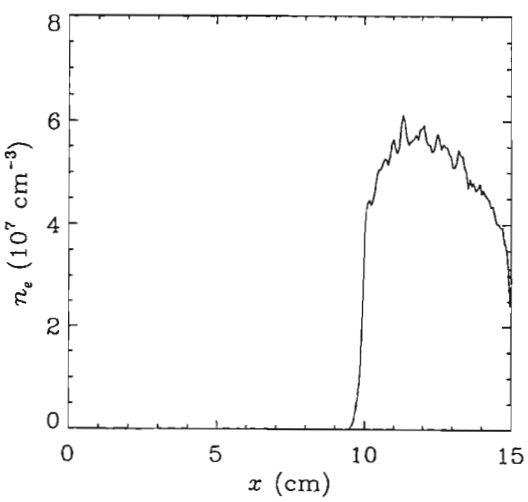

Figure 42: Electron density as a function of position

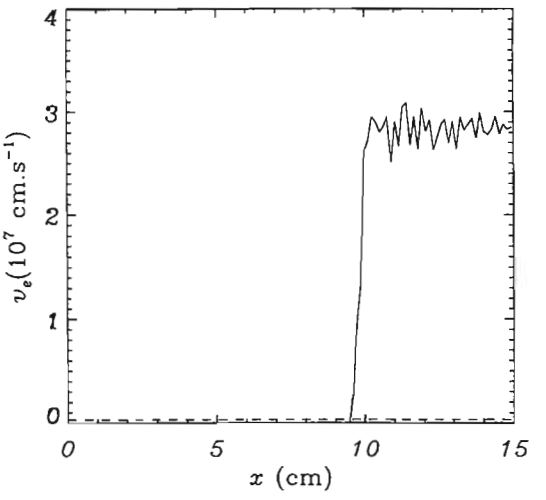

Figure 44: Bin-averaged electron velocity magnitude as a function of position. The average velocity is shown as a dashed line.

than the ions, due to the lighter electron mass. Examinations of the electron velocity phase space revealed that the electrons tended to 'slosh' back and forth in an electron cloud between the chamber wall and the sheath. The slightly positive average velocity, drawn in as a dashed line, shows that while there are large fluctuations in the electron velocities, they have a low drift velocity directed away from the target.

To explicitly show the particle velocity distribution, figures 45 and 46 are produced by plotting a dot for each particle at its corresponding velocity and position. The resultant scatter plot gives an indication of the one dimensional particle distribution function, $f(x, v)$. From these figures it can be seen how the electrons have a large spread of velocities, distributed around zero, while the ions show a small spread for $x > 10$cm, with a cold beam of accelerated ions directed toward the target for $x < 10$cm.

The velocity distribution function at specific positions is produced by analysing the velocities of each particle species in a small spatial region. The velocities of the ions and electrons in the region $x = 9.8 \pm 1.5$cm (sheath at ~ 9.5cm) are shown in figures 47

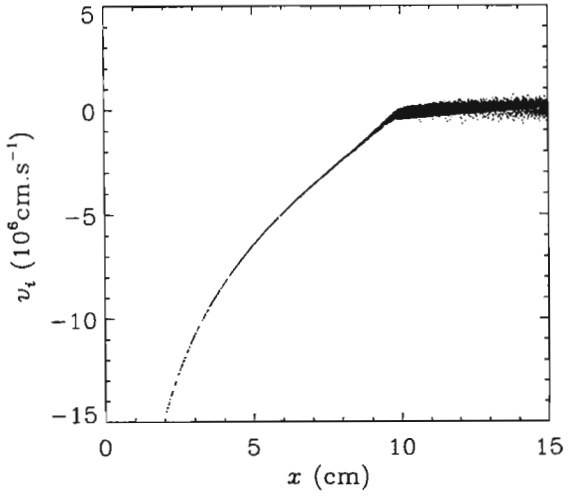

Figure 45: Scatter plot showing ion velocity and position, (sheath at $\sim$ 9.5cm).

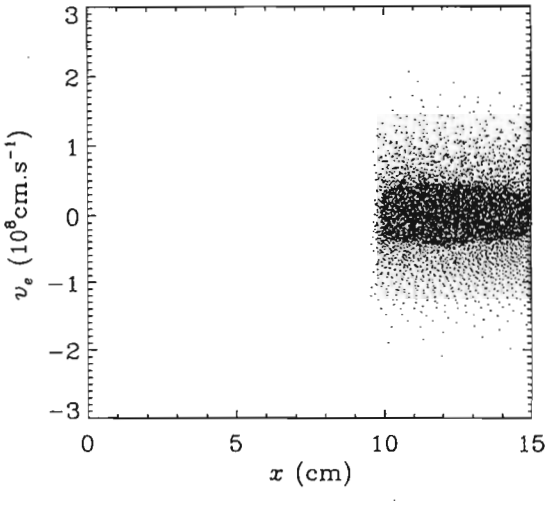

Figure 46: Scatter plot showing electron velocity and position, (sheath at $\sim$ 9.5cm).

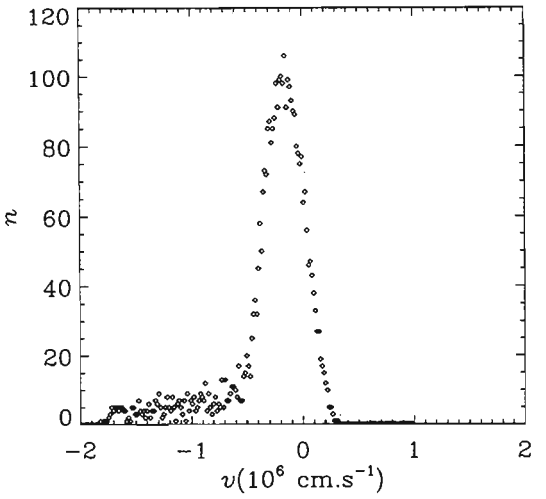

Figure 47: Ion velocity distribution in the region $x = 9.8 \pm 1.5$cm. The tail in the distribution is caused by the ions being accelerated toward the target, since the sheath edge is around $x \approx 9.5$cm.

and 48, and show the electrons having symmetric spread, centred about $v = 0\text{cm.s}^{-1}$, with most particles having a velocity with magnitude less than $1 \times 10^8\text{cm.s}^{-1}$. The symmetric electron tail is indicative of an oscillatory behaviour.

Figure 47 shows that most of the ions have a velocity in the narrow range of $v = -0.2 \pm 0.5 \times 10^6\text{cm.s}^{-1}$, but with a clearly visible tail of ions being accelerated toward the target.

Further away from the target, at $x = 12.0 \pm 1.5$cm, the electrons as shown in figure 50 have a similar distribution to that nearer the target. The deviation from a Maxwellian velocity distribution near $v = 0.0\text{cm.s}^{-1}$ is apparent, however, the half-height width of $v = 8 \times 10^7\text{cm.s}^{-1}$ compares favourably with the electron thermal velocity of $5.93 \times 10^7\text{cm.s}^{-1}$ (see appendix A). The half-height width of the ion velocity distribution, shown in figure 49 to be $3 \times 10^5\text{cm.s}^{-1}$, also compares favourably with the ion thermal velocity of $2.19 \times 10^5\text{cm.s}^{-1}$ used in the PDS1 input deck used for these experiments (appendix A). While this thermal velocity is about a factor

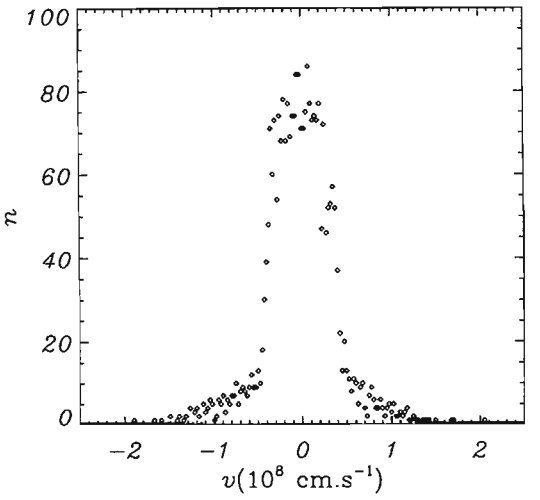

Figure 48: Electron velocity distribution in the region $x = 9.8 \pm 1.5$cm

10 greater than is appropriate for this experiment, it is not clear that this would materially affect the conclusions regarding sheath behaviour. There is also no strong evidence of the region being affected by the target potential, as expected from the zero plasma potential in this region.

Thus it can be seen that close to the target ions are accelerated toward the target, while further away they are relatively undisturbed. This is in agreement with current PSII plasma models, where the ions are accelerated toward the target only when they are uncovered by the expanding sheath. The unexposed plasma ions have only random thermal motion.

5.2.2 Simulation Saturation Currents

It was next necessary to examine whether the sheath position could be inferred from the electron saturation current. This investigation could easily be carried out in the simulation since both the plasma potential and the particle velocity distributions are known. By integrating the velocity distribution, an effective saturation current signal

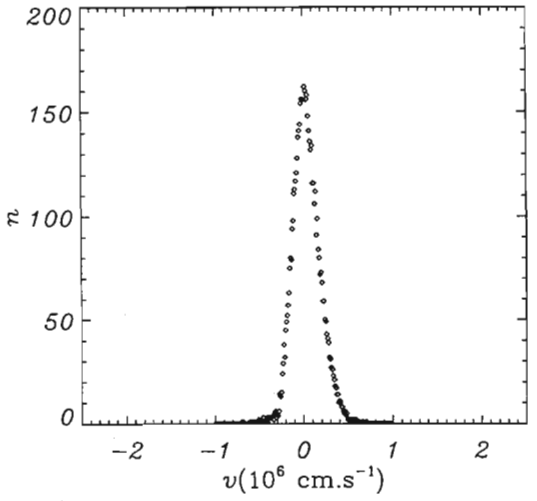

Figure 49: Ion velocity distribution in the region $x = 12 \pm 1.5$cm

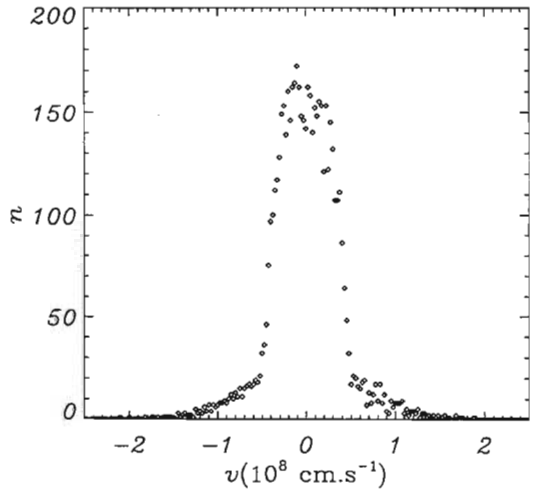

Figure 50: Electron velocity distribution in the region $x = 12.0 \pm 1.5$cm

could be computed.

Ion and electron saturation currents were calculated by evaluating the discrete equivalent of the following current integral, using $v_{min,j}^2 = 2q_j(V - V_s)/m_j$,

$$\begin{aligned} J_{SAT}(V) &= \textstyle\sum_j q_j \int_{-\infty}^{\infty} f_j(v)(v^2 - v_{min,j}^2)^{\frac{1}{2}} dv \qquad \text{for } v_{min,j}^2 \leq 0 \\ J_{SAT}(V) &= \textstyle\sum_j q_j \int_{v_{min,j}}^{\infty} f_j(v)(v^2 - v_{min,j}^2)^{\frac{1}{2}} dv \\ &+ \textstyle\sum_j q_j \int_{-\infty}^{-v_{min,j}} f_j(v)(v^2 - v_{min,j}^2)^{\frac{1}{2}} dv \quad \text{for } v_{min,j}^2 > 0. \end{aligned} \tag{29}$$

where V the probe bias, V_s the plasma potential, q_j and m_j the charge and mass of the j^{th} particle species and f_j the distribution of the j^{th} species. The sums are usually calculated over all particle species, but it may be beneficial to calculate currents due to only one of the species.

Thus the experimental electron saturation current traces measured in the experiments performed with the spherical target, presented in section 6.2, can be simulated and reproduced here.

Figures 51 and 53 show the electron and ion saturation current traces respectively, at positions close to the target, while figures 52 and 54 show multiple electron and ion saturation current traces measured at increasing distances from the target.

Figure 51 shows a negative current measured for approximately 1μs, which then decreases suddenly to zero, when the sheath passes this position. By superimposing the currents measured at increasing distances from the target, figure 52 shows the increasing time taken for the sheath edge to reach that position. The reduced temporal current gradient further from the target is characteristic of the weaker electric field that exists there.

Figure 53 shows a positive current also being measured for the first 1.75μs, after which a sudden decrease to zero occurs. Since this decrease occurs much faster than the ion plasma period of 2μs, there will still be ions in this region. Examining the plasma density information 1μs after the pulse was initiated (that is, when the pulse reaches maximum potential) shows the ion density to be reduced, but not zero.

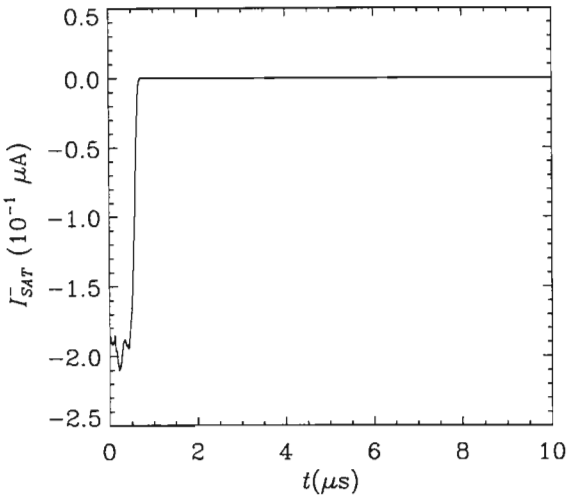

Figure 51: Electron saturation current at $x = 4.5$cm, obtained from the PIC simulation

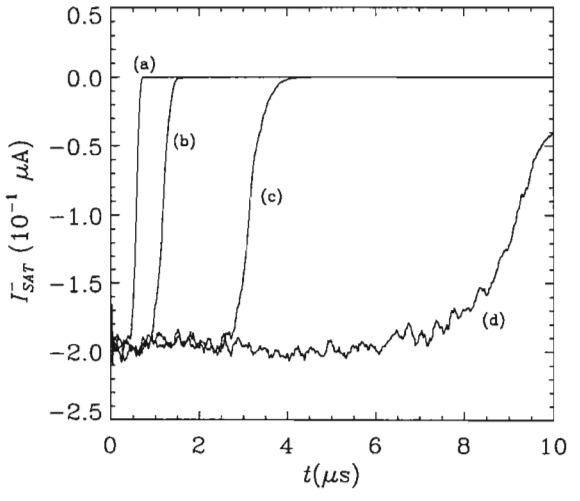

Figure 52: Superposition of electron saturation currents. Traces (a), (b), (c) and (d) show currents recorded at $x = 6, 7, 8.5$ and 10 cm

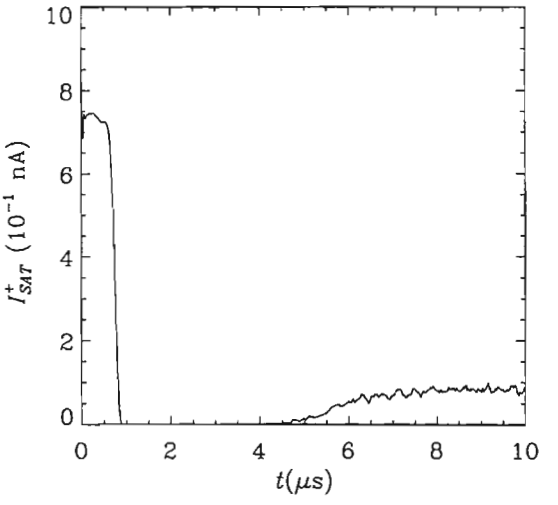

Figure 53: Ion saturation current at $x = 6$cm

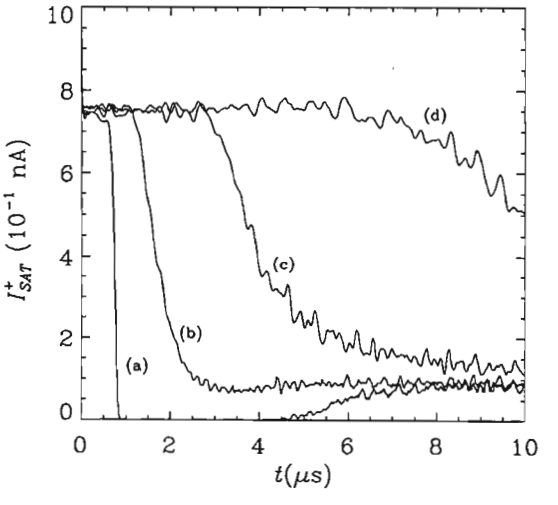

Figure 54: Superposition of ion saturation currents. Traces (a), (b), (c) and (d) show currents recorded at $x = 6, 7, 8.5$ and 10 cm

Specifically, looking at density distributions after 1μs, ion density is low (around $1.1 \times 10^6 \text{cm}^{-3}$ at $x = 2$cm, $1.1 \times 10^7 \text{cm}^{-3}$ at $x = 4.5$cm, where it increases linearly to a maximum of $1.0 \times 10^8 \text{cm}^{-3}$ at $x = 13.5$cm). Electron density is zero at $x = 2$cm, and about $1.9 \times 10^7 \text{cm}^{-3}$ at $x = 6$cm. Thus ion depletion has taken place.

Sheath Identification

Any object immersed in a plasma that is held at any potential other than the plasma space potential, is surrounded by a sheath. This sheath is characterised by the plasma surrounding the object having a different potential to the space potential. Caused by differences in the charge densities around the object as one of the charge species is depleted with respect to the other, this potential profile is a *smooth* function, varying from the object potential at the object, to the plasma potential at the sheath edge. According to the Bohm Sheath Criterion (see section 2.2.1), the sheath edge could be defined as that region where the object potential has dropped to $\sim \frac{kT_e}{2e}$, which is about 1V in the plasmas discussed here. But when the object potential is as high as several, or tens of kV, this definition is not useful as it is very difficult to detect exactly where these potentials have decreased to 1V, and some other relation has to be found to represent the sheath edge.

By plotting the plasma potential over the entire simulation region at selected times and then overlaying the electron saturation currents measured over the same regions, it is possible to see if any relationship exists between the plasma potential and the saturation currents. Figure 55 shows the plasma potential at 1 and 10μs, graphed with dash-dot and dashed lines respectively. By overlaying electron saturation current traces at 0, 1, 3, 5, 7 and 10μs, one can then attempt to relate the saturation currents to the potential, and identify some feature of the potential to define as the sheath edge.

Features of interest in the figure are:

1. the sharp boundary where the saturation current drops to zero,

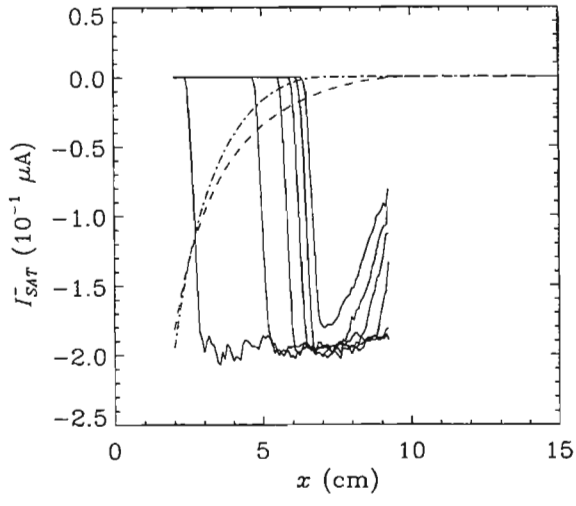

Figure 55: Overlaying electron saturation currents at 0, 1, 3, 5, 7 and 10μs with the plasma potential at 1μs (dash-dot line) and 10μs (dash-dash line).

2. the smooth, continuous form of the potentials, and
3. the apparent electron depletion near the chamber wall (from $x > 9$cm).

The assumption that the transition in the electron saturation current can be used to identify the sheath edge and its subsequent evolution implies that it is necessary to define some criterion to specify the sheath edge in the smoothly varying potential profile as well as in the electron saturation current trace.

By choosing the criterion to define the sheath edge as being that point at which the potential has decreased to 10%, it is instructive to calculate the velocity of this reference point. From figure 55 it is seen that this point in the potential profile propagates from 4.8 to 6.5cm in 9μs, i.e. has a velocity of about 2×10^5cm.s^{-1}, or $5c_s$, which compares favourably with the sheath velocity at 6.5cm, as shown in figure 57.

This definition of the location of the sheath coincides with the sudden transition in the electron saturation current. In practice, a similar criterion needs to be applied to the experimental current trace. This could fairly arbitrarily be defined as being

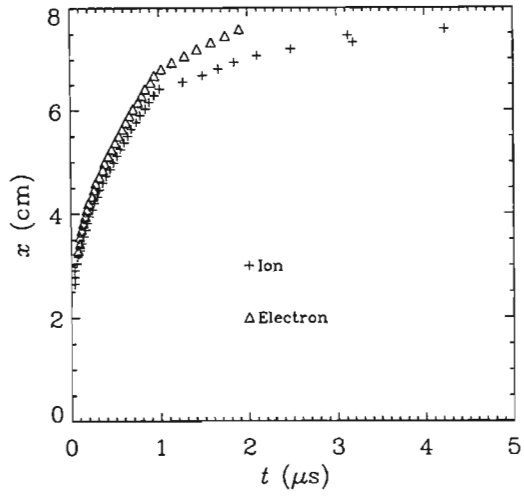

Figure 56: Sheath position as determined from the saturation currents in the numeric simulation. The y-axis shows sheath edge distance from the target centre.

the point at which the electron current dropped by, for example, 10% of its maximum value. In the analysis of the experimental data, saturation current values of 60%, 85%, and 90% of the current maximum were used, depending on current signal conditions.

Sheath Evolution

Using the criterion that the sheath position is determined by the point at which the saturation current decreases to about 90%, figure 56 shows the resultant sheath position as a function of time. It should be noted how the ion saturation current decrease lags behind the electron saturation current.

Figure 57 shows sheath velocity as the sheath expands. Expressed in units of c_s, the ion acoustic velocity, this figure shows how the sheath is initially travelling at about $70c_s$, followed by a gradual decrease in velocity. The velocity is about $5c_s$ at $x = 6.5$cm, in agreement with the value determined on page 83, determined from the examination of sheath position at two known times.

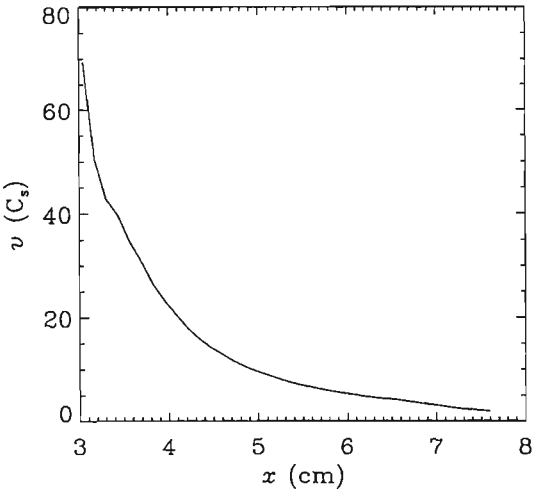

Figure 57: Sheath velocity calculated from the electron saturation current in the numeric simulation. The y-axis shows sheath velocity as a function of distance from the target centre.

5.3 Summary

The simulation has been used to reveal more detail about ion and electron behaviour during the PSII process. More importantly, the simulation has been used to verify a correlation between the electron saturation current decrease and the sheath position.

Chapter 6

Experimental Results and Discussion

This section presents the data of the experiments performed, and is divided into three sections, each describing the results obtained with the spherical, rectangular and complex targets.

Some discussion is included in each section, but concluding statements are left for the next chapter.

6.1 Experiment Results

The results presented below are representative of experimental work performed in the Plasma Processing Laboratory of the Department of Physics, University of Natal, Durban, from February 1994, to March 1995.

The results presented describe the ion and electron saturation current measurements and can be applied to the analysis of sheath behaviour during the PSII process.

Sheath evolution is determined by measuring the ion and electron saturation currents at intervals along the line and then determining when the sheath edge passes each point. The sheath edge is defined to have reached a particular point when the

electron saturation current has decreased to a certain percentage of its background value, typically 90%.

By using the HP digital oscilloscope triggered to capture both input channels upon detection of the negative going edge of the high-voltage pulse, a record of

1. either the target voltage or total current on channel 1 and,
2. either the ion or electron saturation currents on channel 2

can be captured.

Clearly, since the probe needs to be biased negatively and positively to measure ion and electron saturation currents respectively, these data must be measured separately.

Thus comparisons between ion and electron saturation currents must be made with the awareness that the two currents were measured simultaneously only in the sense that they share the same triggering event.

6.2 The Spherical Target

This target was used to produce saturation current traces that can most sensibly be compared with the simulation. Since the PIC simulation was used to validate the assumption that electron saturation currents can be used to track sheath evolution, this section will describe results obtained using this diagnostic technique. Additionally, ion and electron saturation currents will be used to compare experimental sheath evolution with well documented theoretical and other experimental results.

6.2.1 Saturation Currents

By incrementally moving the probe along the axis of the chamber and sampling the saturation current, it is possible to measure sheath evolution as it propagates axially into the chamber.

6.2.2 Ion Saturation Currents

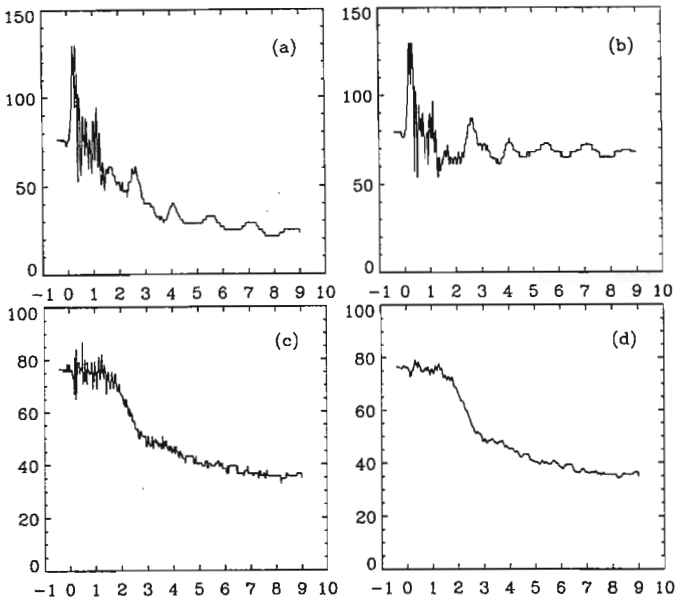

Figure 58: Processing the ion saturation current. Panels (a), (c) and (d) recorded 2.5cm from the target, (b) recorded at 3.85cm is the background signal. (c) shows (b) subtracted from (a). x-axis in μs, y-axis in mA.

Before sheath evolution was investigated the saturation currents were examined individually. From this initial examination it was noticed that the quality of the ion saturation current signal was contaminated by the presence of an extremely large amplitude noise signal. The noise is visible in figure 58(a) and (b) (recorded 2.5 and 3.85cm from the target, respectively) as a damped simple harmonic signal having two frequency components. The first being the frequency of the damped signal itself ($\sim$0.7 MHz), and the second being a high frequency signal (>10 MHz) very clearly visible in the first 2μs.

This noise signal appeared to remain unchanged over the entire scanned region. Since there appeared to be no detectable phase shift it was probably caused by electromagnetic pickup generated by the power-supply. Figure 58(b) shows this noise recorded at the furthest point from the target. This was used to define the background signal. Thus the ion saturation current could be cleaned by background subtraction (figure 58(c)). Additionally, by smoothing using a moving 5 point box-car average, a

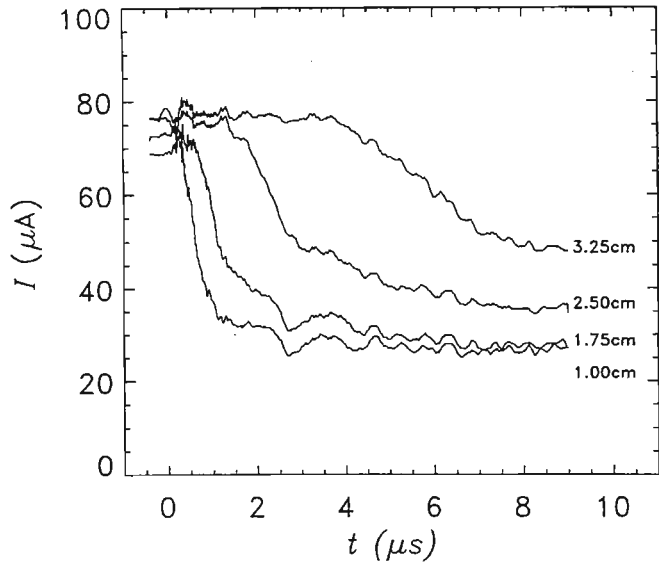

Figure 59: Spherical target ion saturation current evolution. Currents recorded 1.00, 1.75, 2.50 and 3.25cm from the target surface respectively.

much clearer plot could be extracted, as shown in panel (d).

Figure 59 shows the ion saturation currents processed with background subtraction and smoothing at various distances from the target. The five plots show the ion saturation currents measured 1.00, 1.75, 2.50, 3.25 and 4.00cm from the target surface respectively.

Points of interest in these figures are the initial current decrease followed by a levelling out of the trace. In the first plot ($x = 1.0$cm) of figure 59, the decrease occurs at $t \simeq 0.3\mu$s, and the levelling out at $t \simeq 1.1\mu$s. On the third plot ($x = 2.5$cm), these points occur at about 1.6 and 2.6μs, respectively. The significance of these two events will be discussed later in section 6.2.4.

6.2.3 Electron Saturation Currents

Since the electron saturation current is about 100 times greater than the ion saturation current, it is far less sensitive to noise caused by noise pickup and small plasma

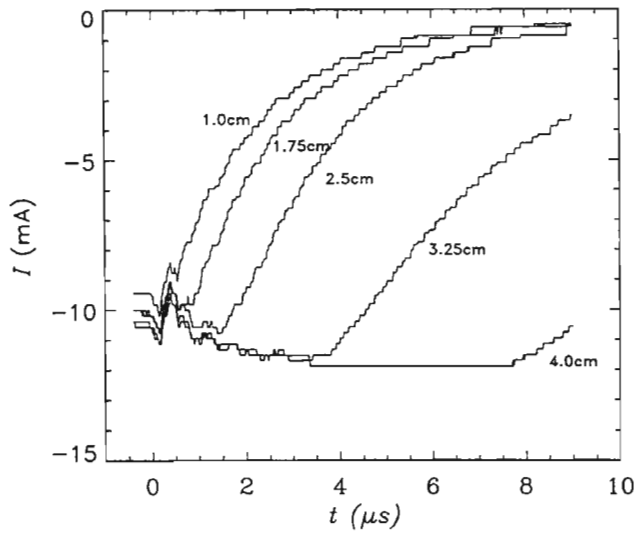

Figure 60: Spherical target electron saturation currents evolution. Currents measured 1.0, 1.75, 2.5, 3.25 and 4.0cm from the target surface.

fluctuations, and no additional pre-processing was necessary before analysis. The electron saturation current traces are drawn in figure 60. The four plots show the current measured (from top to bottom) 1.00, 1.75, 2.50, 3.25 and 4.0cm from the target surface respectively. It is seen that the time taken for the current to decrease to zero increases with distance.

An interesting feature is the *increased* (negative) currents measured in the plots at $x = 3.25$cm between 1 and 9 μs, and at $x = 4.0$cm between 1 and 4μs *after* the pulse was applied. This can be explained in terms of an increased average electron energy and density at this position as the electrons which are accelerated away from the target travel through this region, resulting in an increased current measured according to equation 4. The reduced currents measured close to the target at $t = -0.5\mu$s are due to the effect of the plasma sheath which ordinarily surrounds the (effectively grounded) target before the voltage pulse at time $t = -1\mu$s. This sheath reduces the undisturbed plasma density near the target, but the reduced sheath effect 4cm from the target can not by itself account for the large currents measured there at around

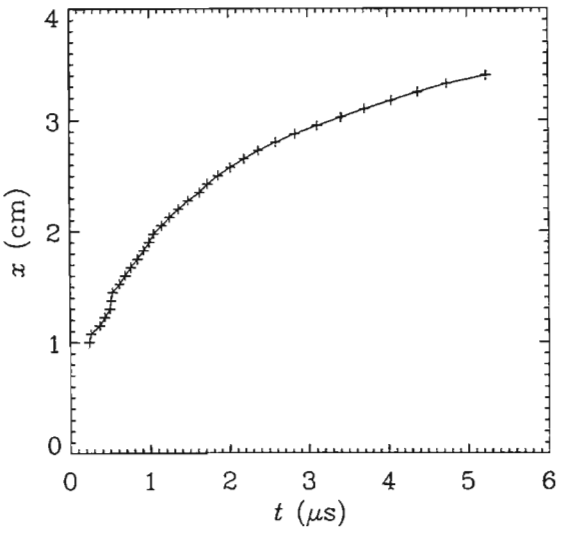

Figure 61: Spherical target sheath evolution. The y-axis shows sheath distance from the target surface

$t = 6\mu$s.

Since the sheath front will be defined to occur at that position where the electron density has decreased to some percentage of its initial value (section 5.2.2), it is sufficient to use only the electron saturation currents to detect sheath passage, though it will be shown later how the ion saturation currents can be used to extract more information about plasma behaviour behind the sheath front.

6.2.4 Sheath evolution

Figure 61 shows the sheath position as a function of time assuming an electron saturation current threshold value of 90%.

In its early stages, the sheath velocity is about $10^2 c_s$, as reported by Thomas and Alport [51].

Comparing this velocity with the numeric simulation equivalent, figure 57, we see that in the early stages the simulation sheath has a velocity of $70c_s$ which compares

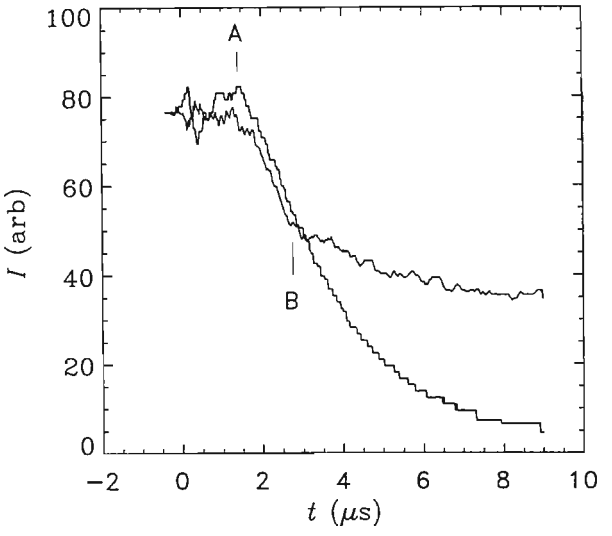

Figure 62: Superposition of ion and electron saturation currents. The ion current is the top trace at $8\mu s$.

favourably with the experiment.

With suitable scaling and inverting it is possible to superimpose the ion and electron saturation currents, as has been done in figure 62. This figure, measured at $x = 2.5$cm, shows a number of characteristic features common to most of the saturation current traces measured using the spherical target. Firstly, both the ion and electron currents begin to decrease simultaneously ("A"), and the rate of decrease is initially approximately the same. However a separation occurs at the second point ("B"). This point can be seen in the numeric simulation, on the third trace of fig. 54((c), at $x = 8.5$cm), at $t \simeq 4.5\mu s$. This is possibly a result of the target-bound ions uncovered by the sheath front (which has already passed this point) being collected by the probe and hence sustaining the positive ion current.

By plotting the evolution of this second point ("B") in figure 63 as the probe is moved away from the target, it is seen that this event lags the sheath (drawn as a dashed line). A similar behaviour was also noted in figure 56 when discussing the

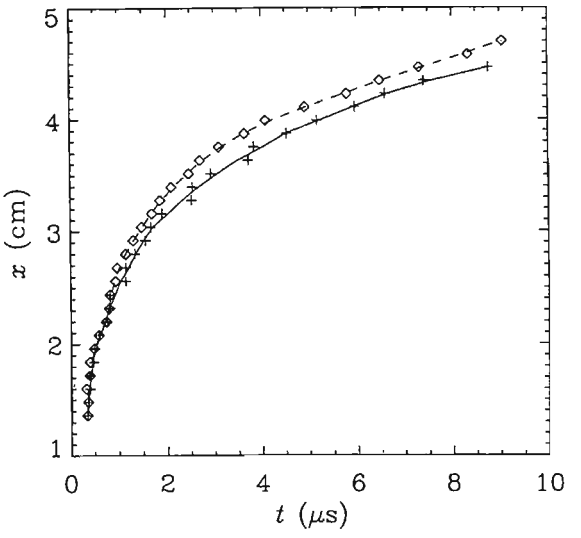

Figure 63: Superposition of ion and electron sheath events

results of the numerical simulation.

Plotting this delay as a function of position in figure 64, we see that it increases as the sheath propagates along the axis.

6.2.5 Summary

The results from this target have been succesfully compared with the numeric simulation to verify the validity of using experimental electron saturation currents to classify sheath position and evolution.

6.3 The Rectangular Target

Machined out of stainless steel into a rectangular block, $8 \times 2 \times 2$cm, the rectangular target was used to investigate sheath evolution around a corner. Theoretical investigations of sheath evolution around corners have indicated that they would experience non-uniform implantation profiles.

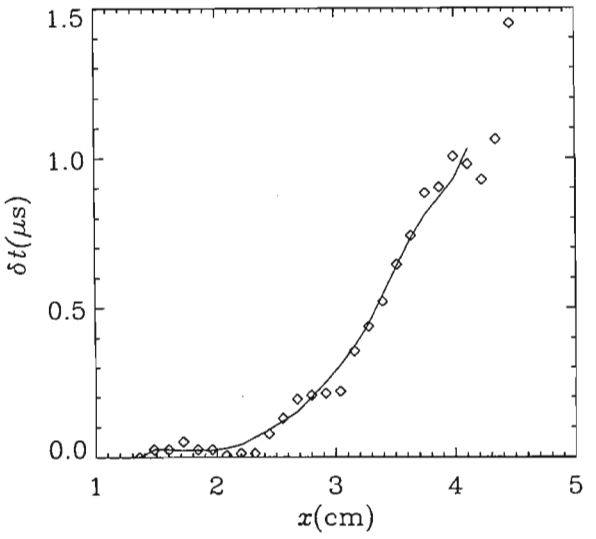

Figure 64: Delay by which the ion sheath event lags the electron sheath event.

6.3.1 Scanning Strategy

The objective to investigate sheath evolution around a rectangular corner required that this target be scanned in two dimensions. The strategy employed involved scanning the target in two adjacent rectangular regions, as shown in figure 31, with both regions starting 7cm away from the target in the x-direction, and scanning toward the target with the same x-increment, so that the two regions could be matched. The data described below use a co-ordinate system where the top corner of the corner is located at $(x, y) = (0, 0)$. The target axis occurs along $(x = x\prime, y = -1)$.

Since the probe motion is controlled by two stepper motors, it was convenient to classify probe motion in terms of these two directions. Thus axial motion was along the chamber axis x, and measured in cm, while radial motion perpendicular to the chamber axis y, was measured in degrees. The spatial distance from the target to the probe in the radial direction can be calculated from the formula for the chord for a sector, as mentioned in section 3.2.3. In these co-ordinates, each region was

scanned by first recording saturation currents at fixed intervals axially along a line, returning the probe to its starting position, then moving it radially, before repeating the axial scan. Thus the first region was scanned in 12 lines of 18 positions, where each point was $\sim$ 3.25mm apart, with successive lines just over 1 degree apart. The second region was scanned in 18 lines of 30 positions, with the same separation. The resultant 30 by 30 region was used to produce the figures below, with the missing 12 by 12 region occupied by the target being filled in with suitable default values. These values were chosen by extending the values of the 12 border positions into this blank region and maintaining as smooth a surface as possible.

6.3.2 Electron Saturation Currents

Preliminary examination of the electron saturation currents revealed a spurious pre-pulse dip, associated with a small positive going spike produced by the high-voltage supply. As with the EMI disturbance with the spherical target, this pulse did not change with probe position, and so could be removed by background subtraction. Figure 65 shows the unprocessed signal (a), the background (b), and the signal minus the background, (c). Slight differences in background currents are corrected by the addition of a small offset, calculated from the knowledge that panel (c) is zero at 30μs. The final processed signal is shown in panel (d).

Figure 66 shows the spatial behaviour of the saturation currents. Recorded along the line ($y = -2$cm) at $x = 1.5, 3.4, 6.0$ and 7.0cm, from top to bottom, these plots show the effect of distance on the saturation current responses.

Figures 67 and 68 show the electron saturation currents at (1.5, -1.0) and (7.0, -1.0), with the currents recorded at (-1.1, 1.1) and (-1.1, 7.0) drawn as dashed lines. From figure 67 it is seen that 1cm from the target the saturation currents have the same basic shape and decrease toward zero simultaneously in the axial and radial directions. At a distance of 7 cm from the target, figure 68 shows that the sheath travels faster in the radial direction, reaching this point 17μs earlier than in the axial

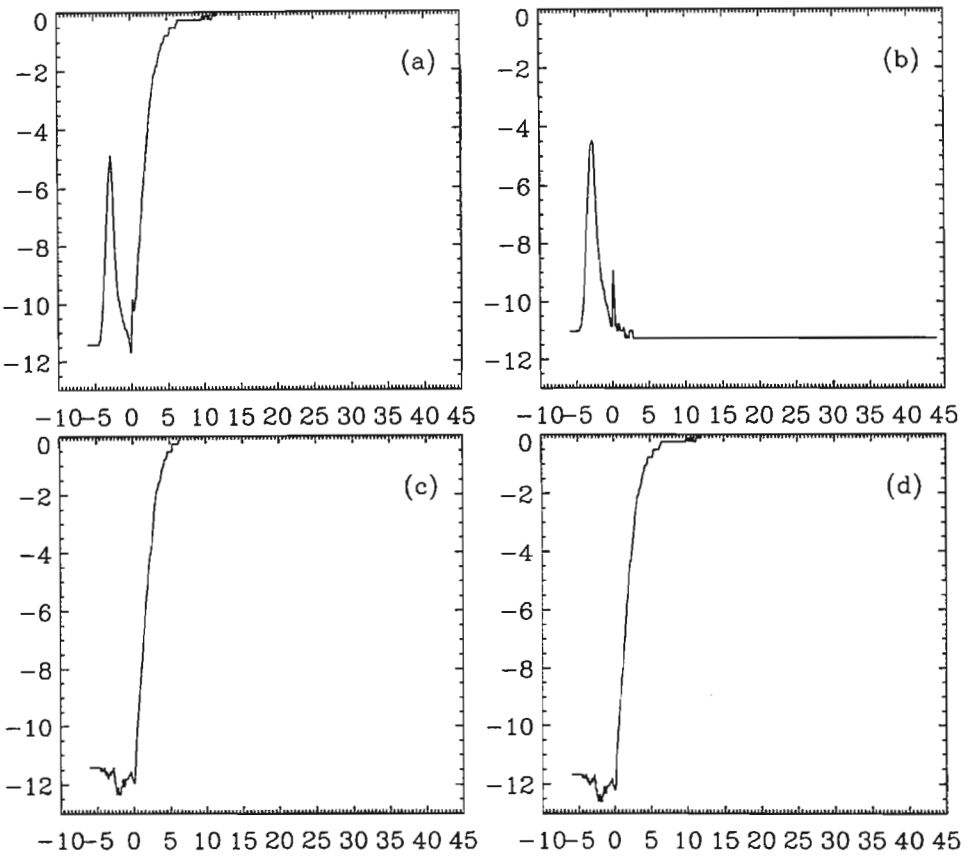

Figure 65: Processing the electron saturation current signal. Panel (c) is produced by subtracting (b) from (a). The x-axis is in μs, y-axis in mA.

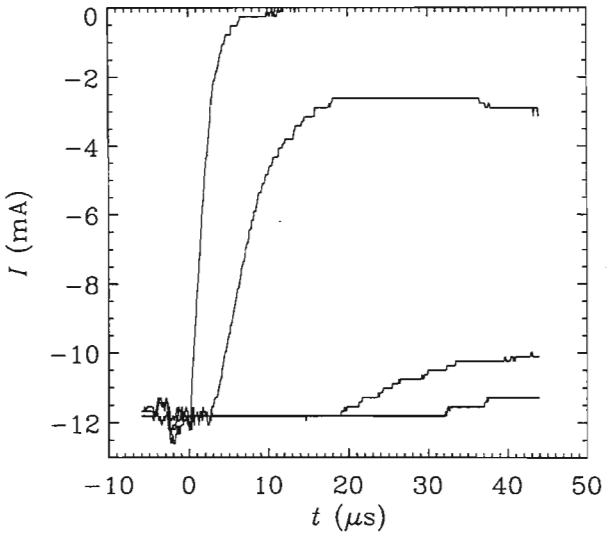

Figure 66: Electron saturation currents measured 1.5, 3.4, 6.0 and 7.0cm from the target in the axial direction, along the line $y = -2$cm.

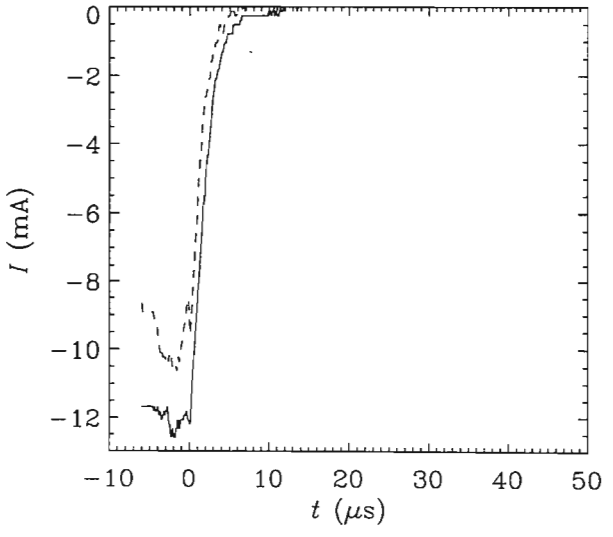

Figure 67: Electron saturation currents measured 1cm from the target in the axial (solid) and radial (dashed) directions.

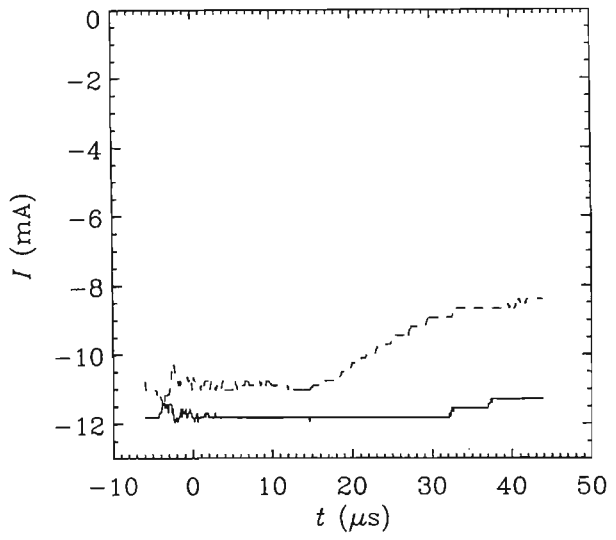

Figure 68: Electron saturation currents measured 7cm from the target in the axial (solid) and radial (dashed) directions.

direction.

This behaviour is also shown in figures 69 and 70. Figure 69 is a contour plot of sheath evolution, where the sheath edge is associated with a 20% decrease in electron current. Each contour shows the time taken for the sheath to reach that spatial position. The widely spaced contours in the radial (y) direction are indicative of a high velocity, when compared with the axial (x) direction.

Profiles of sheath position *vs* time at $x = -1$cm and $y = -1$cm are drawn in figure 70. A greater velocity in the radial direction is apparent.

Plasma recovery

By reducing the oscilloscope timebase to 500μs per sample, plasma recovery around the target can be examined. The saturation currents recorded along the lines $y = -1$cm, at $x = 1, 4$ and 7cm are shown in the left column of figure 71, while the currents recorded along the line $x = -1$cm, at $y = 1, 4$ and 7cm are shown in

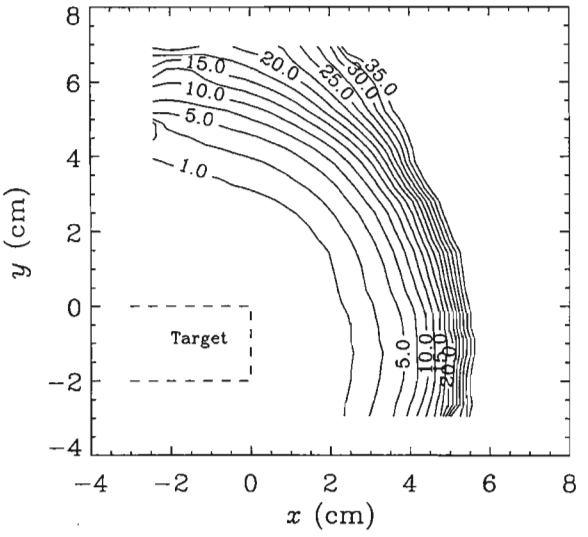

Figure 69: Contours showing sheath evolution around the rectangular target. Contour labels are in μs.

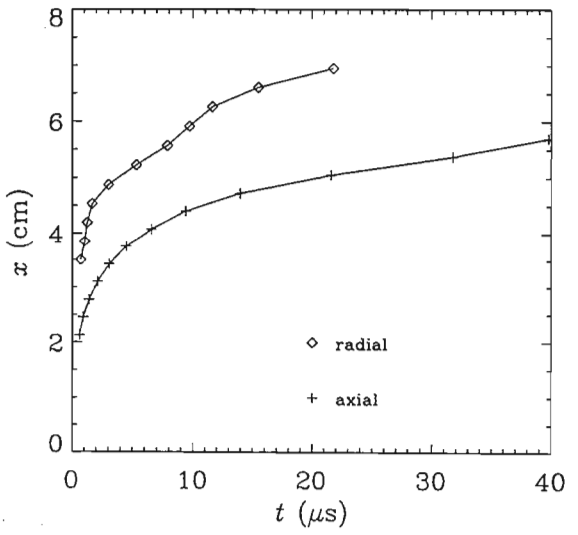

Figure 70: Sheath evolution, measured 1cm from the corners of the rectangular target.

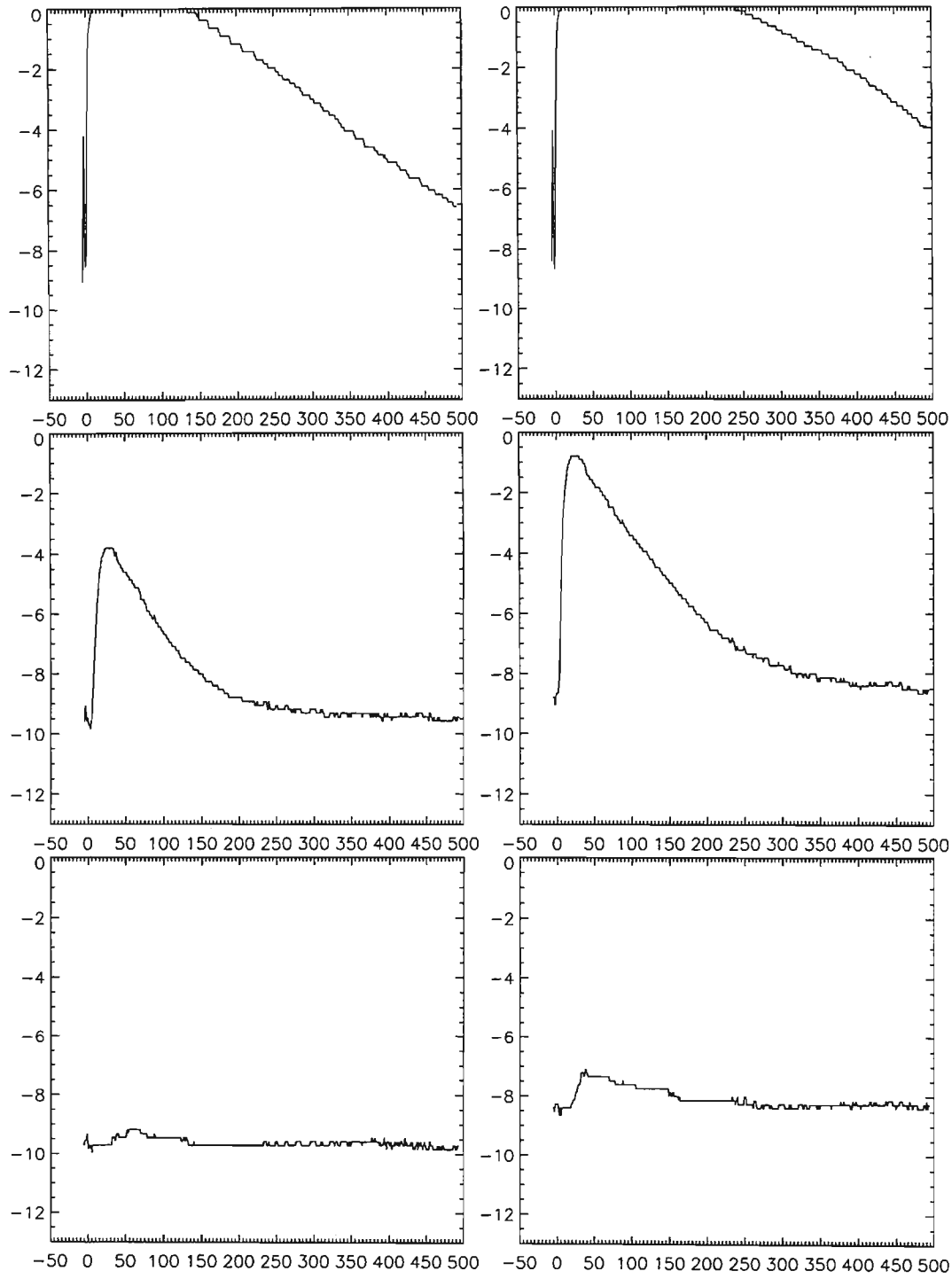

Figure 71: Long-time electron saturation current measurements, showing plasma recovery. x-axis in μs, y-axis in mA.

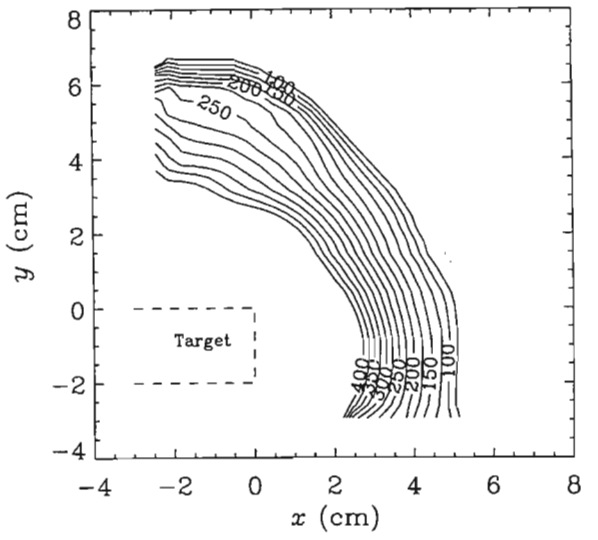

Figure 72: Contour plot showing plasma recovery. Contours are in μs, showing time taken for the saturation current to return to 80% of maximum.

the right column. This figure shows the full effect of the PSII pulse on the electron saturation current traces.

Figure 72 is a contour plot showing the time taken for the saturation current to return to about 80% of its steady-state value. Again the velocity in the radial direction appears much greater than in the axial direction. The velocity in each of these two directions is shown plotted in figure 73.

6.3.3 Ion saturation currents

By biasing the probe negative, an ion current is measured, and by biasing the probe with a sufficiently large negative bias, typically -36V, the ion saturation current is measured (c.f. section 2.2.1). Ideally, this measured ion current should be positive, however, if the plasma electrons are given enough energy (by the high-voltage pulse, for example) they can overcome the potential barrier of the probe and, if enough electrons do so, they can swamp the ion signal and produce a net negative current.

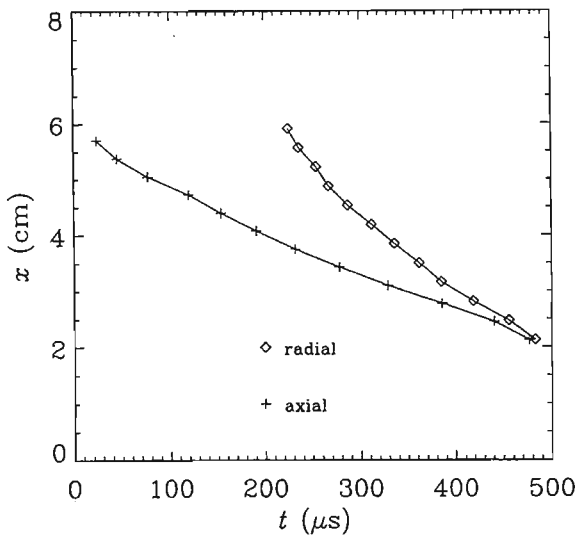

Figure 73: Plasma recovery. The two lines show the distance of the plasma sheath edge from the target in the axial and radial directions.

This phenomenon is clearly visible in ion saturation currents measured near the target, where electrons ejected from the target are accelerated by its high potential, and is discussed again on page 126.

At this stage it is worth pointing out that there are three electron populations present in the plasma during this time. The first two being the electrons which normally present in a discharge plasma, consisting of the primary ionizing and the background plasma electrons. The third population are the secondary electrons which are ejected from the target by ion bombardment. It is suspected that these secondary electrons, which can be accelerated to high energies by the target potential, are responsible for the swamping of the ion currents to produce a negative net current.

Having subtracted the background noise (discussed below) from the signal, figure 75 shows the ion current measured at the same positions as for figure 71. The top two panels clearly show the negative currents measured close to the target.

Looking at the background signal, shown in figure 74(b), two distinct signals are

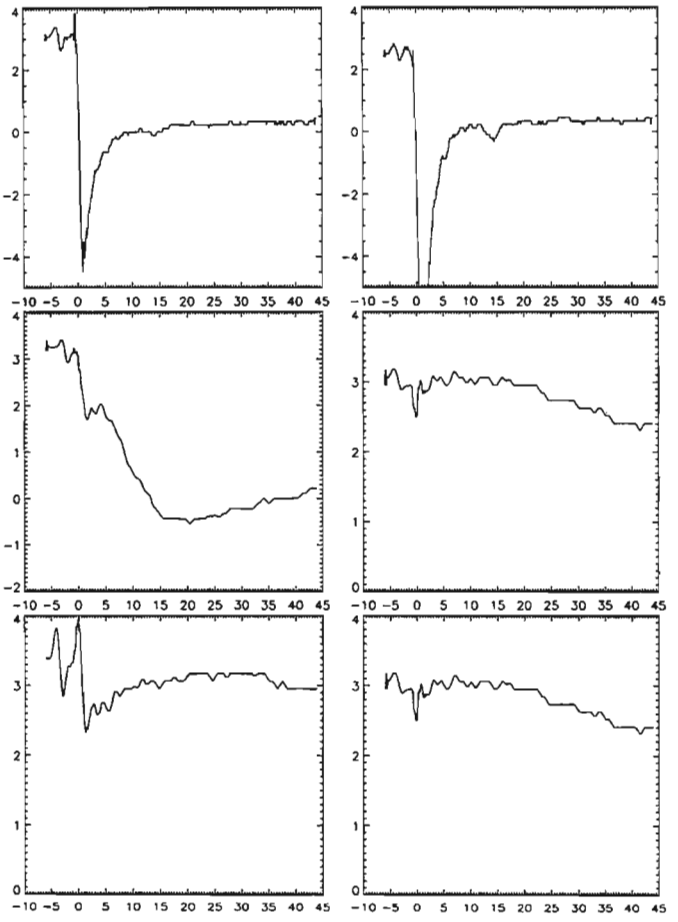

Figure 75: Spatial ion current behaviour. Left (right) panels show the ion currents measured along the lines $y(x) = -1$cm, $x(y) = 1, 4$ and 7cm. The x-axis is in μs, the y-axis in 100μA.

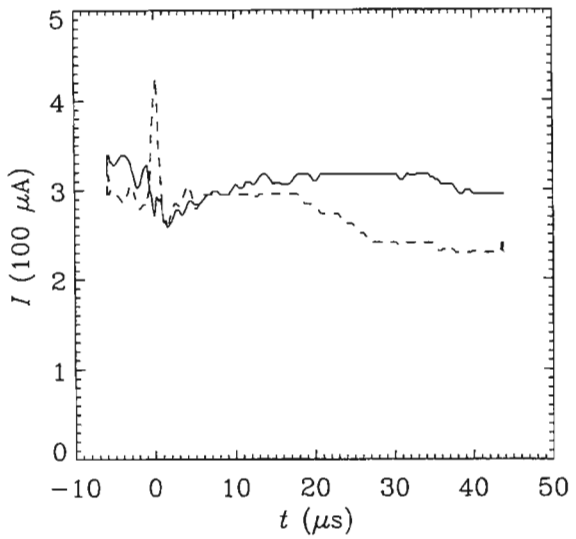

Figure 76: Ion saturation currents measured 7cm from the target in the axial (solid) and radial (dashed) directions.

the ion currents measured at (-1, 7) (7cm from the target in the radial direction), as a dashed line and (7, -1)cm (7cm from the target in the axial direction), as a solid line.

Figure 77 shows the ion saturation current measured at four positions along the $y = -1$ line (corresponding to a line through the middle of the square face). Electron swamping is clearly visible from $1 < t < 9\mu$s at 1.5cm, and for $t > 9\mu$s at 3.4cm. The negative current is produced when the secondary electrons, emitted from the target, are given sufficient energy that they can overcome the -70V potential barrier of the probe bias. Since the electrons are being accelerated away from the target, their contribution to the probe current would increase with distance away from the target as they accelerate through the sheath.

By plotting the two dimensional spatial variation of the ion saturation current at specific times, the influence of these accelerated electrons and the target geometry can be clearly seen. Figure 78 is a contour plot of ion current at $t = 10\mu$s, with

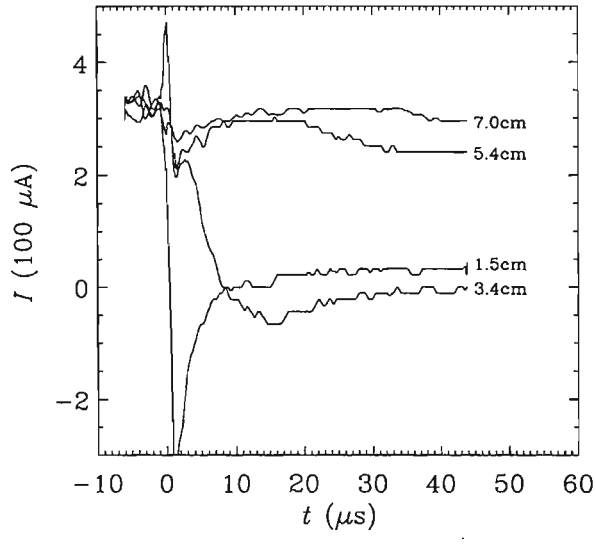

Figure 77: Ion saturation currents measured 1.5, 3.4, 5.4, and 7.0cm from the target in the axial direction.

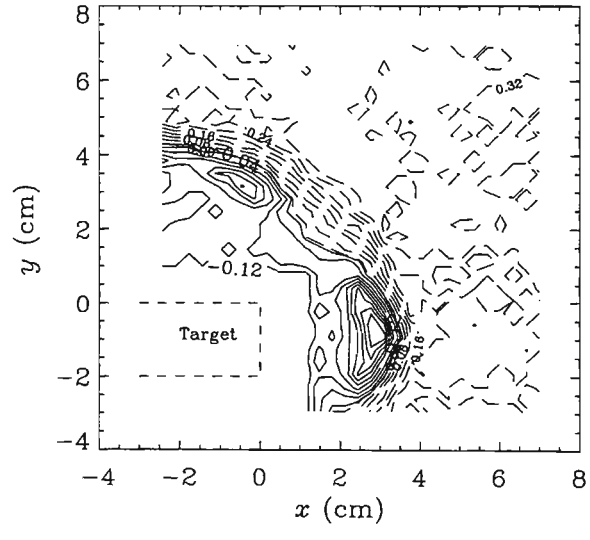

Figure 78: Two dimensional contour plot of the net ion current at $t = 10\mu$s. The contour values are in mA, with solid contours representing negative currents caused by electron swamping.

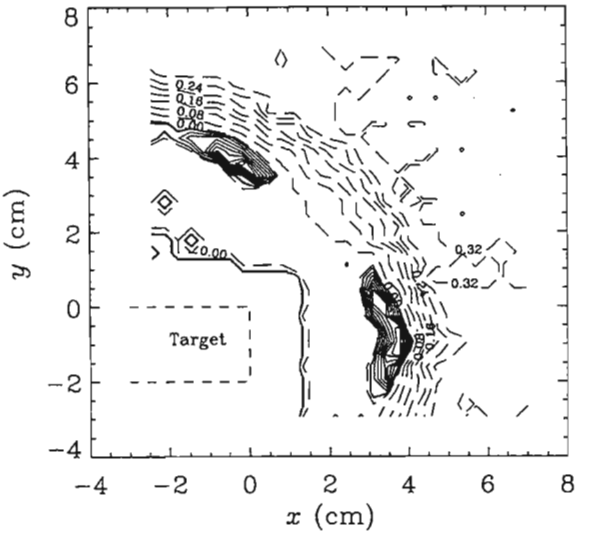

Figure 79: Two dimensional contour plot of ion saturation currents at $t = 20\mu$s. The contour values are in mA, with solid contours representing negative currents caused by electron swamping.

contour values shown in mA. The dashed and solid contours correspond to positive and negative current respectively. Visible as two islands of solid contours, very localised electron swamping is seen to occur about 3cm in front of, and to the side of the target. Since the sheath edge is about 4 – 6cm from the target at this time (figures 69 and 70), these islands are not caused by electrons being accelerated away by the approaching sheath.

Additionally in figure 79, at a later time (20μs) it can be seen how this region of electron swamping, as shown by the closed solid contours at 3.5 – 4cm, moves away from the target as the sheath edge propagates outward.

There are possibly two explanations why electron swamping occurs in the localised regions visible in figures 78, 79 and 80: (1) Out-bound electrons are being focused into these regions by properties of the target geometry and swamping the ion current, or (2) While high energy electrons are capable of inducing negative currents in a

shell around the target, certain regions experience an increased ion flux due to ion channelling. This increased flux may be sufficient to prevent electron swamping in those regions. Further three-dimensional scanning may be more informative, though the use of single-sided probes may be sufficient (section 6.4.4).

In their paper in which Sheridan and Alport [54] propose a two-dimensional model of ion dynamics during PSII. They show how the electric field focuses ions near the corner of a square target. They considered a target which was one ion-matrix sheath width d_{im}wide, leading to an increased ion flux to the target due to ion focusing approximately $0.125d_{im}$ from the corner. In the experiments described in this thesis, $d_{im} \simeq$ 4.3cm, with a target width of either 2 or 8cm, depending on the face examined. In either case, the electron surplus occurs about 0.5cm from the corner, or about $\frac{1}{8}d_{im}$. This is consistent with what one would expect if there were enhanced secondary electron emission from a region experiencing a greater ion dose.

Figure 80 is a multi-panel contour plot illustrating that these electron-rich regions exist for a long time as they propagate away from the target. From figures 69 and 70 it can be seen that the islands are well within the sheath at these times.

6.3.4 Summary

Electron saturation current measurements made around the rectangular target demonstrate the formation and propagation of a sheath during the PSII process. This sheath tends to have a spherical shape, except that sheath propagation is faster (figure 70) in front of the (8 × 2cm) side face than the smaller (2 × 2cm) front face.

Ion saturation current measurements demonstrate susceptibility to electron swamping, in small localised regions 3 – 4cm in front and to the side of the rectangular target.

When using the probe to measure saturation currents in front of the rectangular sides of the target, the plane of the probe surface is no longer parallel to the sheath. Since a sharp transition is still seen in the saturation current traces, it is not clear if this configuration adversely affects the results presented here.

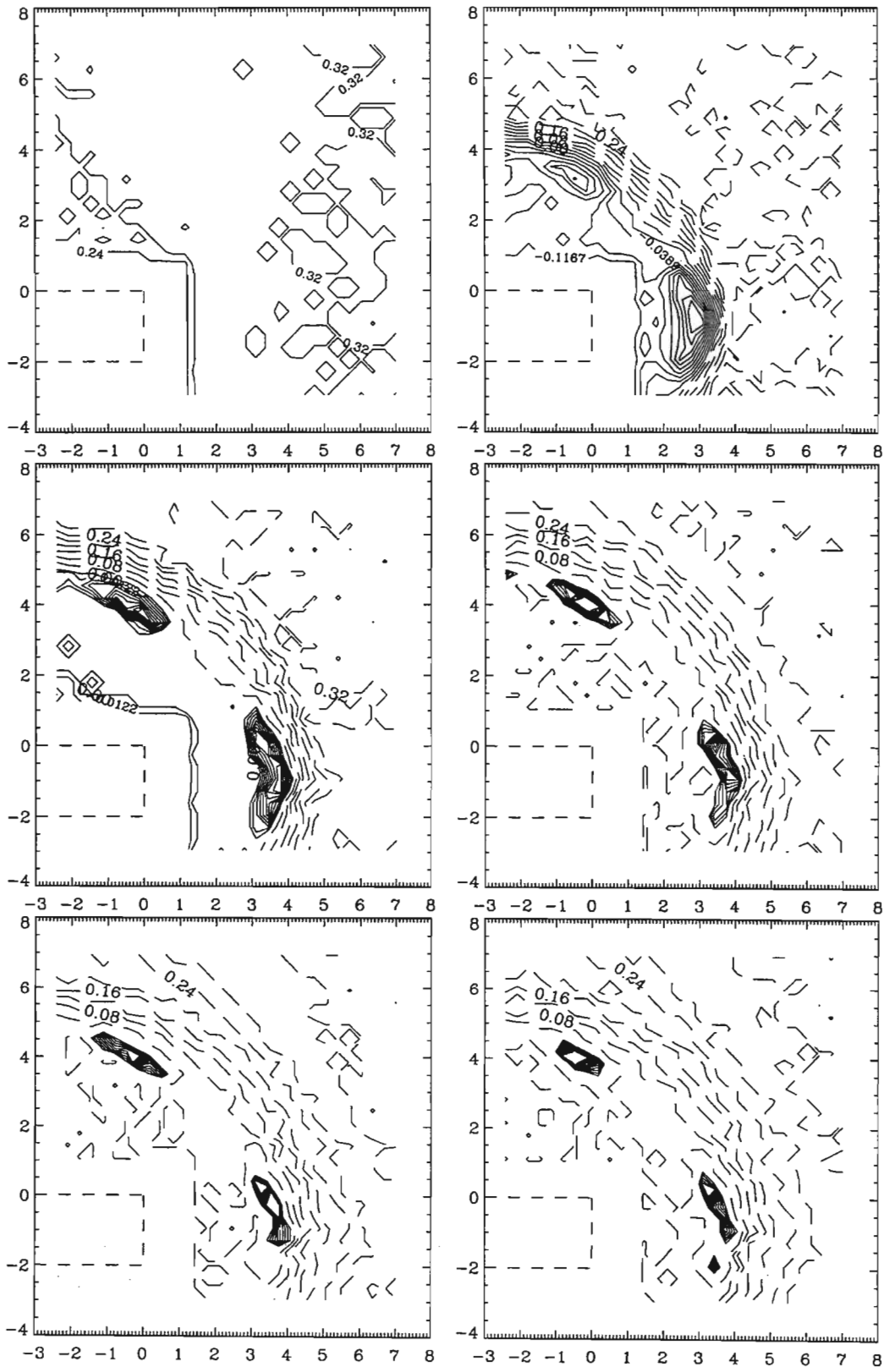

Figure 80: Contour plots of the net ion currents measured at $t = 0, 10, 20, 30, 40$ and 43μs. The x and y axes are in cm and the contour values are in μA.

6.4 The Complex Target

As described before in section 4.4, the complex target has a saw-tooth cross-section. This geometry thus had three concave and four convex regions, comparable to the 90° structures used by Watterson [41] and Donnelly [40]. In their papers they studied ion acoustic wave evolution around concave and convex structures and reported non-symmetric sheath formation. Specifically, they reported observing a thinner sheath around the apex of the wedge, and correspondingly thicker sheaths in front of the concave regions.

Initially the complex target was chosen to investigate the degree of sheath conformality with target geometry. However, the initial qualitative examinations of the measured currents displayed two-dimensional structures. The focus of the investigation shifted to a study of these structures.

This section reports on spatial structures observed in the two-dimensional ion and electron saturation current measurements which have significant implications regarding ion focusing and electron channelling around concave and convex structures. This in turn affects ion dose uniformity, and possibly X-ray production.

6.4.1 Scanning strategy

The sheath evolution around the complex target was analysed by scanning a 12 × 6cm rectangular region in a (curved) plane perpendicular to the plane of the target, centred at the target midpoint. This region was scanned along 64 lines of 16 points. Each line extended axially into the chamber, with each point 3.8 mm apart. The lines were 0.58 degrees apart, or 0.2 mm (in the radial direction). The target and probe configuration are shown in figure 32. The co-ordinates given below give the distances from the centre of the target, with the plane of the apexes at $y = 0$cm.

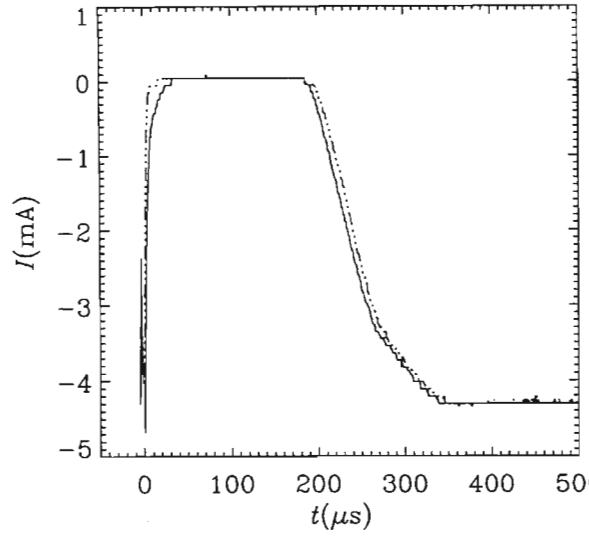

Figure 81: Electron saturation currents recorded in front of the apex (dashed, at $x = 1.3$cm) and concave region (solid, at $x = 2.6$cm) of the complex target

6.4.2 Electron saturation currents

A preliminary investigation of the saturation currents again revealed the spurious pre-pulse disturbance mentioned in section 6.3.2. However, since this disturbance occurs earlier in the recorded traces and does not affect the electron saturation currents in the times of interest, no special processing has been performed to remove it. Also, since the ion saturation current characteristics are used to perform qualitative analysis, no processing was performed on them either.

The electron saturation currents recorded over a 500μs interval, starting 6μs before the high voltage pulse was applied, is given in figure 81. The dashed plot was recorded in front of an apex at $(-1.3, 1.1)$, and the solid plot in front of a concave region at $(-2.6, 1.1)$. From this figure it can be seen how the currents recorded at the concave region take longer to decrease to zero.

Closer examination of the first 80μs, as shown in figure 82, reveals that the current recorded at the apex starts decreasing earlier, as expected from the closer proximity

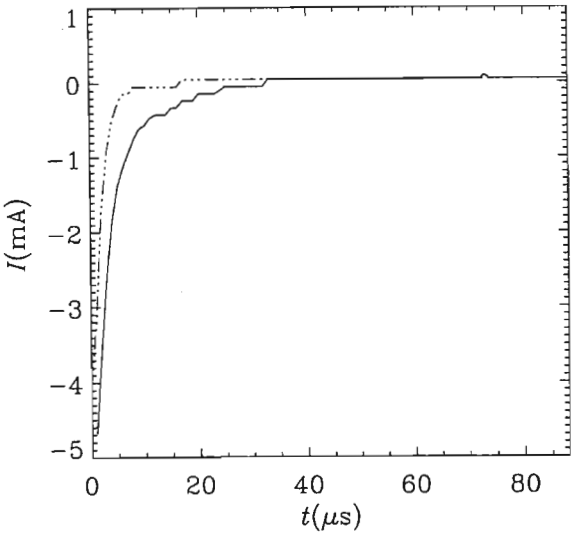

Figure 82: Electron saturation currents recorded in front of the apex (dashed) and concave region (solid) of the complex target, during the first 80μs.

of the probe to the target surface, but that the lifetime of the currents measured at the concave region is much longer than might otherwise be expected. While one might expect a delay before the current decreases to zero as the plasma electrons are repelled from the ion matrix, it should not take as long as 10μs, which corresponds to $\sim 1000\tau_{pe}$, by which time the sheath edge has long passed this position; (visible at $y \approx$ 4cm after 2μs in figure 83). Thus, it appears that even though the probe is between the target and the sheath, it is still collecting a significant electron flux: This is attributed to the secondary electron emission from the target.

Two dimensional contour plots of the electron saturation current recorded over the entire region at selected times clearly show structure associated with target shape. For reference, the target profile is drawn in at the bottom of each figure.

Figure 83 shows the electron saturation current recorded 2μs after the high-voltage pulse was applied. Features to note are the main sheath edge forming a rounded spherical front about 4cm away from the target, a shape which bears little resemblance

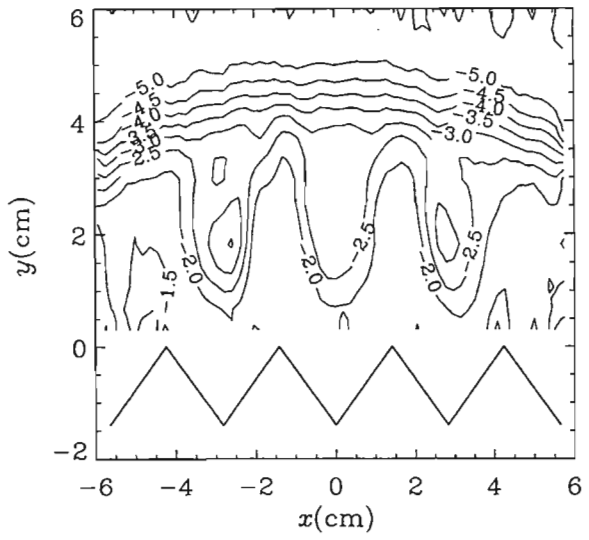

Figure 83: Spatial variation of the electron saturation currents measured at $t = 2\mu$s, contours are in mA.

to the target geometry. Of more interest are the three extended fingers that protrude in front of the concave regions. The closed contours visible in the two regions at $(\pm 2.5, 1.9)$ are -3mA islands. These islands of increased electron flux are possibly caused by the focusing of electrons as they are accelerated away from the target.

Examining the plasma at a slightly later time $t = 5\mu$s, in figure 84, it can be seen how the sheath edge is now 5cm from the target, and still quite clearly spherical.

While reduced in magnitude, the three islands of increased negative current are still clearly visible, and have moved further away from the target.

By plotting several such figures next to each other, the formation and evolution of features is more clearly seen. Figure 85 shows such a sequence of panels plotted at $t = -5, 2, 5, 7, 10$ and 20μs.

Figure 85(a), at $t = -5\mu$s, shows the normal undisturbed saturation current profiles. The reduced magnitudes measured near the target correspond to the expected

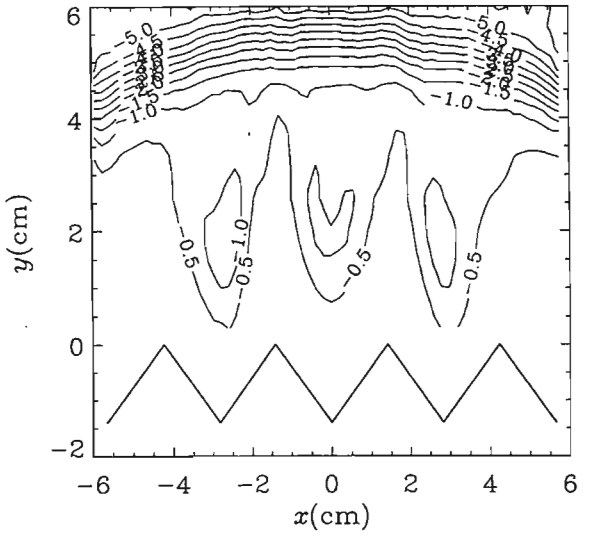

Figure 84: Two dimensional plot of the electron saturation currents measured at $t = 5\mu$s in front of the complex target. The contours are labelled in mA.

reduction in plasma density as one enters the plasma sheath surrounding any conductor.

Panel (b) (2μs) and panel (c) (5μs) show the islands of greater negative current measured in front of the concave regions. As will be shown later in the analysis of the ion saturation currents, these islands are thought to be caused by energetic electrons being ejected, and accelerated away from the target.

Panel (d) (7μs) again shows the localised and transient nature of these higher energy electrons, with their current contribution decreasing again about 3.5cm from the target. Also, for the first time, zero currents are recorded in front of the apexes, where the plasma has been completely depleted of electrons.

Panel (e) (10μs) shows that the extent of the electron depleted region has increased. The main sheath edge has left the top of the scanned region, and is still propagating outward.

Panel (f) (20μs) shows the sheath to have almost completely left the scanned

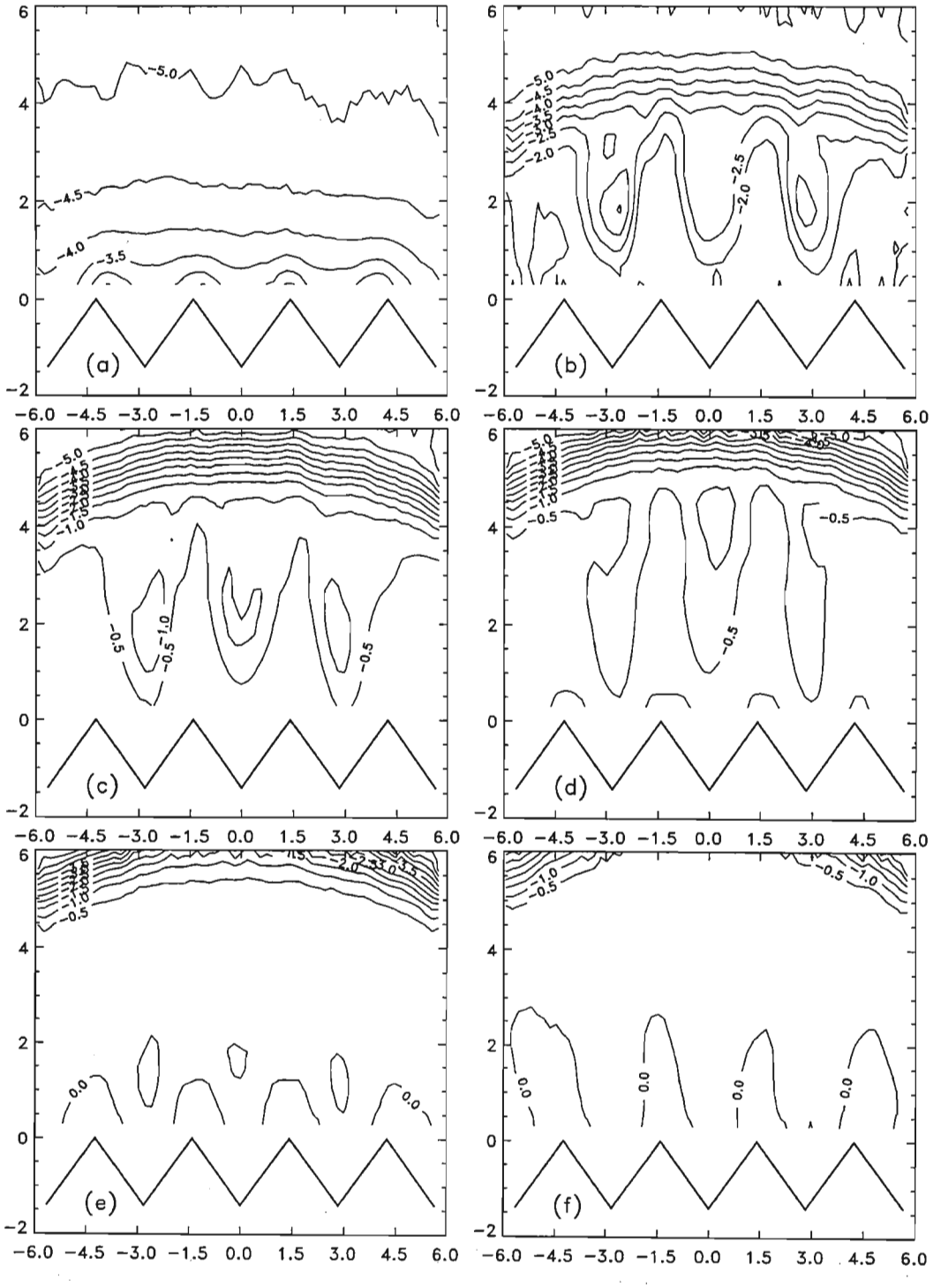

Figure 85: Two dimensional electron saturation currents measured at $t = -5, 2, 5, 7, 10$ and 20μs. Axes are in cm.

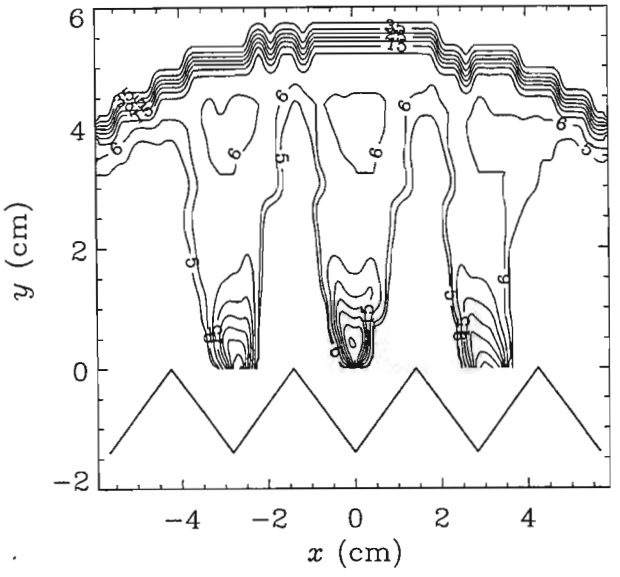

Figure 86: Contour plot showing sheath evolution. Contours are in μs, and show the time taken for the electron current to be depleted to 15% of its background value. The contour values are in multiples of 5μs except for the addition of a 6μs contour.

region. The elongated regions of total electron depletion have also expanded. The fact that these depleted regions do not extend into the regions in front of the concave regions again support the suggestion of the presence of an electron source, either at the target (eg. secondary electrons being ejected by ion bombardment), or in the region in front of the target due to neutral gas ionisation.

Sheath evolution

By associating some electron current value with the sheath edge, in the same manner as sections 6.2.4 and 6.3.2, a two-dimensional picture of sheath evolution can be produced. The contours of figure 86 show the time taken for the electron current at each spatial position to decrease to 15% of its background value. This low value was chosen to highlight the low current structures visible in the previous figures, and their long lifetime. Of more interest are the contours in front of the target concave

regions which show islands that are also long lived.

A similar plot (not included) showing the time taken for the current to decrease to 45% of the background value just shows a single 2μs contour overlaying the 5μs contour of figure 86 with no particularly long lived structure visible.

Thus it seems as though the plasma density is rapidly depleted to a low density in these regions, but thereafter decreases much slower, taking as long as 50μs to be completely depleted. This behaviour was first seen in figures 81 and 82, but now the spatial behaviour of this effect is clearly visible.

Also, the sheath shape only reflects target geometry for the first few microseconds after the application of the potential pulse, after which it has a distinctly rounded shape.

Thus by examining the electron saturation currents, the characteristics of sheath formation and evolution can be investigated, demonstrating the effect target shape has on the plasma behaviour.

Plasma replenishment

Figure 87 shows the various stages of the plasma replenishment. Of interest in these figures is again the rounded shape of the plasma front and the reduced fluxes recorded close to the target as a result of the presence of the target plasma sheath.

6.4.3 Ion saturation currents

Typical ion saturation currents measured in front of an apex and concave region, corresponding to figures 81 and 82, are described below.

Figure 88 shows the ion saturation currents recorded over a 500μs time interval. Once again electron swamping is evident (*c.f.* section 6.3.3), since the negative currents recorded for the first 5 and 25μs can only be as a result of electrons overcoming the -70V potential barrier of the probe bias and being collected by the probe.

The negative part of the trace has been clipped at $\sim -80\mu$A. The actual full

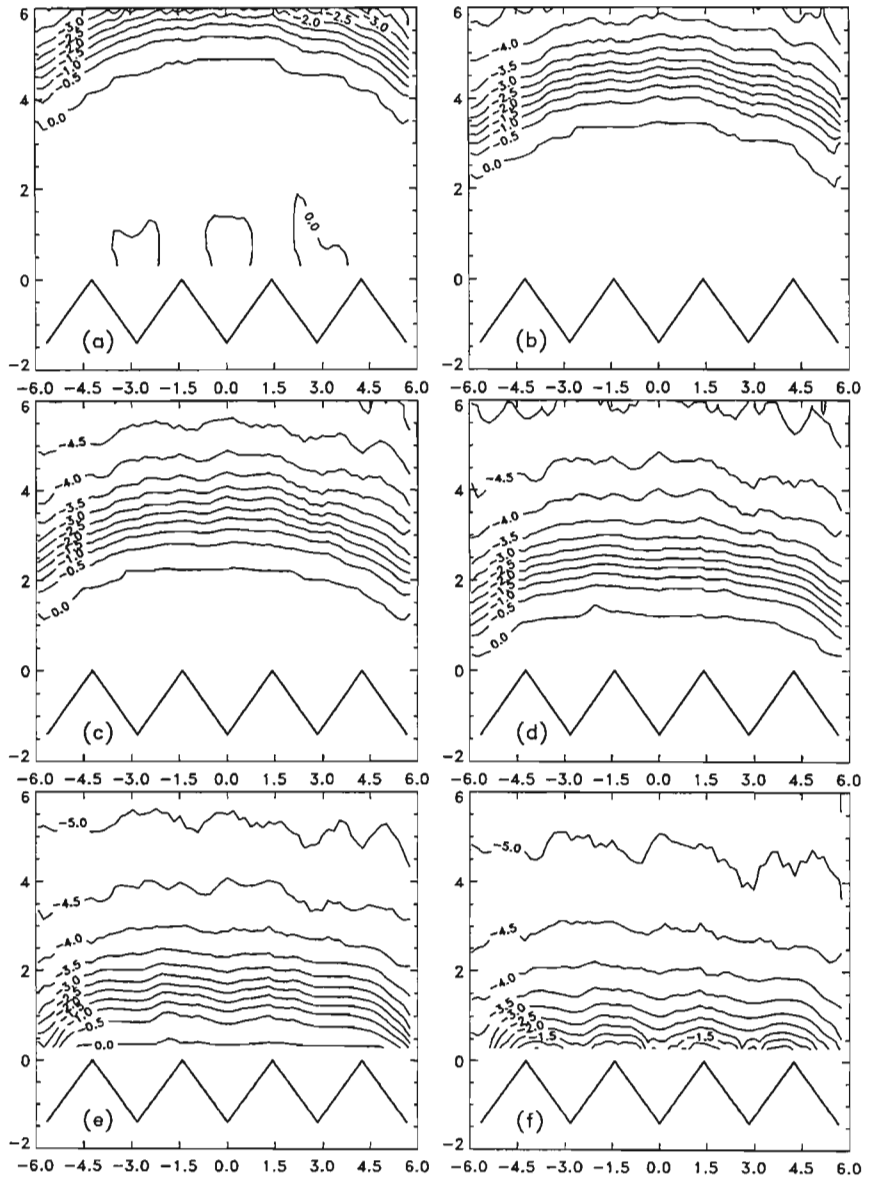

Figure 87: Electron saturation currents measured $50, 100, 150, 200, 250$ and 300μs after the pulse was applied, to show plasma replenishment. Contours are in mA, axes in cm.

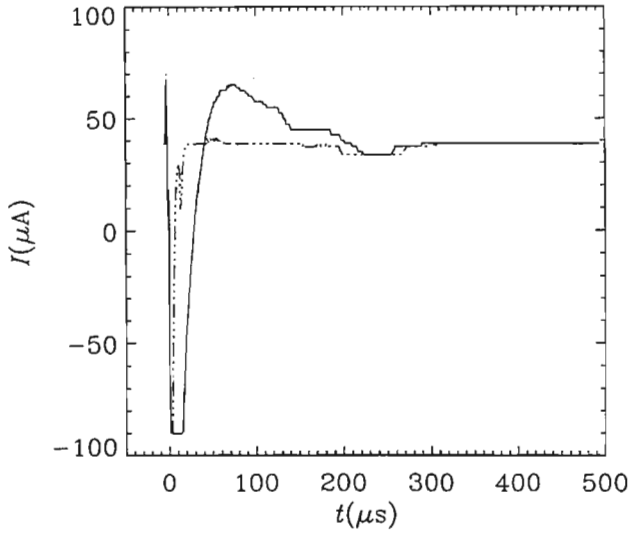

Figure 88: Ion saturation currents recorded in front of the apex, at (1.3, 1.1)cm (dashed) and concave region, at (2.6, 1.1)cm (solid) of the complex target.

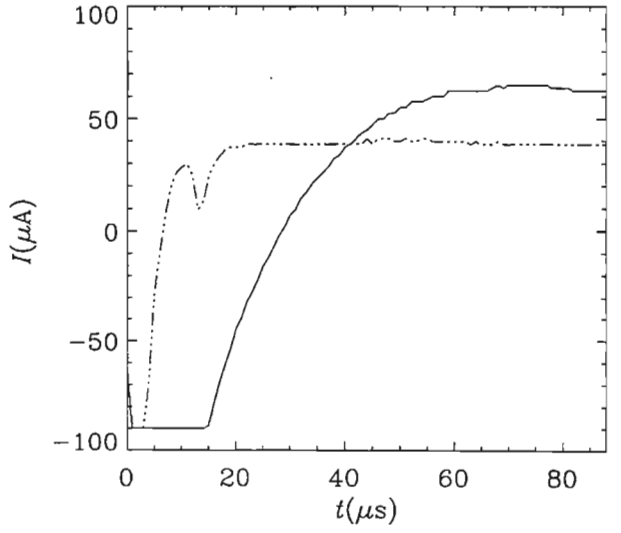

Figure 89: Ion saturation currents recorded in front of the apex, at (1.3, 1.1)cm, (dashed) and concave region, at (2.6, 1.1)cm, (solid) of the complex target, the first $80\mu s$.

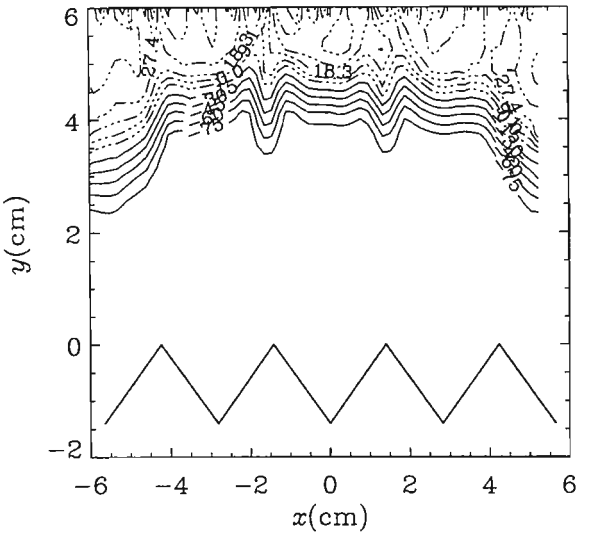

Figure 90: Two dimensional contour plot of ion saturation currents measured at $t = 2\mu$s. Solid contours show negative net current caused by electron swamping.

magnitude of this negative current is comparable to that measured by the electron saturation currents, i.e. ~ -5mA.

A feature to note in this figure is the especially interesting current recorded in front of the concave region at (-2.6, 1.1), where a very large negative current is detected, and which takes a long time ($\sim 45\mu$s) to recover. But having achieved a positive value, it then shows a higher current compared with that recorded near the apex at the same time. This time taken to recover is comparable to the long life-time of the electron currents shown in figure 86.

Full two-dimensional snapshots of the scanned region show these spatial variations quite clearly: Recorded 2μs after the high voltage pulse, figure 90 shows negative currents drawn with solid contours, and positive currents drawn with dashed contours. This choice was based on the desire to highlight areas of electron swamping,

Clearly visible in the large region between $y \sim 4.5$cm (which already shows some target-related structure) and the target, are regions of complete electron swamping.

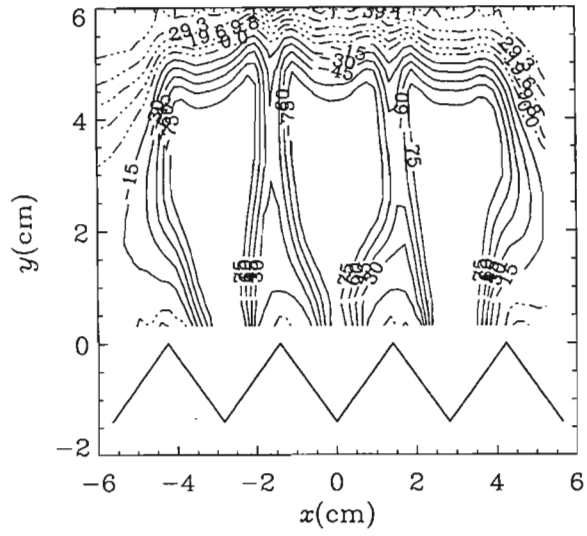

Figure 91: Contour plots of two dimensional ion saturation currents measured at $t = 5\mu$s. Positive current contours are now visible near the apexes. Solid contours show negative net current, contour labels are in μA.

Considering the same data 3μs later, at $t = 5\mu$s, in figure 91, it can be seen that the regions of electron swamping have been reduced to islands of similar shape to those regions of increased electron current shown in figure 84.

The expected positive ion currents are now visible in front of the apexes, albeit with low magnitude. This transition of the ion currents to net positive values can be seen extending into the previously negative regions further from the target.

Even considering a later time at $t = 50\mu$s, as shown in figure 92, negative currents are still being recorded close to the target in front of the concave regions.

However, high ion current islands form between 2 and 4cm away from the target, and are clearly visible after 70μs. Figure 93 shows the ion currents recorded at $t = 70\mu$s, with all contours drawn with dashed lines.

A general view of the plasma behaviour can be achieved by examining figures 94 and 95 which show the ion currents recorded at selected times over the first 200μs.

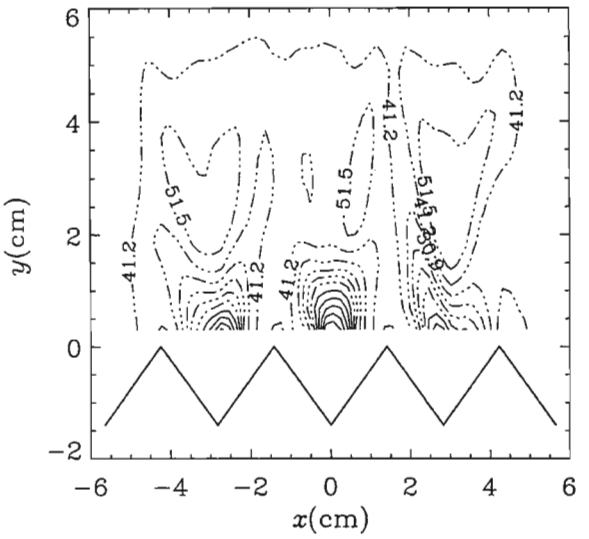

Figure 92: Contour plot of ion saturation currents measured at $t = 50\mu$s in two dimensions. Solid contours show negative net current, contour labels are in μA.

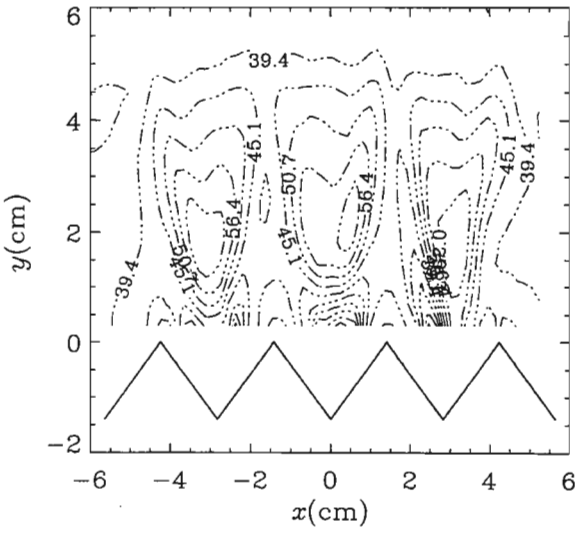

Figure 93: Contour plot ion saturation currents measured at $t = 70\mu$s. Contours show positive ion current, contour labels in μA.

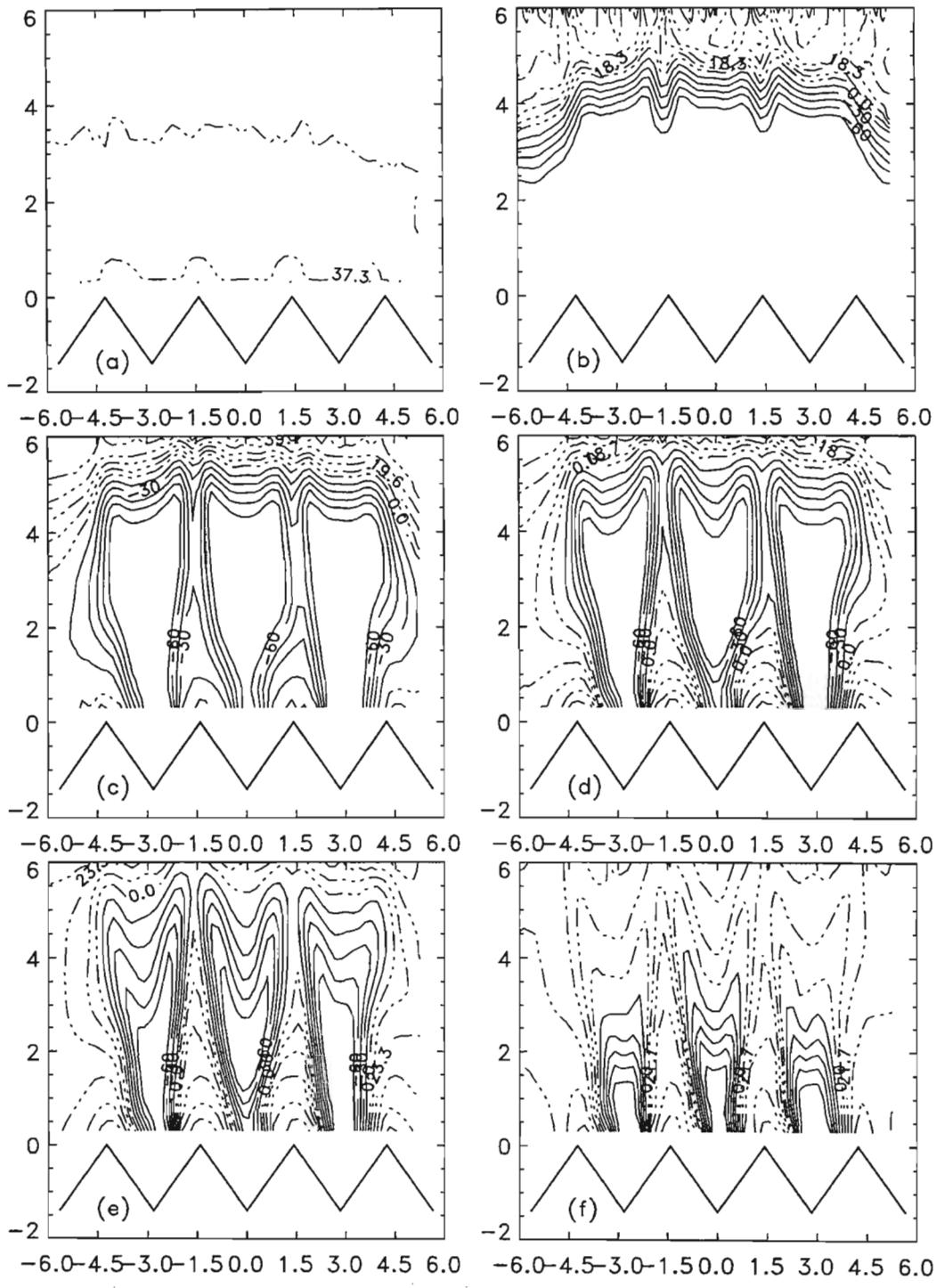

Figure 94: Two dimensional ion saturation current panels, measured at $t = -5, 2, 5, 7, 10$ and 20μs, contour values are in μA.

The formation and evolution of the electron-swamped regions, corresponding to the high-electron current regions, are clearly visible in figure 94, the ion current equivalent of figure 85. The horn shaped islands suggest the existence of adjacent regions of narrow beams of outward streaming electrons and inward bound ions, that is, focusing of outgoing electrons and channelling of incoming ions into narrow beams.

Looking at the long time ion behaviour in figure 95, which shows the ion currents recorded at $t = 50, 70, 90, 120, 150$ and 200μs, it can be seen how, at later times ($t > 70\mu$s), the ions show a strong tendency to be channelled into the regions in front of the concave regions. They are being accelerated toward the target, since for $t > 120\mu$s, the current measured increases with proximity to the target. The reduction in the vertical extent of these regions is probably related to the fact that at this time, the high voltage PSII pulse has dropped to less than half (25%) its maximum value. Examining the total current (figure 19) the total current to the target has also decreased to about 20% of its maximum value.

6.4.4 Summary

The important phenomena described in this analysis of spatially and temporally realised ion and electron saturation currents collected in the region around the complex target are:

1. The apparent focusing of electrons and channelling of ions into narrow localised regions clearly associated with specific features of the target structures.
2. From the electron saturation currents there is little evidence of sheath conformality.
3. Electron focusing resulting in a high localised electron flux incident on the chamber walls.
4. From the ion saturation currents, the sensitivity of the negatively biased probe to energetic ($kT > 70$eV) electrons makes it a useful tool for investigating localised variations in electron currents.

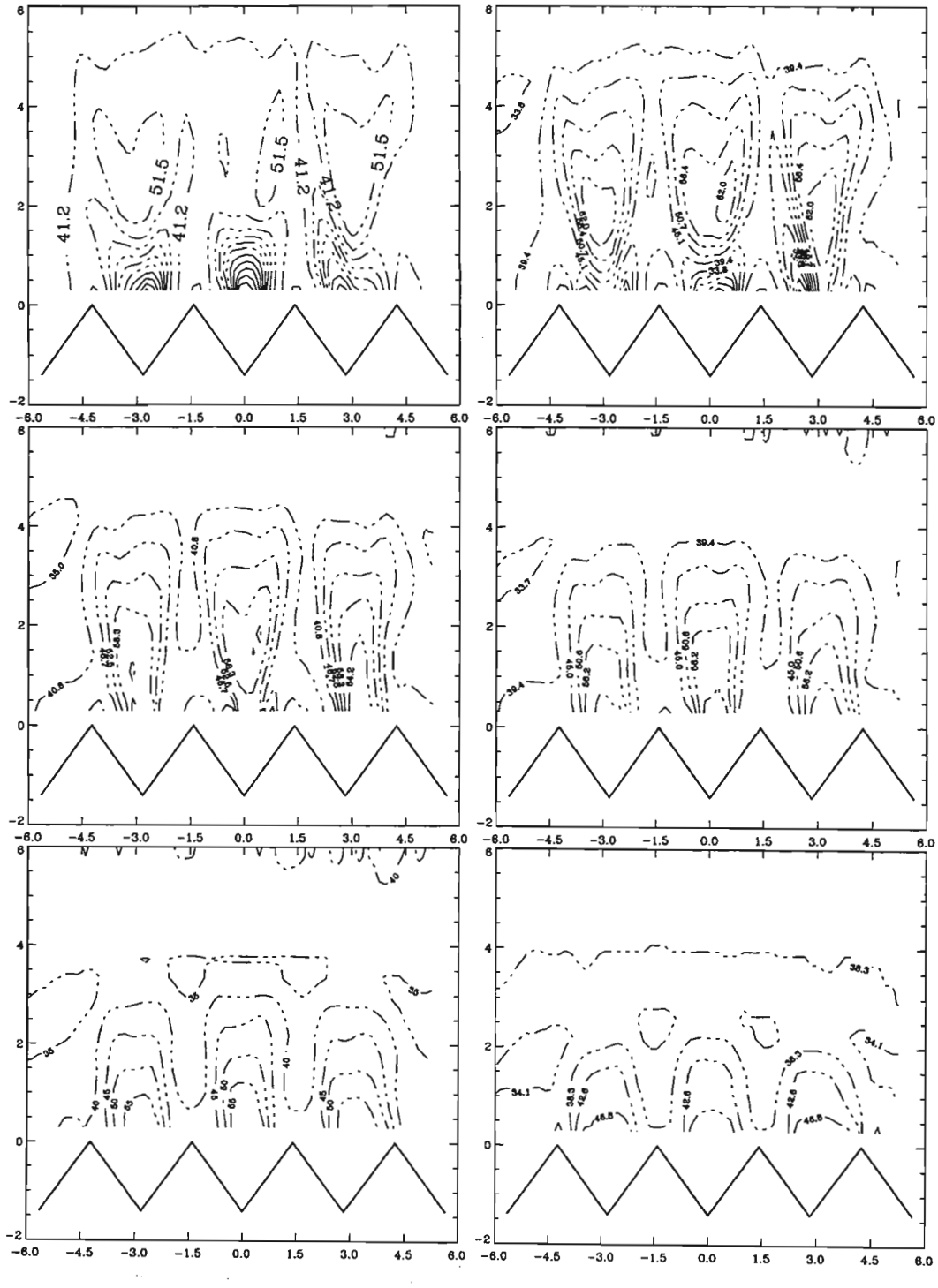

Figure 95: Two dimensional ion saturation current panels, measured at $t = 50, 70, 90, 120, 150$ and 200μs. Axes are in cm, contour values are in μA.

Unfortunately there are still questions about ion doses and angles of incidence that are beyond the scope of this investigation. The early time panels show definite electron focusing but because these electrons completely swamp the ion signal, very little ion information can be recovered. Also, little can be inferred about incoming ion channelling other than that there appears to be a stream of ions possessing a perpendicular velocity restricted to regions in front of the convex target features initially, and the concave features later. The regions in front of the target faces are dominated by energetic outbound electrons. As for the origin of these electrons, it is possible that they are secondary electrons ejected by the impact of ions, and to a lesser extent by ionising collisions between neutral gas atoms and electrons. The ionisation distance, or the mean free path (equation 1), is greater than 3000cm for 6keV electrons. They certainly cannot be electrons from the original plasma, as these are repelled away from the target over the entire initial ion matrix sheath during the first few electron plasma periods ($\tau_{pe} \simeq 0.01\mu s$).

It may be useful to use single sided probes and repeat the ion and electron current measurements. With single sided probes, it might be possible to detect spatial variations in the target-bound ion flux by using a probe which has the conducting surface facing away from the target biased to collect ions. These variations are presently being swamped by the energetic electrons which are ejected from the target and collected by the target-facing probe surface.

Finally, since the plasma is greatly disturbed by the application of the high voltage pulse to the target, the plasma potential decreases from the normal background value at the sheath edge ($x = s$), to the target potential at the target ($x = 0$). This has implications for a probe that is initially biased to -70V to collect an ion saturation current. The decrease in the local plasma potential as the sheath propagates past the probe would leave the probe biased *positive* with respect to the local plasma potential. Ions reaching the probe position x_p from the sheath edge would have gained enough energy to be able to overcome this positive probe bias and be collected.

Even though the original plasma electrons have been expelled from the region within the sheath, secondary electrons emitted from the target continue to traverse this region. Since the effective probe potential at x_p is positive, these electrons will be collected. This electron current can swamp the ion current if the secondary electron velocity and density is sufficiently high. While further from the target, even though the electrons have been accelerated to high velocities by the plasma potential, they are no longer well focused into a small region and tend to diverge. The resultant decreased flux would cause a reduced electron current contribution and explain the localised nature of the islands of electron swamping. Thus it appears that the ion currents can be used to detect the regions where electrons are focused with more sensitivity than the electron currents.

The increased ion currents measured at later times ($t > 60\mu s$) also suggest characteristic focussing effects of the target. By focusing incoming ions into a smaller region, the ion density there is increased, causing increased ion currents to be measured. While this effect may be occurring at earlier times, the electron swamping is preventing it from being seen, but at later times a reduced incident ion energy results in fewer secondary electrons being ejected, and hence a reduced electron density.

From examining panel (e) of figures 85 and 94, which shows the two dimensional electron and ion saturation currents measured at $t = 10\mu s$ respecively, it can be seen how the ion currents are swamped over a large portion of the measured area. By comparison, the electron currents do not show a corresponding increased current, except for three small islands of -0.5mA. It is not clear why increased electron saturation currents are not measured, although it is suspected that this may be related to the reduced oscilloscope sensitivity used to record them.

Chapter 7

Conclusion

7.1 Summary of Thesis Results

The experimental measurements have been performed to investigate the two dimensional plasma behaviour during the PSII process. Since an appropriate application for PSII is the implantation of machine parts, it was decided to select targets that had similar geometries: the square bar, for its resemblance to pierce punches, and the complex saw-tooth target, for its resemblance to gear teeth.

While the critical parameters of the PSII process, from a materials science point of view, are the implanted ion dose and depth, it is very difficult to examine these experimentally in order to be able to comment on how target geometry affects them. However, since the implanted ions are accelerated through the ion matrix sheath edge, an investigation of the plasma sheath gives information about the influence of target geometry on ion dose. Thus by referring to plasma behaviour it is specifically the plasma sheath behaviour that is being investigated.

Having said this, while it is possible to determine sheath position by measuring the plasma potential directly with an emissive probe, or with a capacitive probe [32], these are fairly difficult experimental tasks. It is thus instructive to consider to what extent simpler Langmuir probes, biased to collect ion and electron saturation currents

can be used to investigate sheath evolution.

Since, from the Poisson equation, it is the local density of the charged species that determines the space potential, it was first necessary to investigate the relationship between the saturation currents and plasma potential. In this regard, it was decided to use a particle-in-cell plasma simulation code to simulate the plasma behaviour under PSII conditions. By using this simulation code it was possible to extract the local plasma potential, particle density and velocity information directly. By integrating the velocity distribution function $f(x, v, t)$ for each particle species it was also possible to explicitly determine the simulation saturation currents and compare them with the equivalent experimentally measured values. In this way the correlation between sheath position and a transition in the electron saturation current was demonstrated. Once sheath position was positively associated with the decrease in electron saturation current, it was possible to use experimentally measured saturation currents to investigate sheath behaviour about square corners and in front of the complex-shaped saw-tooth target.

Investigations into sheath behaviour around the two dimensional targets revealed definite target non-conformality. With the rectangular target, this was manifested as a rounded sheath which formed further away from the target in the radial direction than in the axial direction. The sheath velocity was also higher in the radial direction. With the complex saw-toothed target, the sheath front was seen to have a spherical shape, showing no target conformality when it was 4cm away. This non-conformality affects the angle at which incident ions reach the target surface, possibly reducing the retained dose and causing damage due to sputtering, and possibly also causing an increased secondary electron flux from these regions.

Ion saturation currents were also measured. Experiments with the spherical target revealed a delay between the decrease in I_{sat}^{-} and I_{sat}^{+}, which is consistent with what we would expect for a sheath occurring in a region of oppositely charged charge sheets.

However, with the rectangular and complex targets, the ion currents were susceptible to electron swamping. These electrons are thought to be secondary electrons ejected from the target by ion bombardment which are then accelerated by the target potential to high energies. The extremely negative plasma potential which exists between the target and near the sheath edge results in a probe which is biased $\sim$ 90V negative with respect to the chamber to become biased positive with respect to the local plasma potential. Energetic ions from the sheath edge can still be collected by this probe, but the net ion current becomes sensitive to electron swamping.

Further examination of the ion currents revealed that electron swamping only occurred in certain localised regions. These regions were clearly associated with concave structures in the target, and thought to be caused either by the focusing of the secondary electrons, together with a localised increased secondary electron flux caused by the channelling of ions onto small regions of the target.

Further investigation of this electron swamping effect may make it possible to use it as a sensitive diagnostic tool for determining regions of enhanced electron flux, and hence non-uniform ion yield. Since the equivalent electron saturation current traces revealed only slightly increased electron currents, the electron saturation current appears to be an insensitive measurement in comparison. Analysis using electron swamping of the ion currents could be useful in determining which regions of the target are experiencing increased ion doses, without actually analysing the implanted ion concentration in the target.

The localised variations in the plasma potential causing the apparently negatively biased probe to become positively biased, with respect to the plasma, can make the ion currents a tool for detecting localised effects of target geometry on the electric field.

At later times increased ion currents were measured in front of the complex target. This could also be related to a decreased target potential resulting in reduced incident ion energies. Since γ, the secondary electron yield per ion, decreases with ion energy

at these energies, fewer secondary electrons would be ejected. A reduced electron density would increase the net ion current measured.

The results presented here suggest that the convex apexes will experience lower ion doses than the nadirs, and that the ions will not be normally incident on the angled faces. The focusing effects of concave structures on electrons in the complex target and the corners of the rectangular target was demonstrated.

7.2 Possibilities for further research

This investigation is by no means complete. Further information about the responses of plasmas to target geometry under PSII conditions must still be determined, specifically:

1. Detailed dose analysis near corners could be performed to check the phenomena reported by Sheridan and Alport [53].
2. The statements made about ion and electron channelling into beams in front of the complex shaped target could be investigated in more detail. This could be done by using single-sided probes. If the probe surface facing the target were covered with an electrically insulating material, the probe could be used to investigate variations in incident ion fluxes. By rotating the probe surface away from the target, variations in electron flux could also seperately be investigated. If the present understanding of the plasma evolution is correct, the ion currents should not show any electron swamping, but still be sensitive to spatial variations in ion flux.
3. Analysis of sputter damage and retained dose along the flat faces of the complex target could reveal information about ion trajectories.

Appendix A

PDS1 input file

The PIC simulation used input decks to determine the parameters of the plasma being simulated. Below is a sample input file describing the conditions of a typical spherical simulation.

```
Plasma Immersion Ion Implantation (IN MKS UNITS)r0=.02,r1=.15
Without electron and ion-neutral collisions (Argon atom)

-start_t[s]-finish_t[s]-t_step--rprobe[m]-v_max[V]-v_min[V]--ion_phi[V]-e_phi[V]
   0.0e-8     1.0e-6      1      0.05      10       -30       -36.0      36.0

-nsp---nc---nc2p---dt[s]---r0[m]---r1[m]---epsilonr--
  2   200   12e7    1e-9    0.035    0.4      1.0

-rhoback[C/m^3]---backj[Amp/m^2]---dde---extR[Ohm]---extL[H]---extC[F]--q0[C]-
      0.0              0.0         0.0    1.0e2      0.0     1.8e-10  1.0e-10

-dcramped--source--dc[V|Amp]--ramp[(V|Amp)/s]---ac[V|Amp]---f0[Hz]--theta0[D]-
    1        v       -5.0e3          -5.0e9         0          0.0       0.0

--secondary----e_collisional----i_collisional----reflux---nfft--
      0             0                0             0       256

--seec(electrons)---seec(ions)---ion species----Gpressure[Torr]---GTemp[eV]---
        0.0            0.2           2             1e-4           .026
```

```
ELECTRON-NEUTRAL COLLISIONAL PARAMETERS-----

--selsmax[m^2]---elsengy0[eV]---elsengy1[eV]---elsengy2[eV]-
     1.2e-19          0.3             15.0            20.0

--sextmax[m^2]---extengy0[eV]---extengy1[eV]---extengy2[eV]---
     7.0e-21         11.55           30.0           100.0

--sionmax[m^2]---ionengy0[eV]---ionengy1[eV]---ionengy2[eV]---
    3.0e-20           15.76          30.0            100.0

ION-NEUTRAL COLLISIONAL PARAMETERS-----

---achrgx[m^2]--bchrgx[m^2/V^1/2]-------ascat[m^2]--bscat[m^2/V^1/2]---
     2.0e-19            5.5e-19              1.8e-19      4.0e-19

SPECIES 1

----q[C]-------m[Kg]---j0L[Amp/m^2]---j0R[Amp/m^2]----initn[m^-3]--
 -1.602e-19   9.11e-31      0.0              .4             1e13

--v0L[m/s]---v0R[m/s]---vtL[m/s]---vtR[m/s]---vcL[m/s]---vcR[m/s]--vtperp[m/s]--
     0.0          0.        5.93e5     5.93e5         0.           0.         0.

---nbin----Emin[eV]----Emax[ev]
     50          0           10


SPECIES 2

----q[C] ------m[Kg]---j0L[Amp/m^2]---j0R[Amp/m^2]----initn[m^-3]--
  1.602e-19   66.8e-27      0.0           1.477e-3           1e13

--v0L[m/s]---v0R[m/s]---vtL[m/s]---vtR[m/s]---vcL[m/s]---vcR[m/s]--vtperp[m/s]--
    0.           0.         2.19e3     2.19e3         0.           0.         0.

---nbin----Emin[eV]----Emax[ev]
    50          0           10
```

Bibliography

[1] J.R. Conrad, R.A. Dodd, and F.J. Worzala. Plasma source ion implantation: A new manufacturing process for surface modification of materials. In *Society of Manufacturing Engineers: 15th NSF Grantees conference on Production Research and Technology*, 1989.

[2] S.C. Brown. *Basic Data of Plasma Physics.* M.I.T. Press, Cambridge, Massachusetts, revised second edition, 1976.

[3] C.K. Birdsall and A.B. Langdon. *Plasma Physics via Computer Simulation.* McGraw-Hill, New York, 1985.

[4] D.R. Askeland. *The Science and Engineering of Materials.* Von Nostrand Reinhold, London, s.i. edition, 1988.

[5] K.N. Strafford, P.K. Datta, and J.S. Gray. *Surface Engineering Practice.* Ellis Horwood Ltd, England, 1991.

[6] J.R. Conrad, R.A. Dodd, F.J. Worzala, and X. Qiu. Plasma source ion implantation: A new, cost-effective, non-line-of-site technique for ion implantation of materials. *Journal of Applied Physics*, 36:927–936, 1988.

[7] S.T. Picraux. Ion implantation metallurgy. *Physics Today*, 38:38–44, 1984.

[8] G.K. Hubler and E. McCafferty. *Corrosion Science*, 20:103–, 1980.

[9] G. Dearnaly. *Journal of Metals*, 34:18–, 1982.

[10] G. Dearnaly. In R. Kossowsky and S.C. Singhal, editors, *Surface Engineering*, New York, 1984. Plenum.

[11] D.M. Follstaedt, F.G. Yost, L.E. Pope, S.T. Picraux, and J.A. Knapp. *Applied Physics Letters*, 43:358–, 1983.

[12] J.M. Williams, G.M. Beardsley, R.A. Buchanan, and R.K. Bacon. In G.K Hubler, O.W. Holland, C.R. Clayton, and C.W. White, editors, *Ion Implantation and Ion beam processing of materials*, pages 735–, New York, 1984. North Holland.

[13] R. Hutchings. *Wear*, 92:143–, 1983.

[14] V. Ashworth, R.P.M. Proctor, and W.A. Grant. *Thin Solid Films*, 73:109–, 1980.

[15] J.R. Conrad. Plasma source ion implantation: A new approach to ion beam modification of materials. *Materials Science and Engineering*, 116:197–203, 1989.

[16] J.R. Conrad, J.L. Radtke, R.A. Dodd, F.J. Worzala, and N.C. Tran. Plasma source ion-implantation technique for surface modification of materials. *Journal of Applied Physics*, 62:4591–4596, 1987.

[17] S. Fayeulle, D. Trehaux, P. Guiraldeno, J. Dubois, and G. Fantozzi. *Journal of Material Science*, 21:1814–, 1986.

[18] F.G. Yost, S.T. Picraux, D.M. Follstaedt, L.E. Pope, and J.A. Knapp. *Thin Solid Films*, 107:287–, 1983.

[19] F.M. Kustas, M.S. Misra, and P. Sioshani. In G.K Hubler, O.W. Holland, C.R. Clayton, and C.W. White, editors, *Ion Implantation and Ion beam processing of materials*, pages 685–, New York, 1984. North Holland.

[20] M. Hirano and S. Miyake. *Applied Physics Letters*, 49:779–, 1986.

[21] N.E.W. Hartley. In S.T. Picraux and W.J. Choyke, editors, *Metastable Materials Formation*, pages 355–, New York, 1982. Elsevier.

[22] J.K. Hirvonen. In G.K Hubler, O.W. Holland, C.R. Clayton, and C.W. White, editors, *Ion Implantation and Ion beam processing of materials*, pages 621–, New York, 1984. North Holland.

[23] A.H. Dutchman and R.J. Partyka. In R. Kossowsky and S. Singhal, editors, *Surface engineering, surface modification of materials*, pages 185–, Boston, 1984. Martinus Mijhoff.

[24] L. Zhang, J.H. Booske, and J.L. Shohet. Anticorrosive surface modification of 6061-aluminum using plasma source ion-implantation. *Materials Letters*, 22(1):29–33, 1995.

[25] J. Min, P.K. Chu, Y.C. Cheng, J.B. Liu, S. Im, S. Iyer, and N.W. Cheung. Buried oxide formation by plasma immersion ion-implantation. *Materials Chemistry and Physics*, 40(3):219–222, 1995.

[26] K.C. Walter, R.A. Dodd, and J.R. Conrad. Corrosion behavior of nitrogen-implanted aluminum. *Nuclear Instruments and Methods in Physics Research Section B-Beam Interactions with Materials and Atoms*, 106(1):552–526, 1995.

[27] I.G. Brown, A. Anders, S. Anders, R.A. Castro, M.R. Dickinson, R.A. Macgill, and Z. Wang. Synthesis of unattainable ion-implantation profiles - pseudo-implantation. *Nuclear Instruments and Methods in Physics Research Section B-Beam Interactions with Materials and Atoms*, 106(1):646–650, 1995.

[28] J.N. Matossian. Plasma ion implantation technology at hughes research laboratories. *Journal of Vacuum Science and Technology B*, 12(2):850–853, 1994.

[29] W.A. Reass. Survey of high-voltage pulse technology suitable for large scale plasma source ion implantation processes. *Journal of Vacuum Science and Technology B*, 12(2):854–860, 1994.

[30] J.R. Conrad, S. Baumann, R. Fleming, and G.P. Meeker. Plasma source ion implantation dose uniformity of a 2x2 array of spherical targets. *Journal of Applied Physics*, 65(4), 1989.

[31] J.R. Smith, N. Hershkowitz, and P. Coakley. Inflection-point method of interpreting emissive probe characteristics. *Review of Scientific Instruments*, 50:210–218, 1979.

[32] G.A. Collins and J. Tendys. Sheath development around a high-voltage cathode. *Plasma Sources Sci. Technol*, 3:10–18, 1994.

[33] Francis F. Chen. *Introduction to Plasma Physics and Controlled Fusion.* Plenum Press, New York, second edition, 1984.

[34] I. Langmuir. *Physics Review*, 21:4–, 1923.

[35] D.R. Lide, editor. *CRC Handbook of Chemistry and Physics.* CRC Press, Boston, 72nd edition, 1991.

[36] I.M. Podgornyi. *Topics in Plasma Diagnostics.* Plenum Press, New York, 1971.

[37] N. Hershkowitz, J.R. DeKock, P. Coakley, and S.L. Cartier. Surface trapping of primary electrons by multidipole magnetic fields. *Review of Scientific Instruments*, 51:210–218, 1980.

[38] J.J. Carroll, M.E. Koepke, W.E. Amatucci, T.E. Sheridan, and M.J. Alport. A segmented disk electrode to produce and control parallel and transverse particle drifts in a cylindrical plasma. *Review of Scientific Instruments*, 65:2991–, 1994.

[39] W.H. Press, B.P. Flannery, S.A. Teukolsky, and W.T. Vetterling. *Numerical Recipes: The Art of Scientific Computing.* Cambridge University Press, Cambridge, 1986.

[40] I.J. Donnelly and P.A. Watterson. Ion-matrix sheath structure around cathodes of complex shape. *Journal of Physics D: Applied Physics*, 22:90–, 1989.

[41] P.A. Watterson. Child-langmuir sheath structure around wedge-shaped cathodes. *Journal of Physics D: Applied Physics*, 22:1300–, 1989.

[42] M.A. Lieberman. Model of plasma immersion ion implantation. *Journal of Applied Physics*, 66(7):2929–2929, 1989.

[43] J.T. Scheuer, M. Shamim, and J.R. Conrad. Model of plasma source ion implantation in planar, cylindrical and spherical geometries. *Journal of Applied Physics*, 63(3):1241–1245, 1990.

[44] Zhongyi Xia and Chung Chan. Modelling and experiment on plasma source ion implantation. *Journal of Applied Physics*, 73(8):3651–3656, 1993.

[45] R.A. Stewart and M.A. Lieberman. Model of plasma immersion ion implantation for voltage pulses with finite rise and fall times. *Journal of Applied Physics*, 70(7):3481–3487, 1991.

[46] G.A. Emmert and M.A. Henry. Numerical simulation of plasma sheath expansion, with applications to plasma source ion implantation. *Journal of Applied Physics*, 71(1):113–117, 1992.

[47] V. Vahedi, M.A. Lieberman, M.A. Alves, J.P. Verboncoeur, and C.K. Birdsall. A one dimensional collisional model for plasma immersion ion implantation. *Journal of Applied Physics*, 69:2008–, 1991.

[48] B.P. Wood. Displacement current and multiple-pulse effects in plasma source ion implantation. *Journal of Applied Physics*, 73(10):4770–4778, 1993.

[49] Dezhen Wang, Tengcai Ma, and Xinlu Deng. Model of collisional sheath evolution in plasma source ion implantation. *Journal of Applied Physics*, 74(4):2986–2988, 1993.

[50] K.-U. Riemann, U. Ehlemann, and K. Wiesemann. *Journal of Physics D: Applied Physics*, 25:620–, 1992.

[51] K. Thomas and M.J. Alport. Two ion fluid model for plasma source ion implantation. *Journal of Vacuum Science and Technology B*, 12(2):901–904, 1994.

[52] Wee Beng Lim, J. Cooney, M.S. Ghaemi, M. Gavin, D.R. Anderson, and K.E. Lonngren. On plasma sheaths surrounding complex shapes as measured using ion acoustic waves. *Journal of Physics D: Applied Physics*, 24:1081–1085, 1991.

[53] T.E. Sheridan and M.J. Alport. Ion-matrix sheath around a square bar. *Journal of Vacuum Science and Technology B*, 12(2):897–900, 1994.

[54] T.E. Sheridan and M.J. Alport. Two-dimensional model of ion dynamics during plasma source ion implantation. *Applied Physics Letters*, 64(14), 1994.

[55] M. Shamim, M.Malik, R.P. Fetherston, K. Sridharan, and J.R. Conrad. Sheath dynamics and dose analysis for planar targets in plasma source ion implantation. *Plasma Sources Science Technology*, 2:81–85, 1993.

[56] R. Faehl, B. De Volder, and B. Wood. Application of particle-in-cell simulation to plasma source ion implantation. *Journal of Vacuum Science and Technology B*, 12(2):884–888, 1994.

[57] MunPyo Hong and G.A. Emmert. Two-dimensional fluid modeling of time-dependant plasma sheath. *Journal of Vacuum Science and Technology B*, 12(2):889–896, 1994.

[58] T.E. Sheridan. The ion-matrix sheath around a round hole. *Plasma Sources Science and Technology*, 4(4):527–533, 1995.

[59] S. Qin, Z.J. Jin, and C. Chan. Dynamic sheath model of collisionless multispecies plasma immersion ion-implantation. *Journal of Applied Physics*, 78(1):55–60, 1995.

[60] T.E. Sheridan and M.J. Goeckner. Collisional sheath dynamics. *Journal of Applied Physics*, 77(10):4967–4972, 1995.

[61] T.E. Sheridan. Pulsed-sheath ion dynamics in a trench. *Journal of Physics D-Applied Physics*, 28(6):1094–1098, 1995.

[62] S. Mukherjee, K. Avinash, and P.I. John. Dynamic sheath expansion and ion current in transient ion sheath experiments. *Pramana-Journal of Physics*, 44(3):263–270, 1995.

[63] S. Mukherjee and P.I. John. Dynamics of a collisional ion sheath. *Pramana-Journal of Physics*, 44(1):55–66, 1995.

[64] M.P. Hong and G.A. Emmert. 2-dimensional fluid simulation of expanding plasma sheaths. *Journal of Applied Physics*, 78(12):6967–6973, 1995.

[65] M. Sun, P. Zhu, and S.Z. Yang. A model of plasma source ion-implantation for inner surface modification. *Journal of Physics D-Applied Physics*, 29(1):274–276, 1996.

[66] M.J. Goeckner, R.P. Fetherston, W.N.G. Hitchon, N.C. Horswill, E.R. Keiter, M.M. Shamim, R.A. Breun, J.R. Conrad, and T.E. Sheridan. Dynamics of collisional pulsed planar sheaths. *Physical Review E, Part B*, 51(4):3760–3763, 1995.

[67] F.A. Smidt and B.D. Sartwell. Manufacturing technology program to develop a production ion implantation facility for processing bearings and tools. *Nuclear Instruments and Methods B*, 6:70–77, 1985.

[68] M.M. Shamim, J.T. Scheuer, R.P. Fetherson, and J.R. Conrad. Measurement of electron emission due to energetic ion bombardment in plasma source ion implantation. *Journal of Applied Physics*, 70(9):4756–4759, 1991.

[69] K.N. Leung, T.K. Samec, and A. Lamm. Optimization of permanent magnet plasma confinement. *Physics Letters*, 51(8):490–492, 1975.

[70] R. Limpaecher and K.R. MacKenzie. Magnetic multiplole containment of large uniform collisionless quiescent plasmas. *Review of Scientific Instruments*, 44(6):726–731, 1973.

[71] M. Notcutt. Hv pulse supply for n^+ implantation: Development of power supply for ppri for plasma source ion implantation. Unpublished UND Physics internal report, dated 4 Oct 1991, 1991.

Appendix B

Paper in preparation

A paper relating to the work described in this thesis is currently in preparation, and has been included here for reference.

Appendix B

Paper in preparation

A paper relating to the work described in this thesis is currently in preparation, and has been included here for reference.

Measurements of two-dimensional PSII plasma sheaths

K.A.Meyer, M.S.Harmer, and M.J.Alport

Plasma Physics Research Institute,

Department of Physics,

University of Natal, Durban, South Africa 4001.

(July 15, 1996)

Abstract

In plasma source ion implantation (PSII), the target to be implanted is immersed in a plasma and pulsed to a high negative voltage. Plasma ions are accelerated from the ion matrix sheath edge, which forms around the target, and are implanted in its surface. Experimental results are presented using Langmuir probes biased to collect ion and electron saturation currents. The spatial and temporal behaviour of these currents are recorded around two dimensional targets, where evidence of electric field focusing of both the electron and ion saturation flux and the formation of flux islands is presented. Enhanced electron flux occurring predominantly in elongated regions corresponding to concave surface structures in the target is attributed to secondary electron emission.

I. INTRODUCTION

Plasma Source Ion Implantation (PSII) is a surface modification technique developed by Conrad and co-workers [1]. The implantation of ions into such diverse targets as drill bits, cutting dies, orthopaedic devices and automotive components has been shown to improve surface hardness and corrosion resistance [2–7].

In PSII, a negative high voltage (50kV) pulse is applied to a metal target that is immersed in a nitrogen plasma. The ions are initially collected from the ion matrix sheath that forms around the target within a few electron plasma periods (τ_{pe}). On a time scale of the ion plasma period (τ_{pi}), the sheath then propagates outward. Numerous papers have considered the one-dimensional formation [1] and evolution [8–15] of this sheath. One of the key questions is to what degree the sheath formation tends to follow a two dimensional target geometry and hence ensuring normal incidence of the ion trajectory on more realistic complex targets. Whilst it appears that sheath target conformality is not strict but is smoothed out with distance from the target, a perhaps more relevant problem is to understand and optimise the ion flux profile in the target itself, particularly at and close to corners since in many applications this is where the maximum wear will occur. Whilst the spatially resolved nitrogen implantation profiles can be measured using RBS or NRA, another technique involves measuring the plasma sheath structure, from which the trajectory of the ions can be inferred. It will be shown that for a more realistic complex target, secondary electron emission strongly perturbs this data.

Numerous numerical and theoretical studies of the one dimensional PSII model have taken place in order to gain an understanding of the basic dynamics of the PSII process. Numerical simulation of two dimensional targets in PSII has also been performed by many authors (Watterson (1989) [16], Donnelly and Watterson (1989) [17], Sheridan (1993) [18], Sheridan and Alport (1994) [19], and Hitchon and Keiter (1993) [20]). Watterson (1989) found that in the case of a convex cathode, the sheath is contracted near the point of the cathode with a maximum ion flux occurring at a distance $\approx W_p/10$ from the tip, where W_p

is the sheath width. However, zero flux was calculated right at the tip of the cathode in the case of a knife edge cathode (the cathode subtends an angle of less than 90^o). Donnelly and Watterson (1989) apart from getting similar results for the convex cathode, also considered the concave cathode and conversely found that there is a widening of the sheath and a decrease in the electric field - implying a lowering in the ion flux - near the bottom of the concave cathode. Sheridan (1993) considered square shaped cathodes arranged periodically. This author also observed focusing of ion flux near the tips of the cathode. However, the distance from the tip at which the focusing occurred was observed to be a function of time; at later times the focus moved further away from the cathode tip. Sheridan and Alport (1994) again considered the square shaped cathode, this time not in a periodic array. Focusing of ions near the cathode tip is again observed, and similarly to Watterson (1989) the maximum is observed at a distance of $\approx d_{im}/8$ from the edge, where d_{im} is the planar ion matrix sheath width. For a Debye length λ_D and ion matrix width corresponding to a plasma density of $10^9 \mathrm{cm}^{-3}$, $V_0 = 10\mathrm{kV}$, the dose is about 20% higher at a distance of 3mm from the corner of a target. This result needs to be confirmed experimentally since other modelling results (Hong and Emmert [21]) argued that this effect was due to a numerical artifact. The paper of Hitchon and Keiter (1993) investigates a cylindrical target. Their results indicate that a large number of the incident ions will have trajectories that are far from perpendicular to the surface of the target. Although they do not directly consider the ion dose at the target, they produce a velocity distribution of the ions at various distances from the centre of the circular face of the cylinder. These distributions would indicate a maximum ion flux near the centre of the face and not near the tip.

Results presented in this paper demonstrate sheath evolution around a right angled corner, where the sheath very quickly becomes spherical, and a saw-tooth shaped target, where evidence of electric field focusing of both the electron and ion flux as well as the formation of flux islands can be seen. An enhanced electron flux, which is attributed to secondary electron emission, is seen to swamp the ion flux. This occurs predominantly in elongated regions in front of concave surface structures in the target.

II. EXPERIMENTAL ARRANGEMENT

This experiment was performed in an aluminium-alloy cylinder 0.68m long and 0.45m in diameter. The end flanges house electrical lead-throughs for the Langmuir probes, the filament and discharge power supplies, and the observation windows. The device is evacuated to a base pressure of $< 10^{-6}$Torr and has an argon operating pressure of $\approx 10^{-4}$Torr. The inside walls of the chamber are lined with a water-cooled copper jacket which protects a large number of ceramic magnets arranged in the usual multidipole magnetic cusp configuration [22] to improve the confinement of primary plasma electrons.

The discharge is produced by a constant potential of 60V that is applied between the chamber walls and three rings of ohmically heated tungsten filaments. An electronic feedback circuit maintained the discharge current at a constant pre-set value of typically 500 mA by controlling the filament current to within 0.1%. This was found to be necessary in order to minimise variations in the discharge current and hence plasma density during the detailed two-dimensional probe scans that will be described below. Typical plasma parameters were $n_e \approx 10^9 \text{cm}^{-3}$, $T_e \approx 1\text{eV}$ and $T_i \approx 0.1\text{eV}$.

For typical industrial PSII applications a 50kV pulsed power supply is required to accelerate ions to sufficient energies so that they are ballistically implanted to a depth ≈ 1000Å in the metal target. Since in this experiment we are concerned with the plasma response and not the metallurgical processes, it was found that a voltage of 5–15kV was sufficient. Provided that a 50kV pulse had a similar rise time, the plasma sheath behaviour should not differ significantly.

The high voltage positive pulse was obtained by a step-up pulse transformer giving a fast linear pulse rise time $\approx 0.7\mu\text{s} \leq \omega_{pi}^{-1}$ and a longer RC decay time ≈ 0.5ms. The pulse repetition rate was 0.5 –5Hz. The output voltage was measured with a high-voltage probe while the total current drawn by the target was obtained either by measuring the voltage drop across a series resistor or from a Pearson current monitor. A typical voltage and current pulse is shown in figure 1. The current is characterised by a short (3μs) spike followed by a

slow decrease as the voltage decreases. The total current measured has two contributions. The first is due to ions being accelerated towards and subsequently collected by the negative target potential. In addition, there is a non-negligible negative current due to secondary electron emission. There have been a number of estimates for γ, the secondary electron emission coefficient (which is a sensitive function of surface composition and condition), ranging from a value of around 2.5 – 4 [9] to 4.8 – 6.2 [23] for steel. Besides making it difficult to use the total integrated current drawn by the target directly as a measure of implanted ion flux, the ejected electron current represents an additional wasteful drain on the pulse power supply.

Figure 2 shows a diagram of the target geometry used: a) a rectangular stainless steel bar having a length of 8cm and a square section with 2cm on a side and b) a brass right angled sawtooth or staircase with a straight side of length 2 cm. The staircase target had 4 steps, each 6.9 cm long, 2.8 cm wide and 1.4 cm tall, giving $L/\lambda_D \geq 40$ for L being a typical target dimension and λ_D the plasma debye length. These two geometries were chosen to represent prototypes of pierce punches and gear teeth - two typical industrial PSII applications. The target was connected to an oil cooled base by a high voltage feedthrough.

Sheath position, plasma parameters and local ion and electron saturation currents were measured by a Langmuir probe that could be moved axially in and out of the chamber, and radially across the chamber using computer controlled stepper motors. In this way, two-dimensional radial/axial scans were taken. The probe is a 3.5 mm diameter tantalum disk, its size optimised to maximise both the signal strength and the spatial resolution. For the purposes of sheath position measurements, the time and spatially resolved electron saturation current was measured by biasing the probe to +70V. The sheath edge was determined to be that position where the electron saturation current, I_{SAT}^{-}, decreased to a nominal fraction (typically 90%) of its unperturbed value. By measuring when the sheath edge passed each probe position as the probe was sequentially moved over the x-y plane, the two dimensional evolution of the sheath edge could be determined with a spatial resolution of 0.4mm. In addition, the spatially resolved ion saturation current traces were obtained by

biasing the probe to −70V. In this case, however, there were times after the pulse had been applied when the ion current was completely swamped by the electronic component when the secondary electrons ejected from the surface of the target (due to ion bombardment) had energies in excess of the probe bias potential i.e. 70V.

III. RESULTS FROM PARTICLE SIMULATION

Data obtained from the 1-D Birdsall particle-in-cell plasma simulation code, PDP1 was used to produce saturation current traces similar to those observed in the experiments from the produced time resolved density and velocity distributions. Figure 3 shows the calculated ion and electron saturation current densities (current per unit area) computed by evaluating a discrete version of the equations for the saturation current:

$$J_{SAT}(V) = \sum_i q_i \int_{-\infty}^{\infty} f_i(v)(v^2 - v_{min,i}^2)^{\frac{1}{2}} dv \qquad \text{for } v_{min,i}^2 \leq 0 \tag{1}$$

$$J_{SAT}(V) = \sum_i q_i \int_{v_{min,i}}^{\infty} f_i(v)(v^2 - v_{min,i}^2)^{\frac{1}{2}} dv + \sum_i q_i \int_{-\infty}^{-v_{min,i}} f_i(v)(v^2 - v_{min,i}^2)^{\frac{1}{2}} dv \quad \text{for } v_{min,i}^2 > 0. \tag{2}$$

where $v_{min,i}^2 = 2q_i(V - V_s)/m_i$, V the probe bias, V_s the plasma potential, q_i and m_i the charge and mass of the i^{th} particle species and f_i the distribution of the i^{th} species. The sums are calculated over all particle species.

The PDP1 code was run with a peak target potential of 5kV, a rise time of 1μs and a plasma density of 10^{13}m^{-3}. The gas used in the simulation was argon as in the experiment. To calculate the ion (J_{SAT}^{+}) and electron (J_{SAT}^{-}) saturation current densities a probe bias of −36V and +36V respectively was used, i.e. $J_{SAT}^{+} = J_{SAT}(V = -36V)$ and $J_{SAT}^{-} = J_{SAT}(V = +36V)$.

Although not shown in figure 3, high frequency oscillations ($f \approx f_{pe}$) were observed in J_{SAT}^{+}, and J_{SAT}^{-}, during the first 0.5μs after the pulse. Severe swamping of the ion saturation current is seen during the first 0.3μs. After about 4μs, there exists a period of non-zero J_{SAT}^{+}

and zero J_{SAT}^{-}, a necessary condition for the formation of the sheath. After 5μs, the sheath has swept through the simulation region and depleted the plasma.

In figure 4 we have compared the electron density with the plasma potential and J_{SAT}^{-}. The top plot shows contours of the electron density at 5% and 95% of the peak value and it is reasonable to assume that the world line of the sheath edge is to be found somewhere in between these two contours (in both the top and bottom plots the 'contours' on the right of the plot are due to noise present in the electron density and J_{SAT}^{-}). We see from the middle plot that the sheath edge does not compare well to contours of 50% or 10% of the plasma potential; however, the correspondence is fairly good at the point where the simulation plasma potential drops to within 1% of the target potential. The bottom plot shows the electron saturation current (J_{SAT}^{-}) at 5% and 95% of its peak value. These correspond remarkably well with the contours of the electron density and hence justify the measurement of the sheath position by inspection of J_{SAT}^{-}, although it must be noted that the very sharp, clean drop off in J_{SAT}^{-} observed in the simulation was not observed experimentally.

IV. EXPERIMENTAL RESULTS

Examples of the time resolved electron saturation current at three different probe positions are shown in figure 5. The nominated sheath positions are designated by the arrows.

Figure 6 shows the sheath evolution around the corner of the rectangular target. It does appear that in the axial direction, where the sheath is more spherical, it has a higher velocity than in the radial direction. We obtain a reasonable agreement with the theoretical equations derived by Scheuer et al [24] for a spherical target although the apparently larger radial velocity is contrary to the predictions of the planar geometry.

Contours of the two dimensional evolution of the normalised ion (left) and electron (right) saturation currents are plotted in figure 7 at 0, 5, 9 and 19μs after the voltage pulse has been applied to the staircase target.

The four left hand panels show the ion saturation current with the solid contours in

the range [0,1]. The dashed contours correspond to a negative net current due to the fact that the electron contribution completely swamps the ion current. The dashed contours are separated by 0.2 in the range [-1,0].

The contours for the electron flux panels in the four right hand panels were normalised in a similar method to the ion panels, thus the solid contours are in the range [0, 1] with a spacing of 0.1. Since the ion current never swamps the electron current, in these panels the dashed contours instead show additional detail at the low currents between 0.0 and 0.1, and have values of 0.050, 0.065 and 0.080. In general, the ion saturation current (left hand panels) show maxima near the target opposite the convex vertices. There are elongated valleys of net electron flux in front of the troughs of the target. For the electron saturation current, (right hand panels) the contours are essentially spherical in shape at $y \approx 5$cm but with elongated structures ($I_{SAT}^{-} \approx 0.02$) corresponding to concave structures of the target. We will now discuss these results in more detail.

At $t = 0\mu$s, the top two panels show the pre-pulse unperturbed density profile around the target where the background ion and electron currents are reduced to nearly half their global maximum as a result of the plasma sheath near the surface.

At $t = 5\mu$s, the net ion flux shows a severe disturbance. Generally, strong electron swamping occurs up to about 5cm away from the target with local minima in net current occurring about $y \approx 3$ cm from the target at $x \approx -2.8, 0$, and +2.8cm, ie opposite the troughs. As can be expected, the electron flux (right panel) reflects this structure, with the low-valued contours (0.2) dipping into the troughs of the target.

At $t = 9\mu$s the ion flux is still swamped by the channelling of electrons into the regions in front of the target troughs. This is visible in the electron saturation current panel as elongated islands at $y \approx 2$cm. However positive ion currents are visible as solid contours in front of the convex vertices.

In both panels the plasma has nearly stabilised at $t = 19\mu$s, and refilling of the depleted region is about to begin as the voltage decays. Note how the electron flux feature is significantly reduced. In the left hand panel this can be seen from the reduced regions of electron

swamping. Since electron swamping is still occurring, energetic electrons are being ejected from the target. The very elongated ion islands that are visible show the strong focusing effects of the target, which focus ions and electrons into the three regions in front of the concave target structures. Ion focusing can be inferred from the horn-shaped structure of these regions, since ions focused down the centre of the region result in an increased ion flux which is less susceptible to electron swamping. Thus positive currents, or reduced electron currents, indicate regions of increased ion flux. The sheath edge has moved off the electron current panel at $y \approx 6$cm.

It can thus be seen how the shape of the target focuses and channels secondary electrons emitted from the target into regions that show up as stable electron islands in the electron flux panels which form in front of concave regions of the target, which corresponding to regions of increased electric field intensity. This behaviour can be graphically illustrated by animating the sequence of data sets.

Figure 8 shows the long time relaxation of the plasma sheath together with the replenishing of the plasma density after $30, 40, 70$ and 100μs. The four panels on the right hand side show the sheath propagating inwards as the voltage decays from 5.25kV at 30μs to 3.25kV at 100μs. For $t = 30$ and 40μs, the ion saturation curves are similar to those shown in figure 7 with the electron component continuing to decrease in magnitude at 70 and 100μs. However, for $t > 40\mu$s, the net flux changes polarity and the region in front of the target troughs become ion islands. Thus once the electron component has been reduced to the point that it no longer affects the ion current, the target focuses ions into the regions in front of the concave target structures. The electron flux no longer swamps the ion current possibly due to a reduction in γ at these low target voltages. This behaviour is more explicitly shown in figure 9 by plotting the temporal behaviour of the electron and ion fluxes at representative spatial positions X, Y and Z shown by the crosses in the top panels. There is only strong swamping of the ion flux for the first few μs in panels (a), (c) and (e). However, in panel (e) corresponding to position 'Z' opposite the target trough, the swamping lasts for about 40μs, after which the net current changes polarity. For clarity the trace has been truncated

at $I = -1$ for $t < 40\mu$s. Panels (b), (d) and (f) show a depletion of the electron flux after 10μs, as the sheath passes the probe location. After 200–300μs, the plasma sheath recovers as the Child-Langmuir sheath collapses back into the target.

V. DISCUSSION

In this experiment, we have found that the net particle flux measured in front of a complex target pulsed to 6kV is dominated by the electron component even though the sheath has already propagated through the region. Initially, after the positive pulse has been applied, the electrons are repelled from the ion matrix region, $y \approx 3$cm. The plasma sheath then propagates outwards and we still continue to measure a strong electron flux component that is restricted to spatial regions in front of the concave structures (the troughs) of the staircase target. Calculation of the vacuum electric field structure suggests that this causes a focusing of the low energy ($\sim$ eV) secondary electrons emitted from the target surface. The decay of this component after $t \approx 70\mu$s as the target voltage decreases is due to the behaviour of γ which generally is a decreasing function of ion energy [25]. The plasma density and the sheath behaviour should not be affected by the secondaries as they are accelerated through the plasma sheath since their mean free path is $\sim$ 30m at 6keV [26], and $\sim$ 5m at 1keV. Data obtained from the one dimensional PIC simulation code PDP1 using typical values of γ has confirmed this result. It should be pointed out that the focusing of the secondary electrons will result in corresponding localised generation of X-rays at the vacuum vessel walls. This result should be taken into account in the optimal design of lead shielding to protect personnel in an industrial PSII facility which will increasingly operate with target voltages in excess of 100kV [27,28].

Experiments are under way using single sided probes to confirm that the measured electron flux is indeed emitted from the target surface. It would also be possible to measure the energy distribution of the ion and electrons by using variable bias voltages.

VI. CONCLUSIONS.

In conclusion, by using the PDP-1 PIC plasma simulation code, we have shown a relation between the plasma potential and the electron saturation current which may be used for the more convenient experimental identification of sheath position. We have also presented results demonstrating sheath non-conformality around square and saw-tooth target structures, and shown how concave target structures focus ingoing plasma ions and outgoing secondary emitted electrons. The presence of secondary electrons behind the PSII sheath has been shown to swamp the ion saturation currents.

REFERENCES

[1] J.R. Conrad, J.L. Radtke, R.A. Dodd, F.J. Worzala, and N.C. Tran. Plasma source ion-implantation technique for surface modification of materials. *J. Appl. Phys.*, 62:4591–4596, 1987.

[2] G.K. Hubler and E. McCafferty. *Corrosion Science*, 20:103–, 1980.

[3] G. Dearnaly. *J. Metals*, 34:18–, 1982.

[4] G. Dearnaly. In R. Kossowsky and S.C. Singhal, editors, *Surface Engineering*, New York, 1984. Plenum.

[5] D.M. Follstaedt, F.G. Yost, L.E. Pope, S.T. Picraux, and J.A. Knapp. *Appl. Phys. Lett.*, 43:358–, 1983.

[6] J.M. Williams, G.M. Beardsley, R.A. Buchanan, and R.K. Bacon. In G.K Hubler, O.W. Holland, C.R. Clayton, and C.W. White, editors, *Ion Implantation and Ion beam processing of materials*, pages 735–, New York, 1984. North Holland.

[7] R. Hutchings. *Wear*, 92:143–, 1983.

[8] T.E. Sheridan, M.J. Alport, W.E. Amatucci, J.J. Carroll III, and M.E. Koepke. Robust analysis of Langmuir probe data. Submitted Rev. Sci. Instrum., 1992.

[9] Zhongyi Xia and Chung Chan. Modelling and experiment on plasma source ion implantation. *J. Appl. Phys.*, 73(8):3651–3656, 1993.

[10] R.A. Stewart and M.A. Lieberman. Model of plasma immersion ion implantation for voltage pulses with finite rise and fall times. *J. Appl. Phys.*, 70(7):3481–3487, 1991.

[11] G.A. Emmert and M.A. Henry. Numerical simulation of plasma sheath expansion, with applications to plasma source ion implantation. *J. Appl. Phys.*, 71(1):113–117, 1992.

[12] V. Vahedi, M.A. Lieberman, M.A. Alves, J.P. Verboncoeur, and C.K. Birdsall. A one dimensional collisional model for plasma immersion ion implantation. *J. Appl. Phys.*,

69:2008–, 1991.

[13] B.P. Wood. Displacement current and multiple-pulse effects in plasma source ion implantation. *J. Appl. Phys.*, 73(10):4770–4778, 1993.

[14] Dezhen Wang, Tengcai Ma, and Xinlu Deng. Model of collisional sheath evolution in plasma source ion implantation. *J. Appl. Phys.*, 74(4):2986–2988, 1993.

[15] K. Thomas and M.J. Alport. Two ion fluid model for plasma source ion implantation. *J. Vac. Sci. Technol. B*, 12(2):901–904, 1994.

[16] P.A. Watterson. Child-Langmuir sheath structure around wedge-shaped cathodes. *J. Phys. D: Appl. Phys.*, 22:1300–, 1989.

[17] I.J. Donnelly and P.A. Watterson. Ion-matrix sheath structure around cathodes of complex shape. *J. Phys. D: Appl. Phys.*, 22:90–, 1989.

[18] T.E. Sheridan. Model of plasma source ion implantation into a trench. In preparation, dated 23 Jan 1993, 1993.

[19] T.E. Sheridan and M.J. Alport. Ion-matrix sheath around a square bar. *J. Vac. Sci. Technol. B*, 12(2):897–900, 1994.

[20] W.N.G. Hitchon and E.R. Keiter. Kinetic simulation of a time-dependant two-dimensional plasma. *J.Comput.Phys.*, 112:226–, 1993.

[21] MunPyo Hong and G.A. Emmert. Two-dimensional fluid modeling of time-dependant plasma sheath. *J. Vac. Sci. Technol. B*, 12(2):889–896, 1994.

[22] N. Hershkowitz, J.R. DeKock, P. Coakley, and S.L. Cartier. Surface trapping of primary electrons by multidipole magnetic fields. *Rev. Sci. Instrum.*, 51:210–218, 1980.

[23] M.M. Shamim, J.T. Scheuer, R.P. Fetherson, and J.R. Conrad. Measurement of electron emission due to energetic ion bombardment in plasma source ion implantation. *J. Appl. Phys.*, 70(9):4756–4759, 1991.

[24] J.T. Scheuer, M. Shamim, and J.R. Conrad. Model of plasma source ion implantation in planar, cylindrical and spherical geometries. *J. Appl. Phys.*, 63(3):1241–1245, 1990.

[25] S.C. Brown. *Basic Data of Plasma Physics.* M.I.T. Press, Cambridge, Massachusetts, revised second edition, 1976.

[26] Francis F. Chen. *Introduction to Plasma Physics and Controlled Fusion.* Plenum Press, New York, second edition, 1984.

[27] W.A. Reass. Survey of high-voltage pulse technol. suitable for large scale plasma source ion implantation processes. *J. Vac. Sci. Technol. B*, 12(2):854–860, 1994.

[28] J.N. Matossian. Plasma ion implantation technology at Hughes Research Laboratories. *J. Vac. Sci. Technol. B*, 12(2):850–853, 1994.

FIGURES

FIG. 1. A typical voltage waveform together with a plot of the total current drawn by the target.

FIG. 2. Schematic diagram of the target geometries used, showing a) the rectangular target and b) the right angled staircase target.

FIG. 3. Ion (J^+_{SAT} - top) and electron (J^-_{SAT} - bottom) saturation current traces obtained from PDP1. The x-axis is the time after the onset of the pulse, for the first 10μs. The pulse reached its peak at 1μs.

FIG. 4. Results obtained from the PDP1 plasma simulation code showing the electron density (top), contours at 5% (left) and 95% (right) of the peak value. Plasma potential (middle), contours at 50%, 10% and 1% (going from left to right) of the target potential. (bottom), contours at 5% (left) and 90% (right) of the peak value. The y axis measures time after the onset of the pulse up to the first 10μs. The x axis is position from the target, which is at the left hand vertical axis, with the far plasma boundary being at the right hand vertical axis.

FIG. 5. Evolution of the electron saturation current drawn by the Langmuir probe at three increasing distances from surface of the rectangular target.

FIG. 6. Contour plot of the sheath evolution around the rectangular target. The contour values are in μs.

FIG. 7. Two dimensional evolution of the electron saturation, I^-_{SAT}, (left) and ion saturation current, I^+_{SAT} at 0, 5, 9 and 19μs after the voltage pulse has been applied.

FIG. 8. Long time behaviour ($t = 30, 40, 70$ and 100μs) ion and electron saturation curves.

FIG. 9. The bottom six panels (a)–(f), are plots of the temporal evolution of the ion and electron saturation current curves at the three spatial positions X, Y and Z shown with crosses in the top two panels.

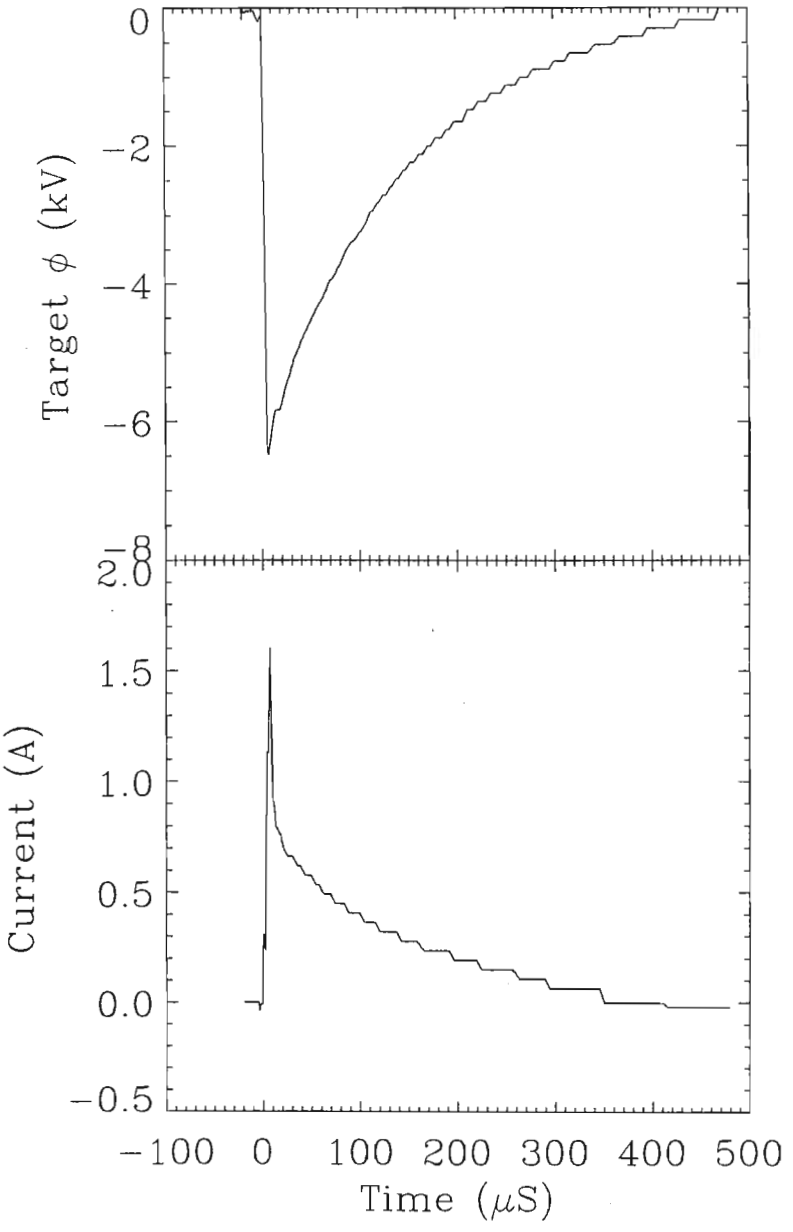

Figure 1: A typical voltage waveform together with a plot of the total current drawn by the target.

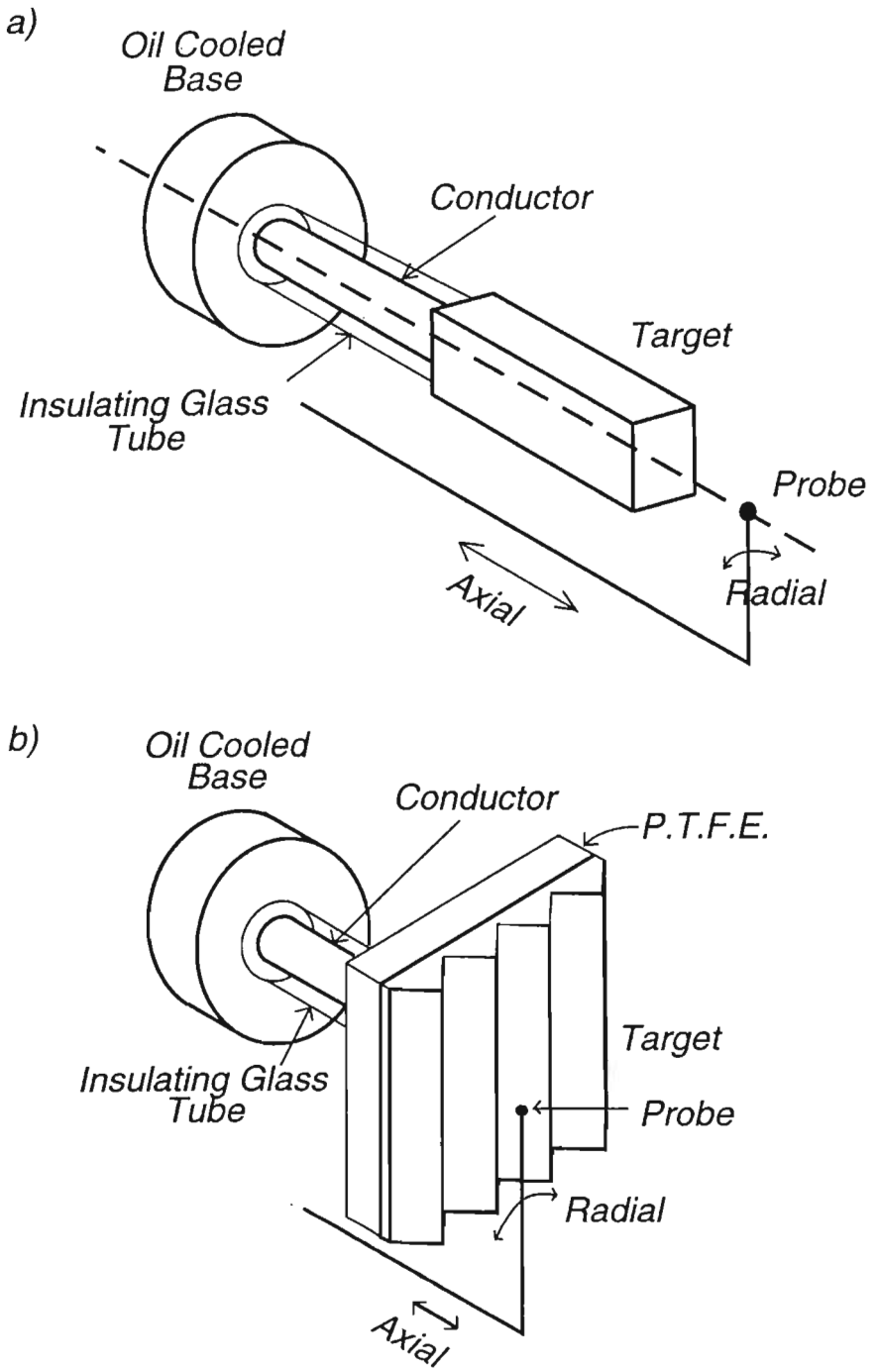

Figure 2: Schematic diagram of the target geometries used, showing a) the rectangular target and b) the right angled staircase target.

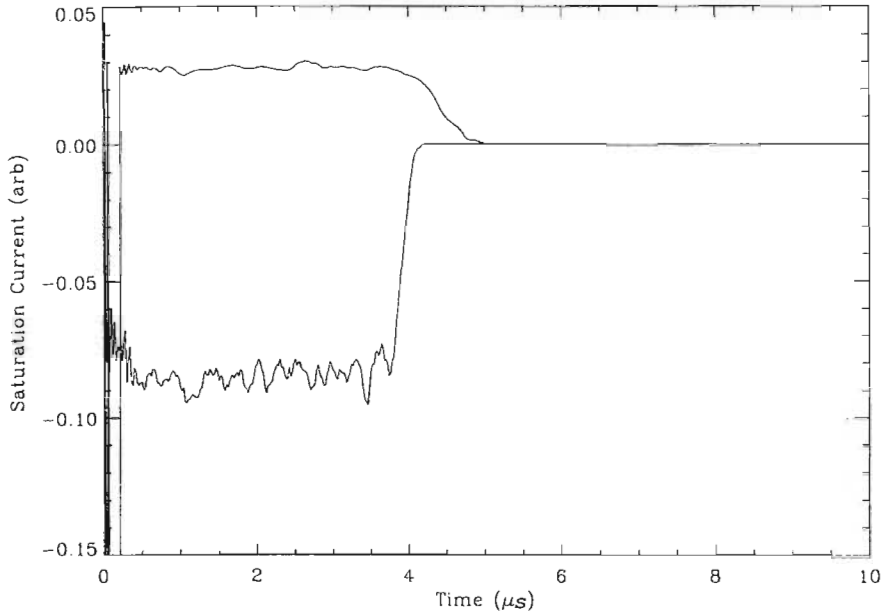

Figure 3: Ion (J^+_{SAT} - top) and electron (J^-_{SAT} - bottom) saturation current traces obtained from PDP1. The x-axis is the time after the onset of the pulse, for the first 10μs. The pulse reached its peak at 1μs.

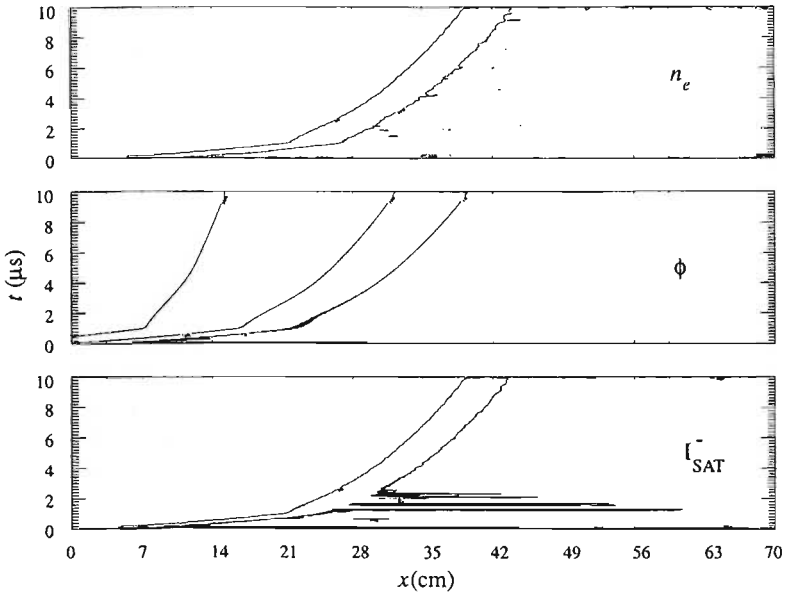

Figure 4: Results obtained from the PDP1 plasma simulation code showing the electron density (top), contours at 5% (left) and 95% (right) of the peak value. Plasma potential (middle), contours at 50%, 10% and 1% (going from left to right) of the target potential. (bottom), contours at 5% (left) and 90% (right) of the peak value. The y-axis measures time after the onset of the pulse up to the first 10μs. The x-axis is position from the target, which is at the left hand vertical axis, with the far plasma boundary being at the right hand vertical axis.

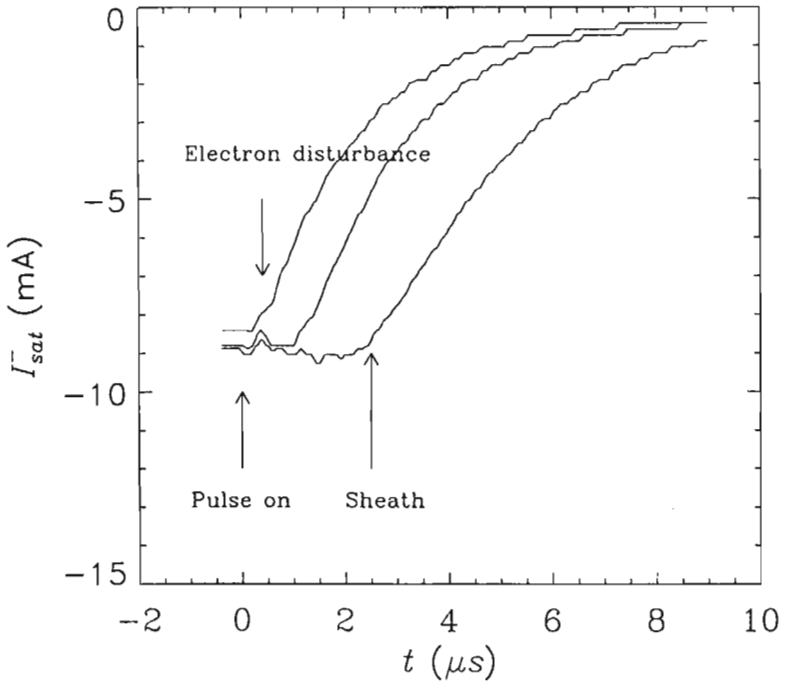

Figure 5: Evolution of the electron saturation current drawn by the Langmuir probe at three increasing distances from the surface of the target. Probe positions are (left to right) 1.6, 2.7 and 3.4 cm from the target.

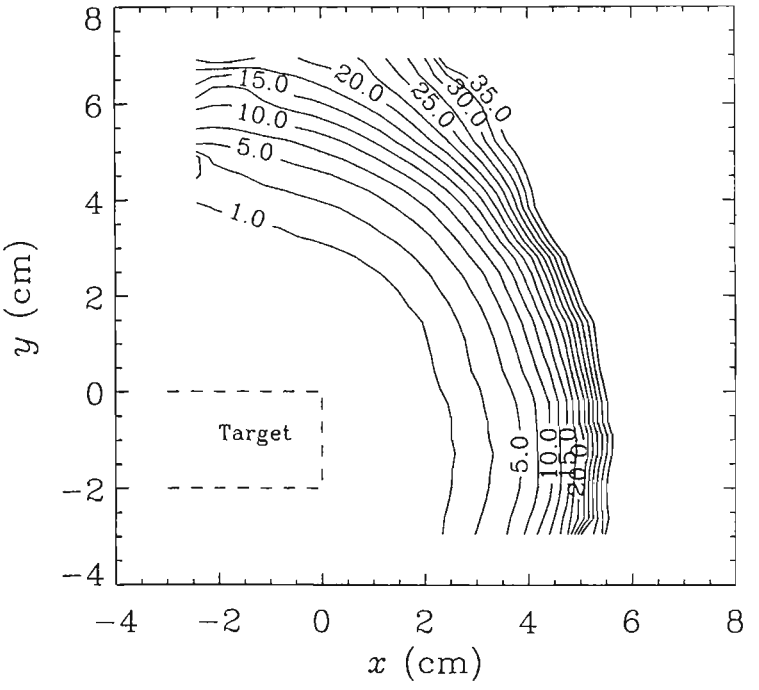

Figure 6: Contour plot of the sheath evolution around the rectangular target. The contour values are in μs.

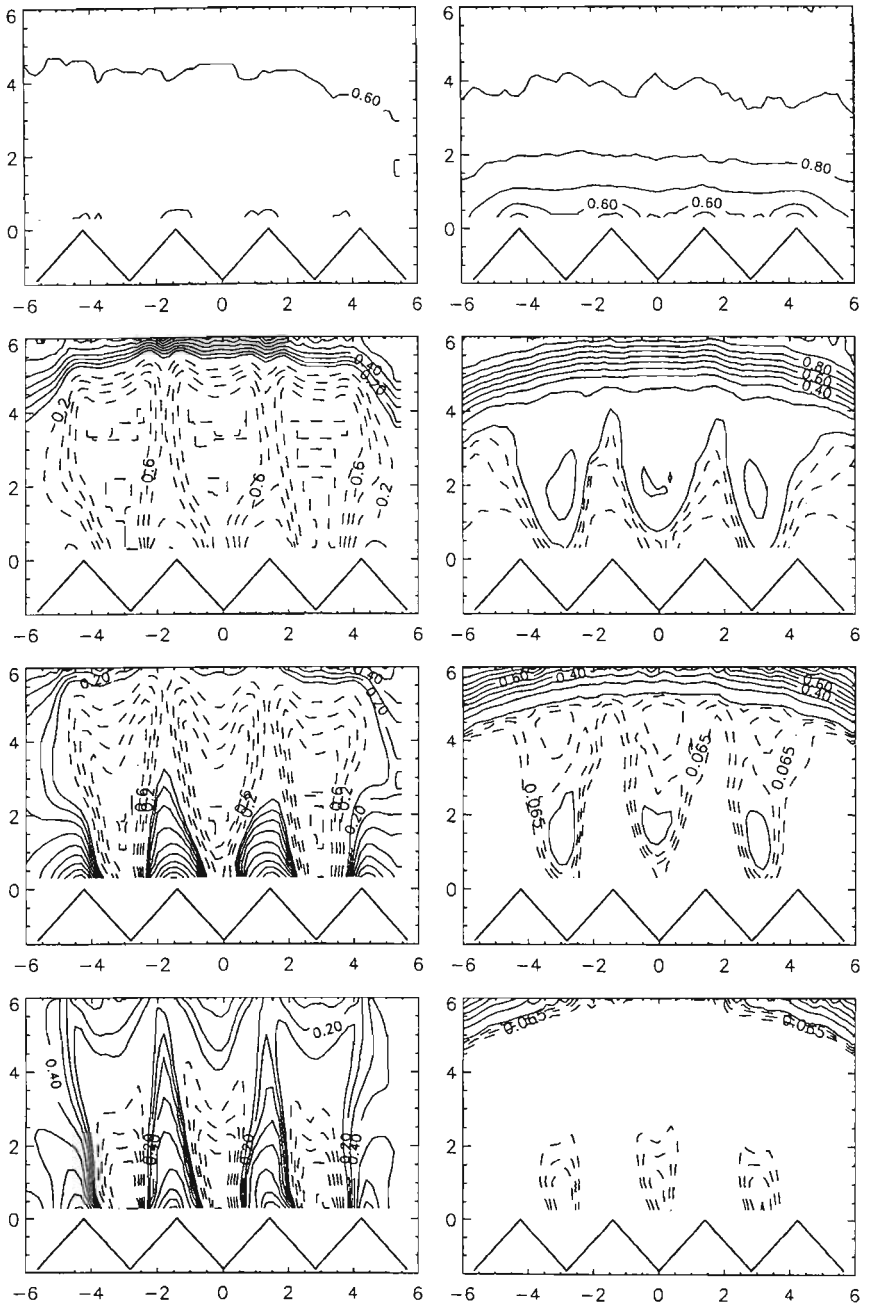

Figure 7: Two dimensional evolution of the electron saturation, I_{SAT}^{-}, (right), and ion saturation current, I_{SAT}^{+} (left) measured 0, 5, 9 and 19μs after the voltage pulse had been applied.

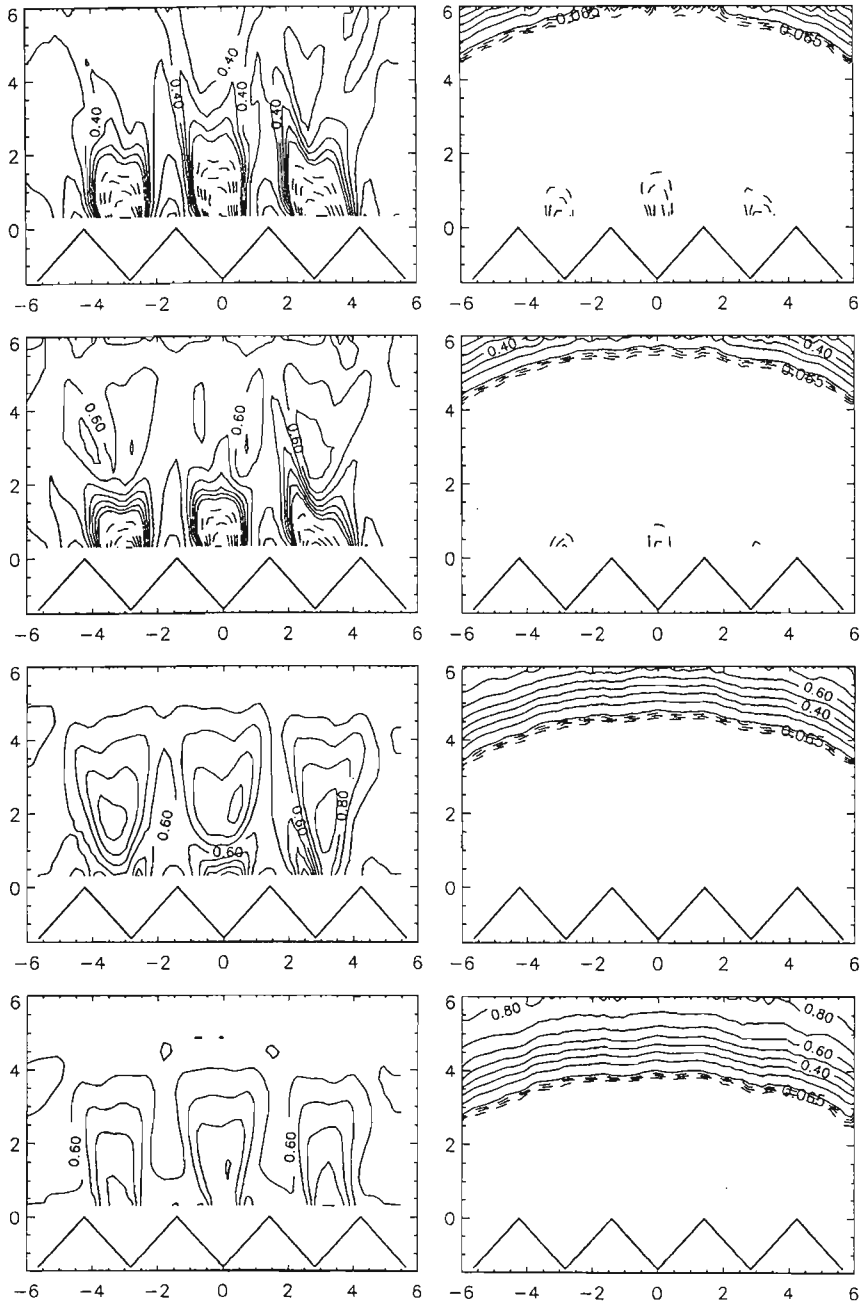

Figure 8: Long time behaviour ($t = 30, 40, 70$ and 100μs) ion and electron saturation curves.

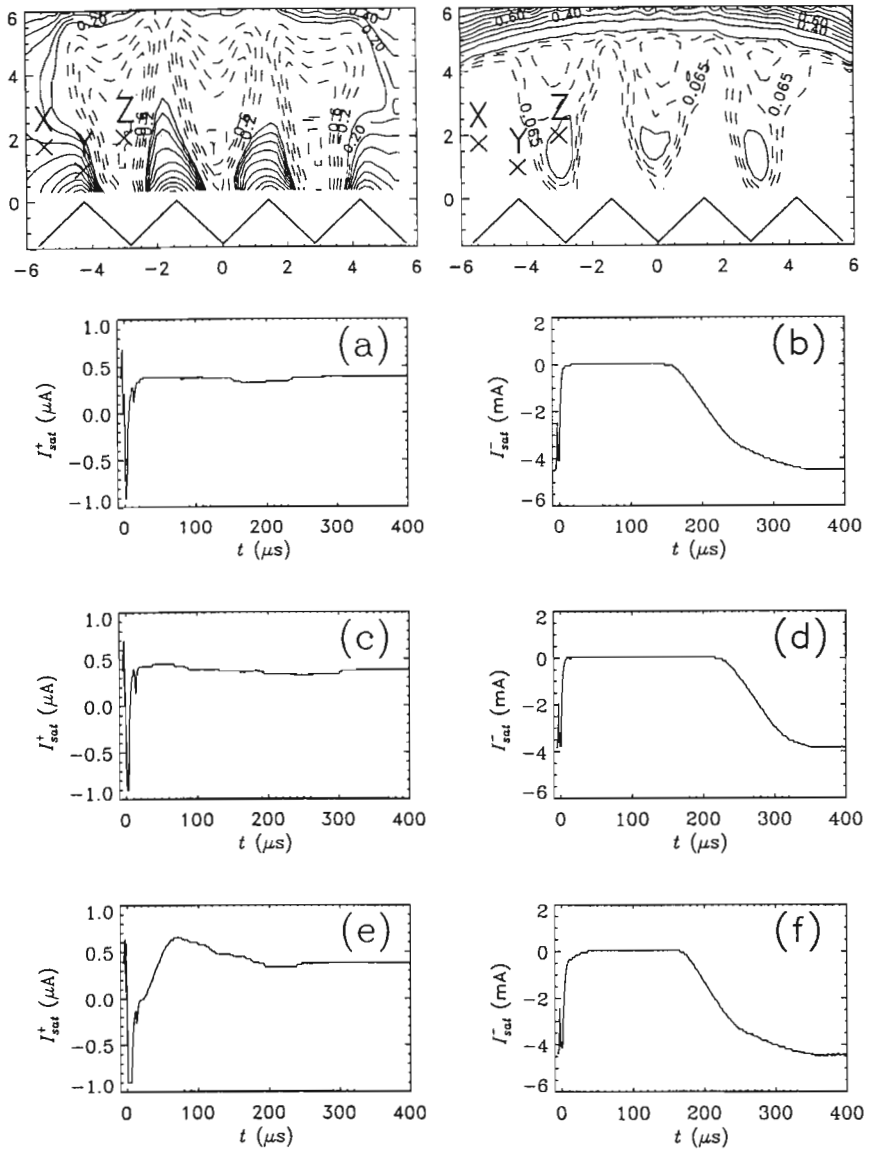

Figure 9: The bottom six panels (a)–(f), are plots of the temporal evolution of the ion and electron saturation current curves at the three spatial positions X, Y and Z shown with crosses in the top two panels.